Technische Universität München
Physics Department

The imprint of the dynamical state on the structure of magnetic fields in simulated galaxy clusters

Diploma thesis
by
Rüdiger Pakmor

written at the
Max Planck Institute for
Astrophysics

November 2006

Contents

1 Introduction

Galaxy clusters are the largest bound systems in the universe. It has been known for some tens of years that they contain magnetic fields. However their strength, distribution and structure were hard to measure. Only recently it became possible not only to measure the magnetic field strength more accurately, but also its structure. This was achieved by the detailed study of Faraday rotation maps of clusters, which allow to determine the power spectrum of the magnetic field. Knowing these powerspectra from observations, the next step is to compare them with the magnetic fields obtained from simulated galaxy clusters, to see if the present models of generation and evolution of the magnetic fields fit not only their overall strength, but also their observed structure.

The task of this work was to analyse the magnetic field of galaxy clusters simulated using the smoothed particle hydrodynamics (SPH) method and compare them with observations. As these simulations need to cover a wide dynamical range, the method has to be adaptive (like SPH). But for the calculation of the magnetic power spectrum or similar quantities it is necessary to have the quantities on a cartesian grid. Therefore the quantities directly derived from the simulation have to be interpolated or averaged onto a cartesian grid. However, the results of this procedure may depend on its internal details. For this reason I compared 6 different methods by their error for different sizes and resolutions of the grid, and chose the most suited to be used for the calculations.

Using the chosen method I calculated the magnetic field on a grid for 3 different simulated clusters and I analysed the dependence of their structure on their dynamical history. The data on the grid allow then to calculate the magnetic energy, power spectrum and autocorrelation function in these simulated clusters. This provides not only an opportunity to compare the structure of the magnetic field with observed ones, but also to understand its evolution within the simulation. By doing this calculation for a tightly sampled time sequence, it is possible to trace the evolution of the structure of the magnetic field.

The same grid calculation method also allows to derive other cluster properties like the kinetic and inner energy, or observable quantities like X-ray emission and temperature and to compare them with the properties of the magnetic field. These are connected with a chain of physical processes that take place during the formation and evolution of the cluster. So for example the infall of matter into the potential of the cluster increases the kinetic energy. It also creates shocks, that run through the cluster gas, increase its

inner energy and reduce the kinetic energy as they slow down. The magnetic field is affected indirectly, as it gets twisted and bend by the complex velocity field and can also be amplified by compression and shear flows. The grid also allows to calculate the total kinetic and magnetic energy on different scales. This can help to understand how the magnetic and velocity fields of the cluster are affected by the evolution of the cluster and especially by the accretion of other halos. Depending on the mass ratio between the cluster and the merging halo, these mergers are called minor or major mergers.

This thesis is divided into 6 parts. It starts with a basic explanation of the cosmological background in section 2. It is followed by a chapter about the formalism that was used for the simulation of the galaxy clusters (3). Section 4 discusses the different methods to calculate the grid and their differences. Section 5 introduces the magnetic power spectrum and autocorrelation function, also showing some tests of their properties. In section 6 the previously introduced methods were used to study 3 simulated clusters. Finally section 7 gives a short summary of the results of this work.

2 Basics of Cosmology

2.1 Light

For thousands of years the only way for people to learn about the universe was to look at the sky. Even with this - compared to now - poor information they managed to understand and predict many things. So they identified the planets of the solar system from Mercury to Saturn and they were able to predict their orbits. Also they had the knowledge to calculate solar eclipses, even though they assumed that the earth was the center of the universe with everything else orbiting around it. In the 17th century Galileo Galilei was the first one to use a telescope to improve his sight. With telescopes it was possible to look at smaller, fainter and therefore more distant objects. This also led to the success of the heliocentric theory over the old geocentric theory by the observations of some satellites of Jupiter. In the beginning of the 19th century astronomers introduced spectroscopy and photography. With the ability to split the observed light into different wavelengths, it is not only possible to detect the signature of different elements in the sun, but also to gain information about processes that lead to emission of radiation and processes that influence radiation on its path through space. But not until the beginning of the 20th century astronomers discovered that the solar system is part of the Milky Way, that itself is a galaxy just like billions of other galaxies in the universe.

Today we know that there are structures even much larger than galaxies. While galaxies contain 10^7 to 10^{12} stars in an area of some 10 kpc, galaxy clusters contain about 50 to 1000 galaxies with typical diameters of some Mpc. Galaxy clusters are the largest gravitationally-bound objects in the universe. They are located at intersections of large filaments. Some of them are part of superclusters, that are the largest known structures in the universe and can reach scales of several tenth of Mpc. They are separated from each other by immense voids and loosely connected by elongated filaments. On larger scales the universe is believed to be homogeneous and isotropic in space, as we know from measurements of the cosmic microwave background and from the distribution of galaxies in large sky surveys. Since Hubble formulated his law in 1929, we also know that there is a linear correlation between the distance of an object and its apparent escape velocity, measured by the redshift of its light when it reaches us. This correlation is interpreted as caused by the expansion of the universe.

Furthermore today it is possible to observe objects not only in the optical frequency range, but also in the radio, infrared, ultraviolet, X-ray and gamma. Additionally we are able to measure high-energy particles whose origin is believed to lie outside the solar system or even outside the Milky Way. With these information people were able to realize that the larger part of the universe is not visible.

2.2 Darkness

There seems to be much more matter in the universe than the one that is directly visible. Historically all matter not directly observable was called dark matter, because it does not emit or reflect enough or even any radiation. The first discussions about the nature of dark matter took into account only baryonic dark matter, which is made up of protons and neutrons and therefore is capable to emit radiation. So, as dark matter is not visible, either it does not emit enough radiation or it is hidden by something else. One part of dark matter consists of brown and old white dwarfs, which do not emit enough radiation and are too small to reflect an observable amount of radiation. Attempts have been made to detect such massive, compact, but directly invisible objects indirectly by their influence on the appearance of bright background sources. So when they cross the line of sight of such a background source, they should amplify its brightness because of gravitational lensing. In this case, due to general relativity, the compact object acts as a lens, bending the light of the background source through its gravitational attraction and producing an effect similar to an optical lens. Nevertheless it was shown that there were not enough such objects detected to explain the missing mass. Another possibility is diffuse gas that does not emit enough radiation to be detected. One example is the warm hot intergalactic medium. Although this gas contains about 10 times more mass than there is in stars, it is also not sufficient to account for all missing matter. Additionally there could be objects that basically emit enough radiation to be detectable, but are hidden by something else, i.e. dust or brighter foreground objects.

As we know that the main fraction of the mass in our universe is nonbaryonic, today (and also in the following in this thesis) only this nonbaryonic matter is called dark matter. Nonbaryonic dark matter interacts only gravitationally, so it is not possible to detect it directly, as it does not emit or absorb photons. It can be divided into two types, hot and cold dark matter. Hot dark matter consists of light particles that move with ultrarelativistic speed, while cold dark matter particles have larger rest mass than kinetic

energy and thus move with non-relativistic speed. The only known candidate for hot dark matter are neutrinos, but as there is an experimental upper bound of their mass of 1eV they cannot account for all dark matter. Until now particle physicists do not know any particle that could be a candidate for cold dark matter. However there are many theoretical ideas about particles that interact only via gravity and possibly via weak interaction called WIMPs (Weakly Interacting Massive Particles), for example from supersymmetric particle physics theories.

As dark matter cannot be detected directly, indirect methods have to be used. One of the observations that give a strong hint on the existence of dark matter are rotation curves of galaxies. From them the velocity of objects in a galaxy is measured depending on their distance from the center of the galaxy. This can be done in the inner part of the galaxy with stars and with hydrogen gas in the outer parts. If the galaxy was made up of only visible matter we would expect that far beyond the center of the galaxy (where most of the visible mass is located) the velocity should decrease. This follows easily from the force balance between gravitational and centrifugal forces for a stable orbit around a spherical potential:

$$G\frac{Mm}{r^2} = \frac{mv^2}{r} \tag{1}$$

G is the gravitational constant, M the mass of the galaxy, m the mass of a test object orbiting around the galaxy, r the distance of the object from the center of the galaxy and v its velocity. Simplified this gives for the velocity:

$$v = \sqrt{\frac{GM}{r}} \tag{2}$$

In contrast to these expectations the rotation velocity seems to be constant also for large distances from the center. First measurements of rotation curves in galaxies can be found in review [FG79]. This suggests that either not all physical laws apply for these conditions as we expect, i.e. the law of gravitation or the laws of motion, or that there is an extended dark matter halo. The latter explanation is now widely accepted, because it needs no changes in any fundamental laws of physics and there are other indications that the main fraction of matter is dark.

Another hint on dark matter is given by observations of galaxy clusters. As Fritz Zwicky first realised in the 1930s, most galaxies of a galaxy cluster have too high peculiar velocities to be bound to the cluster by the gravitational

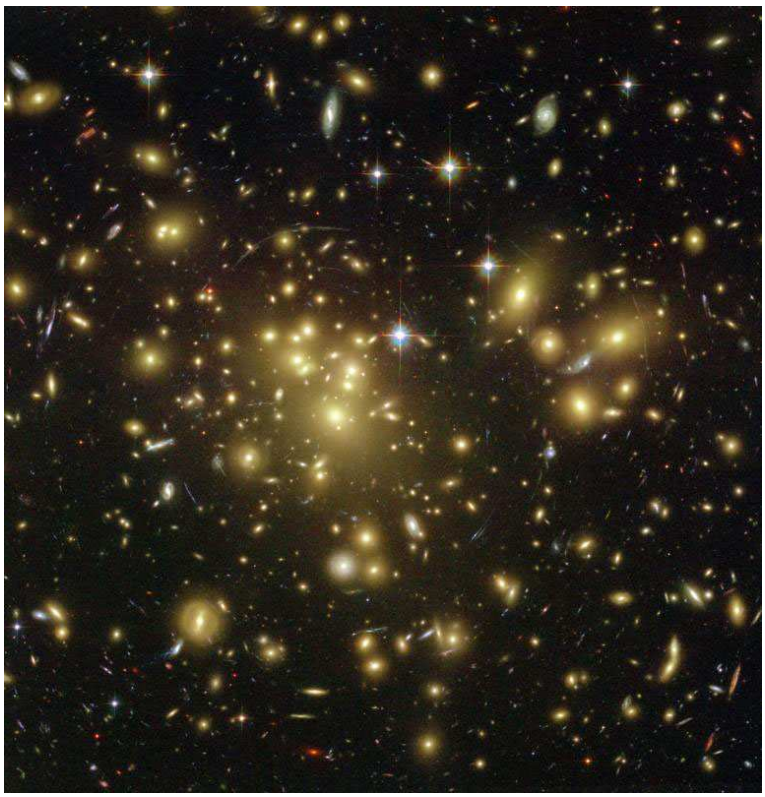

Figure 1: Image of the Abell 1689 cluster acting as gravitational lens observed by Hubble Space Telescope. Around the cluster in the center one can see the elongated arcs. See [XW02] for mass determination of the cluster.

force of the visible part of the cluster. He found that one galaxy cluster he observed needed 400 times more mass than there was visible in stars to explain these velocities. These observations were confirmed later by X-Ray observations of hot intracluster gas. The temperature of this gas is related to the mass of the cluster assuming that cluster and gas are virialized. In this case the time average of the total kinetic energy (that defines the temperature in equilibrium state) equals minus half the time average of the total potential energy. In measurements of the gas temperature, the temperature turned out to be much higher than expected from the visible mass (stars and hot gas) of the cluster, but in agreement with mass estimates from the peculiar velocities of the galaxies.

All these effects were dynamical measurements of the mass of galaxies or galaxy clusters, so they could basically also be caused by some incorrect fundamental laws of dynamics. Additionally there is the possibility to measure

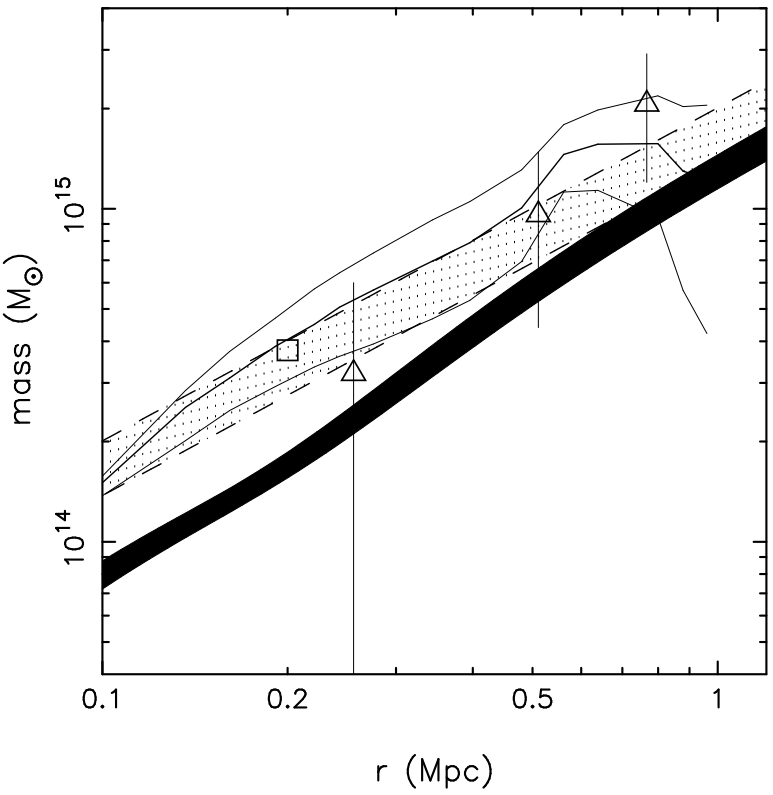

Figure 2: Projected mass distributions of the A1689 clusters from observations of the Chandra satellite (filled region with 90% confidence limits), from strong gravitational lensing (square), the distortion of background galaxy luminosity functions (triangles), the deficit of number counts of red galaxies (solid lines) and the best-fit singular isothermal sphere to the weak lensing data for background galaxy redshifts from z = 0.5 to 3.0 (dashed lines). Figure taken from [XW02].

astrophysical masses through the effect of gravitational lensing. This effect is only based on general relativity and needs no dynamical impact, so it is completely independent of the other methods to determine masses. It uses the distortion of a bright background source by masses along the line of sight. If they are dominated by one very massive object like a galaxy cluster, this object acts as a lens. It then causes a distortion of the background source into arcs. The strength of the distortion measures the mass of the foreground object, typically a galaxy cluster. The results obtained by gravitational lensing agree with the mass estimates from dynamical measurements. One example can be seen in figure 1. A detailed study of the mass distribution of the Abell 1689 cluster with different methods can be found in [XW02]. Its results are shown in figure 2.

2.3 Physical Cosmology

The base of physical cosmology is Albert Einstein's theory of general relativity, that replaced Newton's theory of gravity. In contrast to Newtons's theory that assumed spacetime to be flat, in general relativity spacetime is curved by matter, that in return feels forces depending on the curvature of space. The coupling between curvature and matter is given by the Einstein field equations:

$$G_{\alpha\beta} = \frac{8\pi G}{c^4} T_{\alpha\beta} + \Lambda g_{\alpha\beta} \tag{3}$$

$G_{\alpha\beta}$ is the Einstein tensor, that characterises spacetime, G Newton's gravitational constant, $T_{\alpha\beta}$ the stress-energy tensor, $g_{\alpha\beta}$ the metric of spacetime and Λ the cosmological constant. There is no obvious reason to assume a nonzero cosmological constant. Nevertheless recent observations indicate that it is not only nonzero, but it is the dominant part in the present universe. Today the physical quantity identified with the cosmological constant is called dark energy.
Looking at the universe on very large scales, it seems to be homogeneous and isotropic. In this case the metric of spacetime can be approximated by the Friedmann-Robertson-Walker metric, that can be written as

$$\mathrm{d}s^2 = c^2\mathrm{d}t^2 - a^2(t)(\mathrm{d}r^2 + f^2(r)\mathrm{d}\Omega^2). \tag{4}$$

Here $a(t)$ is a scale factor depending only on time . Therefore expansion has to be isotropic as the scaling has no angular dependencies. As the universe is homogeneous and isotropic, also its curvature is the same in all points of spacetime. The function $f(r)$ depends on the value of the curvature of spacetime.

$$f(r) = \begin{cases} \dfrac{1}{\sqrt{K}} \sin(r\sqrt{K}) \\ \\ r \\ \\ \dfrac{1}{\sqrt{|K|}} \sinh(r\sqrt{|K|}) \end{cases} \tag{5}$$

where K is the radius of curvature. The curvature also determines the type of space:

$K < 0$: hyperbolic space (sum of all angles in a triangle $< 180°$)

$K = 0$: Euclidean space (sum of all angles in a triangle $= 180°$)

$K > 0$: spherical space (sum of all angles in a triangle $> 180°$)

Applying the FRW metric (4) to the Einstein equations (3) we get the Friedmann equations.

$$\begin{aligned} H^2 \equiv \left(\frac{\dot{a}}{a}\right)^2 &= \frac{8\pi G}{3c^2}\left(u + \rho c^2\right) - \frac{Kc^2}{a^2} + \frac{\Lambda c^2}{3} \\ \frac{\ddot{a}}{a} &= -\frac{4\pi G}{3}\left(\rho + \frac{3p}{c^2} + 2u\right) + \frac{\Lambda c^2}{3} \end{aligned} \tag{6}$$

Here ρ and p are homogeneous mass density and pressure, u is the energy density of radiation and H is the newly introduced Hubble function. These equations have 3 independent variables, so to solve them we need an additional equation, that is usually an equation of state $p = p(\rho)$.

In the case of our present universe, that is matter dominated, we can neglect the energy density of radiation and pressure of matter ($u = 0, p = 0$). Applying this to the first Friedmann equation (2.3) and defining the Hubble function at present time H_0, the normalised matter density Ω_m and the normalised cosmological constant Ω_λ as

$$H_0 \equiv H(t_0) \quad \text{(Index 0 represents present time)} \tag{7}$$

$$\Omega_m \equiv \frac{8\pi G}{3H_0^2}\rho_0 \tag{8}$$

$$\Omega_\lambda \equiv \frac{\Lambda c^2}{3H_0^2} \tag{9}$$

we get

$$\frac{H^2}{H_0^2} = \Omega_m \frac{\rho}{\rho_0} + \Omega_\lambda - K\frac{c^2}{a^2 H_0^2}. \tag{10}$$

Looking at this equation for $t = t_0$ and solving for the curvature K we obtain

$$k = (\Omega_m + \Omega_\lambda - 1)\frac{a_0^2}{c^2 H_0^2}. \tag{11}$$

The geometry of the universe depends on the value of K. There are 3 possibilities:

$\Omega_m + \Omega_\lambda < 1 \Rightarrow K < 0$: the universe is open

$\Omega_m + \Omega_\lambda = 1 \Rightarrow K = 0$: the universe is flat (in this case the total density of the universe equals the critical density)

$\Omega_m + \Omega_\lambda > 1 \Rightarrow K > 0$: the universe is closed

The main effect of the expansion of the universe that we can see is the redshift z of light that reaches us from distant sources. Their change in wavelength leads to:

$$z + 1 = \frac{\lambda_0}{\lambda_e} = \frac{a(t_0)}{a(t_e)}, \tag{12}$$

where λ_e is the wavelength of the light that was emitted at time t_e from any source and λ_0 the wavelength that is measured by an observer at time t_0.

The difference between the total emitted luminosity L and the luminosity l an observer measures is called luminosity distance and defined by

$$l = \frac{L}{4\pi D_L^2}. \tag{13}$$

For Euclidean space and small distances it is equal to the distance. In general for a Friedmann-Robertson-Walker metric it is

$$\begin{aligned} D_L &= \frac{(1+z)c}{H_0} \quad f\left(\sqrt{|1-\Omega_m-\Omega_\Lambda|}\times\right. \\ &\times \left.\int_0^z \left[\sqrt{|1-\Omega_m-\Omega_\Lambda|}(1+z')^2 + \Omega_m(1+z')^3 + \Omega_\Lambda\right]^{-1/2} \mathrm{d}z'\right), \end{aligned}$$

where f is the curvature depending function defined in equation 5. For small redshifts $z \leq 0.1$ it reduces to the well known Hubble law.

$$D_L \approx r \approx \frac{cz}{H_0} \tag{14}$$

So the redshift of an object is proportional to its distance. As the redshift was first interpreted as velocity of these objects moving away from us, the Hubble law is also known as "the velocity of distant objects is proportional to their distance".

In addition, the Friedmann solution of the Einstein equations tells us that there was a singularity some time ago, when the universe came into existence. This point is called the Big Bang. Since the total energy within the universe does not change, it had to be very hot and dense in the beginning. Since then it is cooling down while it is expanding.

2.4 Cosmic Microwave Background

As the very early universe was very hot with a very high energy density, all types of particles were created and destroyed in equilibrium. While the

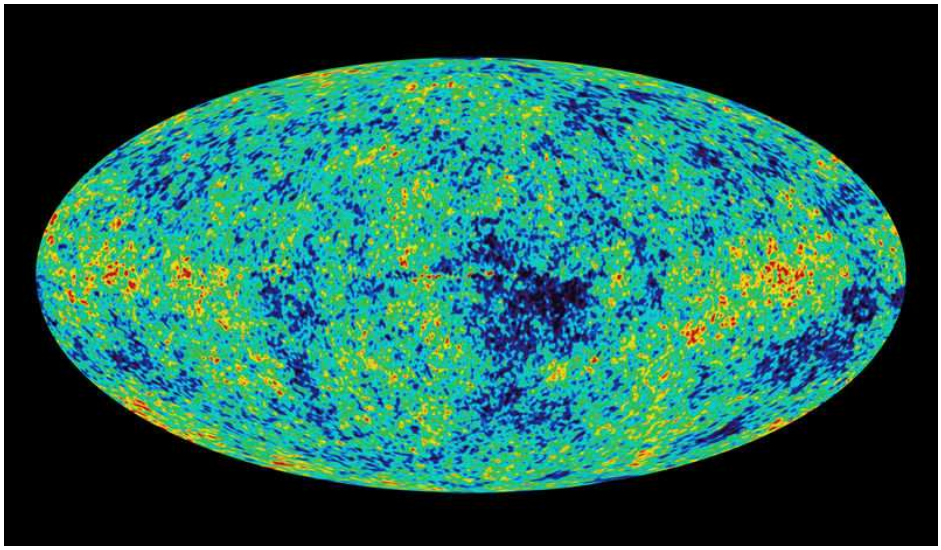

Figure 3: Anisotropies of the cosmic microwave background observed by the WMAP satellite. Image taken from NASA.

universe was cooling down, the energy density decreased and more and more types of particles were destroyed rather than created. So after some time only electrons, protons and neutrons were left, surrounded by photons and constantly interacting with them.

When the temperature of the universe dropped below 3000K, out of energetic reasons it became favorable for electrons and protons to combine to hydrogen atoms. At this time the photons stopped to be scattered, as the baryons were now neutral atoms. After this decoupling the photons were able to propagate freely. The photons cooled down to the present temperature of 2.725K. They are measurable as cosmic microwave background and have a perfect thermal black body spectrum.

However it is not isotropic, but shows some anisotropies on scales of 10^{-5}, that originate on the one hand from effects that happened before the last scattering surface - called primary anisotropies - and on the other hand from secondary anisotropies - effects that changed the photons on its way to the observer. Figure 3 shows the anisotropies of the CMB.

The form and distribution of these anisotropies can be used to constrain the parameters of cosmological models. Before recombination photons that

scatter on the electrons and protons tend to erase anisotropies by their pressure. At the same time the gravitational potential of the protons favors overdense areas to collapse. The interplay of these effects causes acoustic oscillations in the photon-baryon plasma, that can be seen as peaks in the angular power spectrum of the CMB. The location and strength of these peaks depend on the composition and geometry of the universe and hence are used to determine some basic properties of the universe as its curvature (first peak), its baryon density (second peak) and its dark matter density (third peak).

The secondary anisotropies consist of many different effects. They include effects like scattering of the photons on ionized intergalactic gas, gravitational redshift or blueshift of photons by gravitational potentials they cross (Sachs-Wolfe effect) or hot electron gas i.e. in galaxy clusters (Sunyaev-Zel'dovich effect).

2.5 Cosmological parameters

Even earlier, starting about 100 seconds after the big bang for the next 200 seconds, the universe provided conditions of temperature and density favourable for nuclear fusion. During this time most of deuterium, helium-3, helium-4 and lithium-7 that exists today was produced. The produced abundances of these elements only depend on the baryon to photon ratio. They can all be measured for our local universe and agree well with one baryon to photon ratio. All methods described above together yield a consistent picture of our universe, that is flat, 14 billion years old, and consists of 4% baryonic matter, 23% dark matter and 73% dark energy. (See table 1).

Table 1: cosmological parameters from WMAP 3-year data [SBD+06]

Ω_Λ	0.72 ± 0.04
Ω_{Mass}	0.27 ± 0.04
Ω_{Baryon}	0.044 ± 0.004
H_0	$71\ ^{+4}_{-3} \frac{\text{km}}{\text{s Mpc}}$
Age	$(13.7 \pm 0.2) \cdot 10^9$y

2.6 Structure formation

As long as radiation and baryons were coupled, fluctuations in the baryon density were not able to develop, as they were washed out by the photon

field immediately. Dark matter in contrast is not influenced by photons or baryons. So after its decoupling in the first seconds after the Big Bang, dark matter underwent no significant interaction apart from gravity. Therefore initial perturbations as observed in the CMB in the dark matter density were able to grow to the large structures we observe today.

As there is much more dark than baryonic matter in the universe, the evolution of dark matter is hardly influenced by baryonic matter. The best agreement to the formation of the observed present day large scale structures of the universe from given initial perturbations are obtained by the ΛCDM-Model. It assumes the existence of a cosmological constant Λ (dark energy) and dark matter to be cold, i.e. dark matter particles to be nonrelativistic. In this case dark matter density fluctuations grow on small scales first and then merge to larger and larger structures, so the clustering is hierarchical. Along with the dark matter, the baryonic matter gathers in the potential wells of dark matter and forms the visible part of our universe.

On large wavelengths the growth of dark matter density perturbations can be approximated as linear. But on small scales gravitational forces are dominated by nonlinear effects. These effects cannot be treated analytically, so one has to use numerical N-body calculations, which compute the nonlinear equations by integrating the forces numerically.

2.7 Galaxy cluster

Galaxies trace the large scale structure of the universe, as they are positioned along filaments and within clusters of dark matter. Many galaxies in the universe are not isolated, but part of galaxy clusters. Galaxy clusters are gravitationally bound and typically contain several 100 galaxies. But galaxies (including their dominating dark matter part), albeit the most prominent part of galaxy clusters, contribute hardly 10% to the total cluster mass. Another about 10% of the mass consists of baryonic gas. The remaining and dominating part is made up of dark matter, which is also the part that can only be detected indirectly. Typically galaxy clusters are by no means homogeneous, but are composed of smaller substructures, as they are the latest formed objects in the universe and therefore usually still dynamically active. These substructures may be filaments that connect clusters to their neighbours, or results of mergers with other clusters in the past. Clusters and their properties can be observed in two ways, either by the radiation they emit or by their interaction with radiation from background sources. The visible image of a galaxy cluster is often dominated by its central galaxy, that is virtually always also the most massive and brightest galaxy of the

cluster. From galaxy spectra we are able to derive their redshift and thus the velocity of the galaxies relative to us. As the galaxies are bound to the cluster, by removing the velocity of the cluster from the peculiar velocities of the galaxies, we get a velocity dispersion of the galaxies within the gravitational potential of the cluster. This velocity dispersion σ_r of galaxies within a given radius R_G around the cluster center depends only on the mass of the cluster, so we can estimate the mass of a cluster from the velocity dispersion of its galaxies. It can be calculated from the virial theorem

$$M = \frac{3R_G\sigma_r^2}{G}. \tag{15}$$

With typical velocity dispersions of 1000 km/s, galaxy clusters have masses between $10^{14}\mathrm{M}_\odot$ and $10^{15}\mathrm{M}_\odot$. The hot gas between the galaxies emits X-rays via bremsstrahlung. Its typical total X-ray luminosity is about $10^{45}\frac{\mathrm{erg}}{\mathrm{s}}$. The X-ray emissivity of a plasma depends on its temperature and density. For intercluster plasma the mass density can be related to the electron density, as the gas is assumed to be completely ionized and consists of known fractions of hydrogen (0.75) and helium (0.25). The emissivity is given by

$$j(T, n_e) = \frac{4C_j}{1+f}\left(\frac{kT}{\mathrm{keV}}\right)^{1/2}\left(\frac{n_e}{\mathrm{cm}^{-3}}\right)^2\left[e^{\left(-\frac{E_a}{kT}\right)} - e^{\left(-\frac{E_b}{kT}\right)}\right]\frac{\mathrm{erg}}{\mathrm{cm}^{-3}\mathrm{s}^{-1}} \tag{16}$$

where $f = 0.75$ is the mass weighted hydrogen fraction of the gas, $C_j = 2.42\,10^{-24}$ a constant, n_e the electron density and E_a and E_b the lower and upper bounds of the emitted energy. With this equation it is possible to assess the temperature of a cluster from the shape of the observed spectrum. Using the temperature it is possible to estimate the electron density that is usually around $n_e = 10^{-2} - 10^{-3}\mathrm{cm}^{-3}$. Assuming a spherical model and hydrodynamical equilibrium within the cluster, one is then able to evaluate the mass of the cluster.

Beside X-rays, some galaxy clusters also emit smooth radio emissions. This radiation also has no discrete sources, but is thought to originate from synchrotron emission of relativistic electrons in a magnetic field. Assuming equipartition energy conditions a rough estimate of the magnetic field strength can be made. This leads to magnetic field strengths in the range of 1 μG. However this estimate typically assumes equal energy in protons and electrons and the magnetic field to span the whole radio source, disregarding structures within the magnetic field. Today radio emissions are thought to be related to former mergers of the cluster.

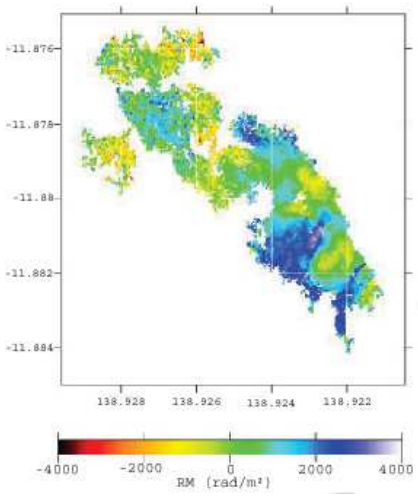

Figure 4: Rotation Measure map of the Hydra A cluster from [VE05].

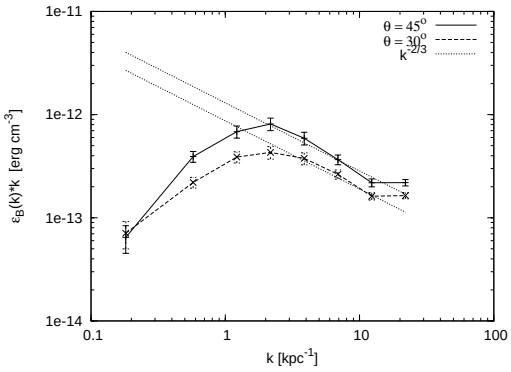

Figure 5: Magnetic power spectrum for the Hydra A cluster for two different inclination angles from [VE05]. Dotted line is a Kolmogorov-like power spectrum for comparison.

To constrain the amount of relativistic electrons one can take advantage of their inverse Compton scattering on photons of the cosmic microwave background. This effect leads to an additional component in the hard X-ray band, but is hard to detect. Although the effect is not directly measurable, upper bounds on these hard X-ray emissions give an upper bound for the relativistic electron density. This density again leads to a lower bound on the magnetic field strength, as the (known) radio luminosity is roughly given by the product of magnetic field strength and relativistic electron density.

A complete different approach is called Faraday rotation measure. It is based upon the fact that magnetised plasma acts as a birefringent lens. Using background synchrotron radiation emitting sources, their radiation, if it is linearly polarised, will change its plane of polarisation when it travels through the plasma. The background source may either be itself part of the cluster or a bright source behind the cluster. The change of polarisation angle is quadratic in wavelength.

$$\Delta\chi = RM \cdot \lambda^2 \tag{17}$$

[DCP87] showed that this change in polarisation cannot be due to a galactic origin or mixing of thermal gas with the radio emitting plasma.

The rotation measure RM depends on electron density and magnetic field along the line sight from the source to the observer.

$$RM = 812 \int_0^L \frac{n_e}{\mathrm{cm}^{-3}} \frac{\vec{B}}{G} \,\mathrm{d}\frac{\vec{l}}{kpc} \frac{\mathrm{rad}}{\mathrm{m}^2} \tag{18}$$

It is important to note that, in contrast to the former methods to measure the magnetic field, the rotation measure depends only on the component of the magnetic field parallel to the line of sight. Also the rotation measure is ambiguous for changes in position angle larger than π (not 2π, as polarisation does not have a direction). The latter problem can partly be solved by measuring at many different wavelengths. Characteristic values for the strength of cluster magnetic fields estimated by Faraday rotation measure maps are some μG.

Historically all these methods agreed on the order of magnitude of the magnetic field strength, but showed some systematic deviations. However, recent observations show structures within the magnetic fields on all scales. Using improved models that take these structures into account and also removing some other simplifications, results seem to agree well with each other. Also RM maps measure only one component of the magnetic field, meanwhile the other estimates include the complete magnetic field.

Figure 4 shows an observed RM map of the Hydra A cluster. It reaches maximum values between -4000 and 4000 with larger regions that have values larger than 2000 or smaller than -2000. The magnetic power spectrum of the cluster obtained from this RM map by a Bayesian likelihood method [VE05] is shown in figure 5. It increases for large k (on large scales), reaches a maximum at about 3 $\frac{1}{\mathrm{kpc}}$ and decreases for larger k (smaller scales). One can see that the slope of the decreasing part of the power spectrum follows a Kolmogorov spectrum (that means a spectral index of -2/3 for this plot), that is expected in case of magnetic turbulence, for nearly one order of magnitude from about 2 $\frac{1}{kpc}$ to 10 $\frac{1}{kpc}$.

Another approach to measure the spectral index of the power spectrum of the magnetic field is shown in figure 6 ([MGF$^+$04]). It shows the ratio between the absolute value of the mean of the rotation measure and the standard deviation of the rotation measure of different clusters depending on the size of the RM map. As the mean may always be smaller or even go to zero, the ratios can only be used as lower bound. They show that there are many spectral indexes that are larger than 1 and some that are larger than 2. It is important to note that here the spectral index is defined as $|B_k|^2 = C_n^2 k^{-n}$ with a normalisation constant C_n^2. Therefore a Kolmogorov spectrum has a spectral index of 11/3.

While recent observations are able, as seen above, not only to estimate the magnetic field as a whole, but also to resolve enough structures to calculate magnetic power spectra, spectral indexes or the magnetic autocorrelation length ([Gov03], [MGF$^+$04], [VE03], [VE05], [GMF$^+$06]), it is now of interest to compute these properties also from numerical simulations to compare them with observations.

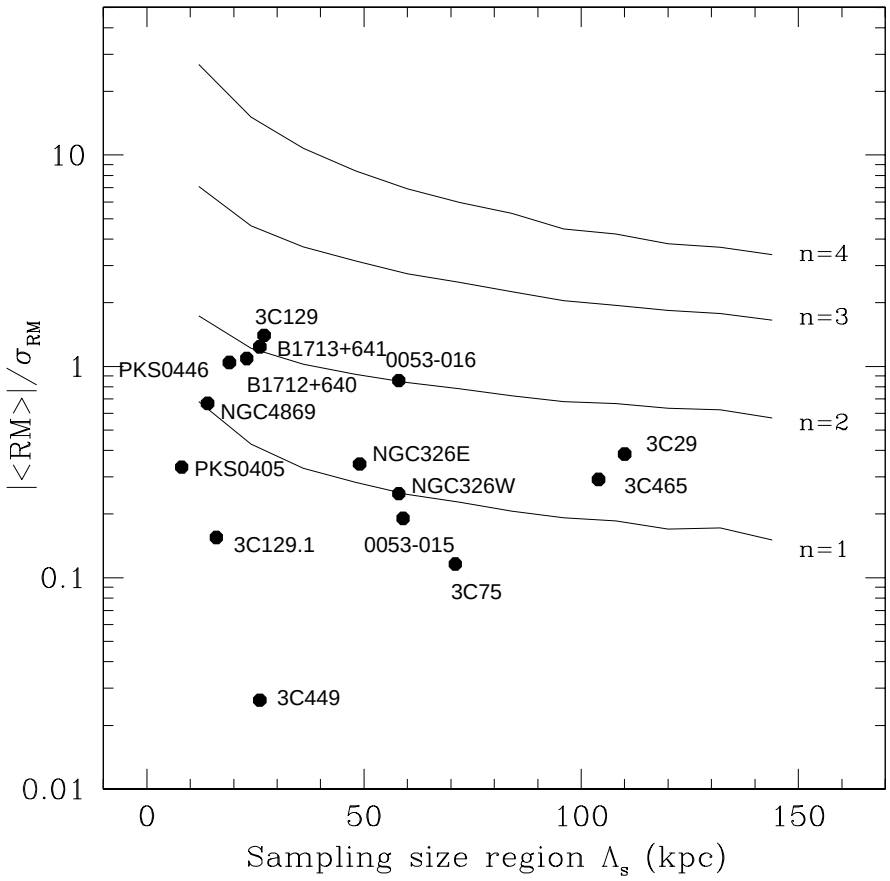

Figure 6: Ratio of the mean of the rotation measure $| < RM > |$ and its standard deviation σ_{RM} as a function of the size of the sampling region for different clusters. Lines correspond to simulated RM maps for magnetic fields with spectral indexes of 1, 2, 3 and 4. Figure taken from [MGF+04].

3 Simulations

As the dominant fraction of mass in the universe is dark matter, that only interacts via gravitation, the easiest way to simulate the formation of large scale structure is to simulate only dark matter, and neglect effects from baryons and photons. So the task is to accurately calculate the gravitational forces. Usually dark matter is simulated using N-body techniques. In this case the universe is modelled with a large number of massive particles (the Millennium simulation used more than 10 billion particles). N-body simulations have the advantage that they are able to cover a wide dynamical range in space without additional efforts like refining a grid, since there will be intrinsically more particles in regions of higher density, giving a better resolution there.

These simulations start from initial density perturbations based on data measured from the CMB, that are discretised by the particles. Using co-moving coordinates, the effects of general relativity can usually be neglected except a global time dependent scaling function, as dynamical timescales are much larger than the propagation timescale of changes in the gravitational field and the mass of the particles is not large enough to have an effect on the local curvature of spacetime. So all one has to do is to compute the Newtonian gravitational forces between particles. But since each particle exerts a different force on each other particle, the number of operations needed to calculate the forces increases quadratically with the number of particles. Therefore the only way to compute the gravitational forces exactly for a large number of particles is to use special hardware that was created for this purpose only. Another way is to use approximations like tree methods or particles mesh methods.The best balance between accuracy and performing is achieved by combining different approximations for different scales. For details how the GADGET code treats them, see [Spr05].

There are basically two ways to compare the results achieved from dark matter only simulations to our observable universe. So it is reasonable to assume the baryons, that are much less than dark matter, follow the gravitational potential of the dark matter. Therefore one can directly compare the dark matter density distribution with observed large scale structures from the galaxy and galaxy cluster distribution in our universe. Another way is to use semianalytic models to model the behavior of baryonic matter, i.e. galaxies, within the dark matter background.

But there are many aspects and models where these simplifications do not hold. So it is not feasible to compute the evolution of magnetic fields or intercluster gas in the post processing of dark matter only simulations. So to do them, one has to include baryons in the simulation from the beginning. Due to several reasons, simulations that include baryonic matter are more difficult, both for physical and numerical reasons. Interaction of baryonic matter is not dominated by gravity, but by electromagnetic forces. This means that some of the effects of radiative heating and cooling, magnetic fields, star formation, nuclear reactions or shocks have to be taken into account. These effects are not easy to treat, as magnetic fields for example are expensive in computation and add numerical problems like a nonzero divergence of the magnetic field in contradiction to the Maxwell equations. Some effects are even impossible to handle in cosmological simulations, as the resolution is far away from the required one or the effect is itself not yet entirely understood. So one has to approximate such effects with models, that were derived from other sources.

However to follow the evolution of baryonic matter is the only way to understand where and how stars are formed, how magnetic fields are amplified from seed fields and why galaxies look like they are observed today.

SPH-Simulations

As the evolution of the baryons is mainly given by hydrodynamics, one has to find a way to use N-body techniques and hydrodynamics together. An elegant way to make this possible is the smoothed particle hydrodynamics formalism ([Luc77], [GM77]). It discretises the fluid into "fluid particles". But in contrast to the N-body formalism, where the particles are point-particles, SPH particles have a finite spatial extend. Their physical properties are smoothed over this extend by a kernel function. The algorithm that determines the size of the particles guarantees that in all points in space there overlap some particles. So it is possible to calculate any property at any point in space from all particles that overlap with this point.

Like N-body techniques, the SPH formalism has the advantage that it is an adaptive method by definition. Also it does not need any grid, since all quantities and their derivatives can be computed from the kernel function. Last but not least, the gravitational forces are easy to compute by handling the SPH particles like the dark matter point particles.

The base of the SPH formalism is the interpolation of a quantity A, that is given by

$$\langle A(\vec{r})\rangle = \int A(\vec{r}')W(\vec{r}-\vec{r}',h)d^3\vec{r}' \tag{19}$$

The kernel function $W(\vec{r}-\vec{r}',h)$ has to be standardised

$$\int W(\vec{r}-\vec{r}',h)d^3\vec{r}' = 1 \tag{20}$$

and transform into the delta function in the limit of h going to zero

$$\lim_{h\to 0}(W(\vec{r}-\vec{r}',h)) = \delta(\vec{r}-\vec{r}'). \tag{21}$$

To separate the continuum into mass elements one has to expand equation 19 by the density and to approximate the integral as a finite sum.

$$\langle A(\vec{r})\rangle = \int \frac{A(\vec{r}')}{\rho(\vec{r}')}W(\vec{r}-\vec{r}',h)\rho(\vec{r}')d^3\vec{r}' \approx \sum_i m_i \frac{A_i}{\rho(\vec{r}_i)}W(\vec{r}-\vec{r}_i,h) \tag{22}$$

In this case m_i and A_i are given as properties of particle i at position $\vec{r}_i$. m_i is the mass associated with the particle, that can be identified with the product of its density and volume element $\rho(\vec{r}')d^3\vec{r}'$. $\rho(\vec{r}_i)$ has to be calculated itself by equation 22, that leads to

$$\langle \rho(\vec{r}_j)\rangle = \sum_i m_i W(\vec{r}_j-\vec{r}_i,h) \tag{23}$$

Considering a differential operator $\nabla\langle A(\vec{r})\rangle$ that acts on r, we get from equation 22

$$\nabla\langle A(\vec{r})\rangle = \sum_b m_b \frac{A_b}{\rho(\vec{r}_b)}\nabla W(\vec{r}-\vec{r}_b,h). \tag{24}$$

Here the differential operator only acts on the kernel function. So as the kernel function is the same all the time, its derivative can be calculated analytically and has not to be computed numerically.

An additional advantage of the SPH formalism is the possibility to assign a different smoothing length to each particle, and to change it with time. So it is possible to have smaller smoothing lengths and therefore a better resolution in regions of higher interest, and larger smoothing lengths in areas that are less interesting. There are different methods to choose the smoothing length of a particle. One is to link the smoothing length of a particle directly to the density at the position of the particle. Therefore the resolution scales with density, and one has the best resolution where the density is maximal.

Another method is to define the number of neighbours each particle has as constant.

All simulations I analysed were done with the open code GADGET [Spr05]. For gas particles it uses the kernel function

$$W(\vec{r},h) = \frac{1}{h^3}\begin{cases} \frac{8}{\pi}(1-6u^2+6u^3) & 0 \leq \frac{r}{h} \leq \frac{1}{2} \\ \\ \frac{8}{\pi}2(1-u)^3 & \frac{1}{2} \leq \frac{r}{h} \leq 1 \end{cases} \tag{25}$$

where r is the distance to the center of the particle, h the variable smoothing length of the particle, and $u = r/h$. This kernel function is approximately gaussian but is nonzero only over a finite area.

It binds the adaptive smoothing length h of each particle to the density at the position of the particle to have a constant mass within the kernel volume. This is equal to the condition

$$\frac{4\pi}{3}h_i^3\rho_i = N_{sph}\overline{m}, \tag{26}$$

where h_i is the smoothing length of the i-th particle, ρ_i its density, N_{sph} the typical number of smoothing neighbours and $\overline{m}$ the average mass of a particle.

To evolve the SPH fluid with time, one has to implement the hydrodynamical equations into the SPH formalism. As showed by [SH02], discretising the fluid Lagrangian leads to the equations of motion for the SPH particles

$$\frac{\mathrm{d}\vec{v}_i}{\mathrm{d}t} = -\sum_{j=1}^{N} m_j \left[f_i \frac{P_i}{\rho_i^2}\nabla_i W(\vec{r}_i - \vec{r}_j, h_i) + f_k \frac{P_k}{\rho_k^2}\nabla_i W(\vec{r}_i - \vec{r}_j, h_j)\right], \tag{27}$$

where the f_i is defined as

$$f_i = \left(1 + \frac{h_i}{3\rho_i}\frac{\partial\rho_i}{\partial h_i}\right)^{-1}. \tag{28}$$

The particle pressure P_i is given by the entropy A_i and density ρ_i of the particle.

$$P_i = A_i\rho_i^{\gamma} \tag{29}$$

As equation of state it is assumed that the gas behaves as an ideal gas. To prevent these ideal gas from developing discontinuities, an artificial viscosity is used.

$$\left.\frac{\mathrm{d}\vec{v}_i}{\mathrm{d}t}\right|_{visc} = -\sum_{j=1}^{N} m_j \Pi_{ij}\nabla_i\overline{W_{ij}} \tag{30}$$

Here $\overline{W_{ij}}$ is the arithmetic average of the two kernels $W(\vec{r}_i - \vec{r}_j, h_i)$ and $W(\vec{r}_i - \vec{r}_j, h_j)$ and Π_{ij} is the pressure tensor. It may take different forms, however one often used is the parametrisation given by [GM83]. The artificial viscosity generates entropy at a rate

$$\frac{\mathrm{d}A_i}{\mathrm{d}t} = \frac{1}{2}\frac{\gamma - 1}{\rho_i^{\gamma-1}} \sum_{j=1}^{N} m_j \Pi_{ij} \vec{v}_{ij} \cdot \nabla_i \overline{W_{ij}}, \tag{31}$$

where $\vec{v}_{ij} = \vec{v}_i - \vec{v}_j$.

In the same way as the hydrodynamical equations, also the magnetohydronamical equations can be applied to the SPH formalism. The intercluster gas has in good approximation no charges, no currents and an infinite conductivity. Therefore one gets two additional equations. One the one hand the magnetic field exerts the Lorentz force on the particles, on the other hand the motion of the particles changes the magnetic field via the induction equation.

The Lorentz force adds one additional term to the motion equation 27 of the particle. It can be written as

$$\frac{\mathrm{d}\vec{v}_i}{\mathrm{d}t} = \sum_{j=1}^{N} \frac{m_j}{4\pi} \left[\left(\frac{\mathcal{M}}{\rho^2} \right)_i + \left(\frac{\mathcal{M}}{\rho^2} \right)_j \right] \cdot \overline{W_{ij}}, \tag{32}$$

where the Maxwell tensor $\mathcal{M}_i$ is defined as

$$\mathcal{M}_{i,ab} = \vec{B}_{i,a} \vec{B}_{i,b} - \frac{1}{2} |\vec{B}_i|^2 \delta_{ab}. \tag{33}$$

The induction equation changes the magnetic field according to the motions of the particles. It is given by

$$\frac{\mathrm{d}\vec{B}_{i,k}}{\mathrm{d}t} = \frac{1}{\rho_i} \sum_{j=1}^{N} m_j \left(\vec{B}_{i,k}(\vec{v}_i - \vec{v}_j) - \vec{B}_i(\vec{v}_i - \vec{v}_j), k \right) \nabla_i \overline{W_{ij}}, \tag{34}$$

where $, k$ represents the k-th component of a vector.

To improve the treatment of magnetic field in the SPH formalism, the part of the magnetic force that is proportional to the divergence of the magnetic field is subtracted explicitly, as described by [BOT01]. This on the one hand prevents the development of numerically induced divergence beyond a negligible level and on the other hand avoids an well-known instability of this SPH-MHD formulation in areas where the magnetic field pressure exceeds the thermal pressure significantly.

Also the magnetic field of each particle is periodically smoothed with the smoothing length of this particle. As the evolution of the magnetic field carries magnetic energy from larger to smaller and smaller scales, this is done to compensate that there is no explicit dissipation of magnetic fields at small scales. It is described in detail in [BOT01].

The SPH formalism defined in this way is able to calculate the value of each quantity at any point in space from the properties of all nearby particles that overlap the desired point, as the kernel function is zero for $r > h$. To compute gas and its magnetic field, additional initial conditions both the gas and the magnetic field are needed. From these initial conditions the SPH particles evolve in the same way as the dark matter particles, but with additional forces.

4 Calculating the grid

The calculation of the grid out of the SPH simulation is not trivial. On the one hand it is limited by the available amount of memory and computational time. It is a problem since the SPH simulation is adaptive and covers a wide dynamical range of up to 5 orders of magnitude, so a uniform grid that resolves and covers the simulation completely would have to be huge and is therefore not affordable. The more particles overlap with a single grid cell, the more expensive is the computation. On the other hand the quantities that are preserved in the transformation of the particle simulation onto the grid depend on the details of the used method. So the goal is to find a method for the calculation of the grid that preserves as much information as possible while the amount of memory and computational time it needs stays within usable limits.

Our SPH simulations contain some million particles. The galaxy cluster itself is made up by more than one million particles.

4.1 Different methods to calculate a grid

4.1.1 Method 1: SPH

The simplest way to calculate the quantities in a grid cell is to use the values provided by the SPH formalism for the center of the grid cell. So we get

$$A(j,k,l) = \sum_i m_i \frac{A_i}{\rho(\vec{r}_i)} W(\vec{x}_{j,k,l} - \vec{r}_i, h_i), \tag{35}$$

where $\vec{x}_{j,k,l}$ is the coordinate of the center of the cell with indexes j, k and l. If the resolution of the grid is fine enough to resolve the simulation completely, i.e. when the size of a grid cell is smaller the smallest particle, this method should give nearly perfect results. However it has comparably high computational costs for good resolutions, because each particle contributes to a large number of grid cells. On the other side, if the resolution is low, one will completely miss some particles that fall through the grid. Even though the quantity is exact at all points of the grid, integrated quantities like the total mass within a volume may become compromised in this case.

4.1.2 Method 2: Average SPH

The second method is similar to the first method, but takes into account not only the center of the grid cell, but 8 points around it. Therefore it only

requires as much memory for the grid as method 1 and takes into account more information, but has about 9 times higher computational costs.

$$\begin{aligned} A(j,k,l) = \tfrac{1}{9}\,(\quad & \sum_i m_i \tfrac{A_i}{\rho(\vec{r}_i)} W(\vec{x}_{j,k,l} - \vec{r}_i, h_i) + \\ & \sum_i m_i \tfrac{A_i}{\rho(\vec{r}_i)} W(\vec{x}_{j,k,l} + \tfrac{a}{\sqrt{3.0}}(1,1,1) - \vec{r}_i, h_i) + \\ & \sum_i m_i \tfrac{A_i}{\rho(\vec{r}_i)} W(\vec{x}_{j,k,l} + \tfrac{a}{\sqrt{3.0}}(-1,1,1) - \vec{r}_i, h_i) + \\ & \sum_i m_i \tfrac{A_i}{\rho(\vec{r}_i)} W(\vec{x}_{j,k,l} + \tfrac{a}{\sqrt{3.0}}(1,-1,1) - \vec{r}_i, h_i) + \quad ...) \end{aligned} \tag{36}$$

where a is the size of the grid cell. In case of a high resolution this method should give the same results like method 1, when the value of the quantity is constant within the grid cell. On the other hand, if the quantity has a large variation within the grid cell, the result will differ. This should match for example the total mass within the grid better, if the density is computed this way, than by method 1.

4.1.3 Method 3: broadened SPH

This method is again nearly the same as method one, but uses a different smoothing length. To prevent particles from falling through the grid, the width of one grid cell is added to the smoothing length of the particle. Therefore it is possible to use a sparse grid, that reduces the computational costs. However it introduces an additional smoothing.

$$A(j,k,l) = \sum_i m_i \frac{A_i}{\rho(\vec{r}_i)} W(\vec{x}_{j,k,l} - \vec{r}_i, h_i + a). \tag{37}$$

where a is the size of the grid cell. This mainly affects particles that have a smoothing length smaller than or comparable with the size of a grid cell. These particles are usually in areas of high mass density and therefore high particle density and good resolution. Particles that are much larger than a grid cell should see nearly no effect. This method guarantees that all particles are taken into account.

4.1.4 Method 4: Sort

Another entirely different approach is method 4. Here particles where treated as point particles and contribute only to the cell their center lies in. To get the normalisation right, it is necessary to multiply the quantities of the particle with the volume of the particle and divide by the volume of the grid cell.

$$A(j,k,l) = \sum_i A_i \frac{V_i}{V_{Cell}} = \sum_i A_i \frac{\frac{m_i}{\rho_i}}{V_{Cell}} \tag{38}$$

where i is running over all particles that have their center within the cell. As this method completely ignores the spatial extend of the SPH particles, it is only usable for effects on scales larger than the typical smoothing length of most particles. Also it has the problem that even for medium size grids, it will lead to empty cells.

4.1.5 Method 5: Triangular Shaped Cloud

The Triangular Shaped Cloud (TSC) method, as described in [HE88], is one way to assign a weighting function to the quantities of the particles. Unlike the smoothing kernel it is not spherically symmetric, but it has the advantage to be simple enough that it is possible to integrate the weighting function over the grid cell. It is one at the point of the particle and decreases linearly. In one dimension it is

$$w(x) = \begin{cases} 1 - |x| & |x| \leq 1 \\ \\ 0 & |x| > 1 \end{cases} \tag{39}$$

where x is the normalised distance to the center of the particle. The three-dimensional weighting function is made up by the multiplication of one one-dimensional function for each dimension. As it is very simple, it is the most used method to map a particle simulation onto a grid.

$$W(x, y, z) = w(x)w(y)w(z) \tag{40}$$

W is normalised by

$$\int_{-\infty}^{\infty} W(x, y, z) \quad dx\ dy\ dz = 1. \tag{41}$$

So the value of a quantity A for a grid cell becomes

$$\begin{aligned} A(j,k,l) = \quad & \sum_i \int_{x_0-a/2}^{x_0+a/2} \int_{y_0-a/2}^{y_0+a/2} \int_{z_0-a/2}^{z_0+a/2} W(\frac{x_i - x_0 + x}{a}, \frac{y_i - y_0 + y}{a}, \frac{z_i - z_0 + z}{a}) \\ & \times \quad A_i \quad \frac{m_i/\rho_i}{V_{Cell}} \quad dx\ dy\ dz \end{aligned} \tag{42}$$

Here x_0, y_0 and z_0 are the coordinates of the center of the cell, a is the size of the cell and x_i, y_i and z_i are the coordinates of the center of the i-th particle. Since the weighting function $W(x, y, z)$ is normalised and the integration

can be done analytically, this method is able to conserve some integrated quantities like the total mass within the grid. It has a limited number of cells that can be affected by a particle, so it is faster than other methods for large particles. But it will produce errors, if the grid cell size is smaller than the smoothing length of the particle. The TSC method also creates empty cells in the outer, low density regions of the simulation, where the smoothing lengths of the particles are much larger than the grid cells and therefore there are very few particles per grid cell.

4.1.6 Method 6: modified TSC

It is possible to eliminate the last problem by modifying the TSC method. This is achieved by using the smoothing length of the particle as width of the cloud instead of the grid cell size. This leads to

$$A(j,k,l) = \sum_i \int_{x_0-a/2}^{x_0+a/2} \int_{y_0-a/2}^{y_0+a/2} \int_{z_0-a/2}^{z_0+a/2} W(\frac{x_i-x_0+x}{h_i}, \frac{y_i-y_0+y}{h_i}, \frac{z_i-z_0+z}{h_i}) \cdot \times \quad A_i \quad \frac{m_i/\rho_i}{V_{Cell}} \quad dx\ dy\ dz \tag{43}$$

The normalisation is still valid after the modification. However the computational effort increases when particles cover a large number of cells now.

4.2 Comparison of the different methods

To see how theses methods behave for different grid resolutions I did some tests. Therefore I compared the grid calculated by methods 2-6 with the grid calculated by method 1 for each resolution. I chose method 1 as reference, as it simply represents the definition of the formalism. I evaluated the relative difference by

$$\Delta A = \frac{1}{N} \sum_{i=1}^{N} \left(\frac{A_i - A_{ref,i}}{\mathrm{Max}(A_i, A_{ref,i})} \right)^2 \tag{44}$$

where N is the number of grid cells. The maximum in the denominator is used to avoid very large differences for values of the denominator close to zero, where the relative difference can be arbitrarily high and dominate the complete sum, but the absolute difference is comparatively small. I did theses difference tests for 3 quantities, density, the norm of the magnetic field and the x-component of the magnetic field. All grid tests were done on the g72 cluster of the Hutt simulation (see chapter 6). The boxes that were used to

Table 2: Size of grid cells

Resolution	Cellsize (kpc) for box:		
	8000kpc	2000kpc	500kpc
256	31.3	7.81	1.95
128	62.5	15.63	3.90
64	125.0	31.25	7.81
32	250.0	62.50	15.63
16	500.0	125.00	31.25

Table 3: Mean number of particles per cell

Resolution	Cellsize (kpc) for box:		
	8000kpc	2000kpc	500kpc
256	$6.59 \cdot 10^{-2}$	$2.46 \cdot 10^{-2}$	$3.20 \cdot 10^{-3}$
128	$5.28 \cdot 10^{-1}$	$1.97 \cdot 10^{-1}$	$2.56 \cdot 10^{-2}$
64	4.22	1.58	$2.04 \cdot 10^{-1}$
32	33.8	12.6	1.64
16	270	101	13.2

calculate the grid had a size of 500 kpc, 2000 kpc and 8000 kpc and were centered at the center of the cluster. For the cell size for each resolution see table 2. Table 3 shows the mean number of particles for a given resolution and box size. The maximum, average and minimum smoothing length of all particles within boxes of different size is given in table 4. The vertical black dashed line always shows the resolution where averaged every second cell is empty.

Figures 7, 8 and 9 show the mean difference in density of the methods for 5 different resolutions from 16^3 to 256^3 gridpoints and 3 different box sizes of 8000 kpc, 2000 kpc and 500 kpc. The different boxes basically differ in

Table 4: Smoothing length of the particles within the box

Smoothing length (kpc) for box size	8000 kpc	2000 kpc	500 kpc
minimum	8.44	8.44	8.44
average	96.7	41.3	22.0
maximum	516	134	39.4

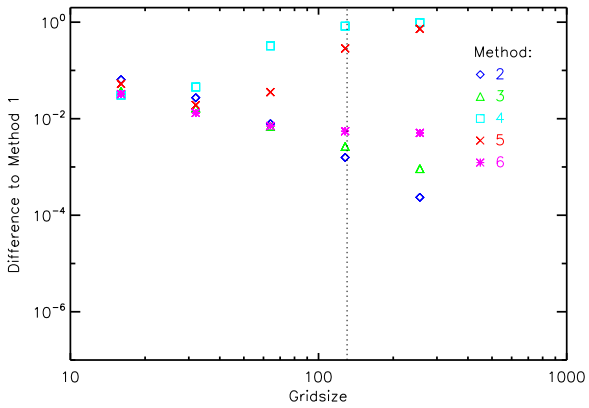

Figure 7: Mass density difference for box size 8000 kpc

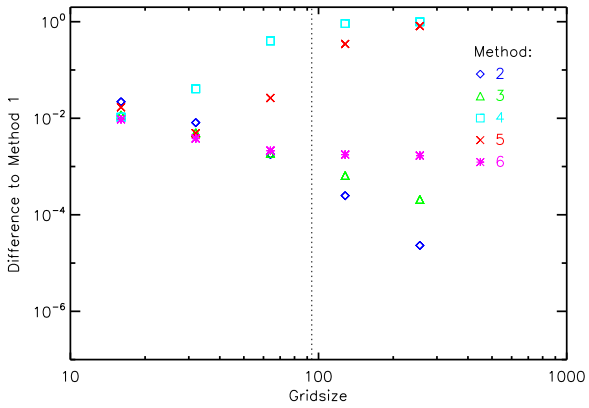

Figure 8: Mass density difference for box size 2000 kpc

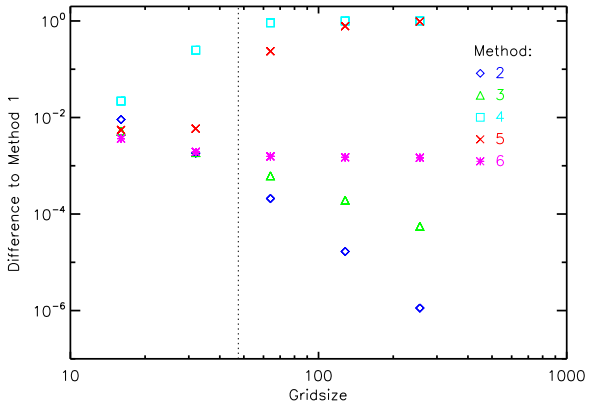

Figure 9: Mass density difference for box size 500 kpc

the average particle size, as SPH simulation has a dynamical resolution. The average particles size becomes smaller with decreasing box size, because the box is centered on the center of the cluster, where mass density and particle number density are maximal. Therefore with decreasing box size the average density increases and the average smoothing length of the particles decreases. Also for equal resolutions the size of a grid cell will be smaller if the box size is smaller.

The behavior is in principle the same for all box sizes. For the lowest resolution it does not make a significant difference, which method is chosen, as the differences are smoothed out. With increasing resolution methods 4 (Sort) and 5 (TSC) become worse until they give completely different results than method 1 (SPH). This is due to the fact that theses two methods reduce the size of the particles when the resolution is much smaller then the typical size of a particle, because the seffective size of the particles is reduced to the size of the grid cell, neglecting the smoothing length of the particle. Here it is interesting to note, that the TSC method is still widely used. Method 2 (av. SPH) agrees best with method 1 for the highest resolution, as expected. Method 6 (mod. TSC) has a constant difference for a resolution of 64^3 gridpoints or higher. The reason of this may be the use of a cubic linear weighting function in contrast to the spherical gaussian-like SPH kernel of method 1, leading to a systematic difference. The difference between method 3 (broad SPH) and 1 decreases linearly with increasing resolution, since the smoothing length used equals the original smoothing length when the grid cells are much smaller than the original smoothing length. Its difference decreases not as fast as the difference between method 2 and 1.

The main difference between the boxes is the size of the difference of the values. It decreases with decreasing box size for equal resolutions.

Figures 10, 11 and 12 show the differences of the norm of the magnetic field for box sizes of 8000 kpc, 2000 kpc and 500 kpc. Like figures 13, 14 and 15 which do the same for the x component of the magnetic field, they show basically the same behavior as the density differences described above. The main difference arises from the fact that the mass density is always larger or equal to zero, while the magnetic field vector and its components can also be negative. Hence they can compensate each other, which may increase the error, as the mean of the quantities is not equal to the mean of the absolute value of the quantity $| < \vec{B} > | \neq < |\vec{B}| >$.

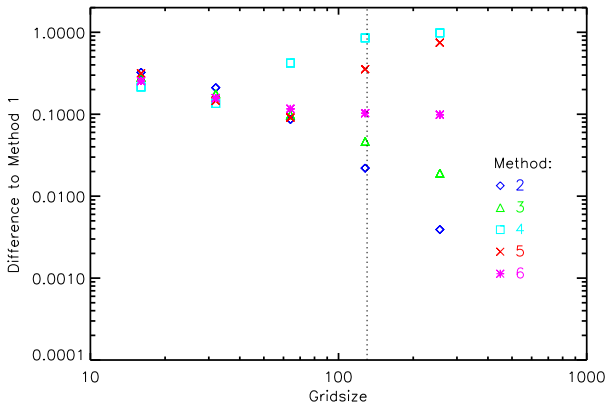

Figure 10: Difference of the norm of the mag. field for box size 8000 kpc.

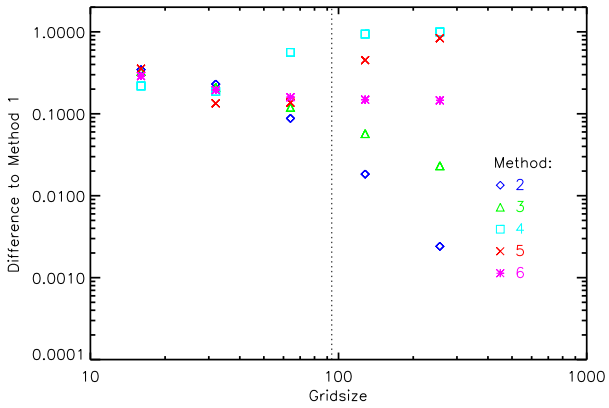

Figure 11: Difference of the norm of the mag. field for box size 2000 kpc.

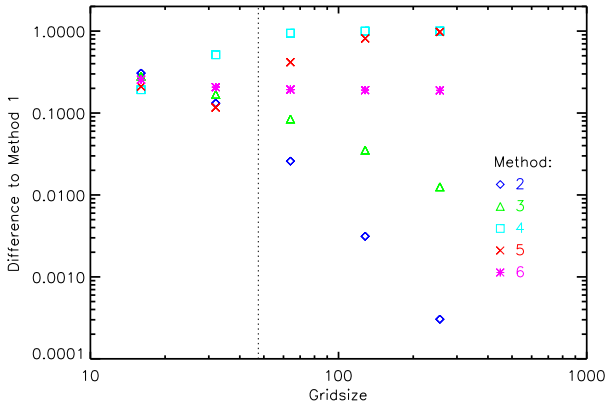

Figure 12: Difference of the norm of the mag. field for box size 500 kpc.

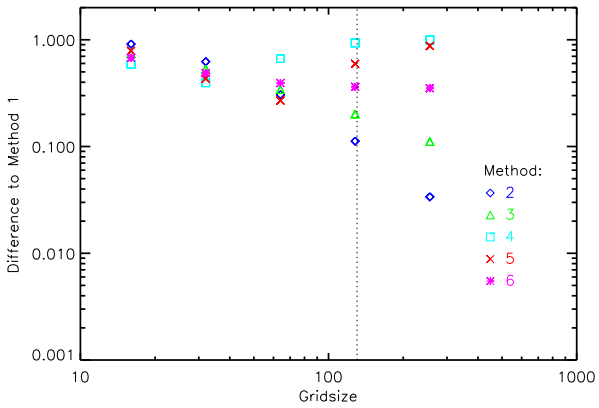

Figure 13: Difference of the x-component of the mag. field for box size 8000 kpc

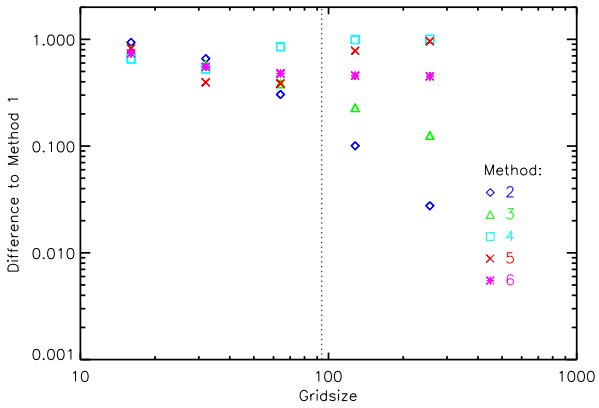

Figure 14: Difference of the x-component of the mag. field for box size 2000 kpc

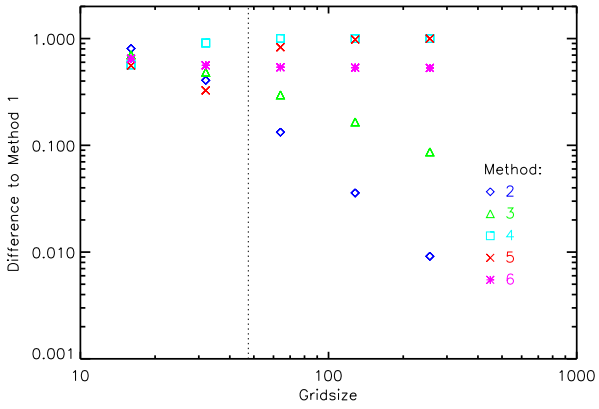

Figure 15: Difference of the x-component of the mag. field for box size 500 kpc

4.3 Projected maps

Although it is not feasible to compute exact values of all (especially integrated) quantities on a grid, this is possible for two-dimensional line of sight integration maps. It is done by calculating the integral by summation over all particles and using the part of the particle that lies within the cube of sight. Because it neglects annihilation effects that happen i.e. when two overlapping particles have magnetic fields with opposite directions, its results are only comparable for scalars like the mass density.

So to compare the results of the different methods with the values of such a projected map, I first integrated the grid along one axis.

$$\rho'_{x_3}(x_1, x_2) = \sum_{x_3} \rho(x_1, x_2, x_3) \tag{45}$$

Then I compared the resulting 2d maps (one for each coordinate) with these maps.

$$\Delta\rho' = \frac{1}{3N} \sum_{i=1}^{3} \sum_{j=1}^{N} \left(\frac{\rho'_{x_i,j} - \rho_{x_i,j}}{\rho_{x_i,j}} \right)^2 \tag{46}$$

where i indicates the line of sight direction of the map, $\rho'_{x_i,j}$ is the j-th cell of the map that was generated by integration along the x_i-axis, $\rho_{x_i,j}$ the equivalent cell of the projected map and N is the number of cells of the map. The differences for box sizes of 8000 kpc, 2000 kpc and 500 kpc can be seen in figures 16, 17 and 18. In contrast to the comparison of the methods with method 1, the evolution of these differences depends on the size of the box.

For the 8000 kpc box, that has the largest dynamical range, there are 2 different types of behavior. Method 4 (Sort) and method 5 (TSC) show an increasing difference with increasing resolution, while method 4 produces the best result for the lowest resolution. The differences of the other methods first decrease with increasing resolution until they reache a constant value. Methods 1 (SPH), 2 (av. SPH) and 3 (broad. SPH) reach a difference that is about one order of magnitude smaller than the difference of method 6. For the 500 kpc box the difference of these 3 methods converge to the same value. For larger boxes method 1 seems to be a bit better than method 2 and 3. The difference of method 6 at high resolutions stays nearly constant for different box sizes.

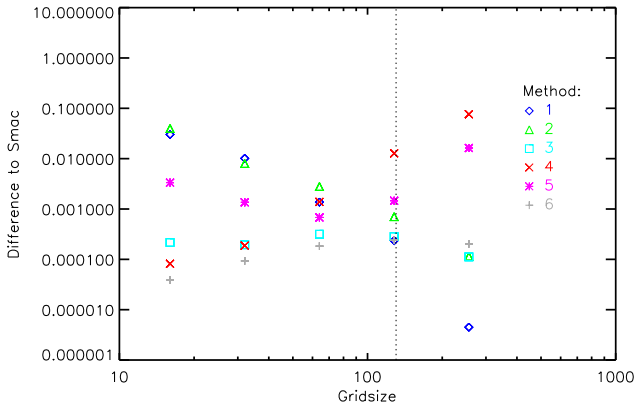

Figure 16: Difference to projected map for box size 8000 kpc

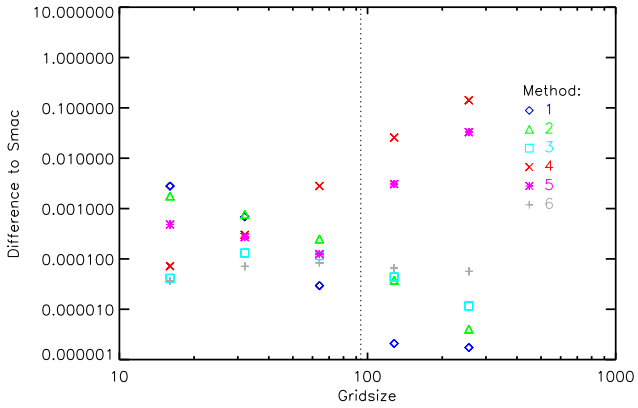

Figure 17: Difference to projected map for box size 2000 kpc

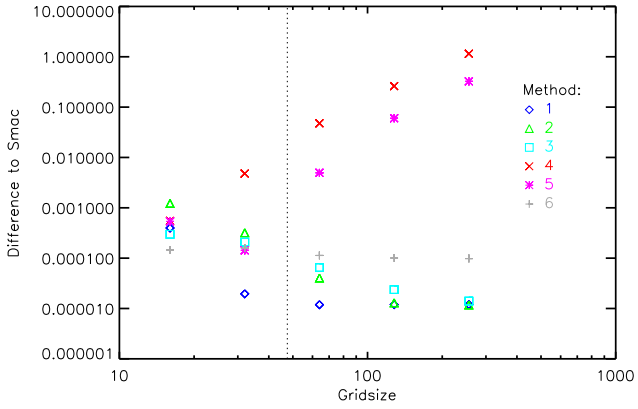

Figure 18: Difference to projected map for box size 500 kpc

5 Autocorrelation and power spectrum of the magnetic field

Now we can use the grid to compute the autocorrelation function and the power spectrum of the magnetic field. In this chapter I will first define autocorrelation function and power spectrum, then show how they are connected and last but not least show a couple of tests about power spectra from different resolutions, from grids that where computed by different methods and on boxes of different size.

The autocorrelation of a the magnetic field in a finite volume is given by the cross-correlation with itself.

$$A(\vec{d}) = B(-\vec{x}) \circ B(\vec{x}) = \frac{1}{V} \int_{-\infty}^{\infty} B(\vec{x}) B(\vec{x} - \vec{d}) d\vec{x} \tag{47}$$

In 3 dimensions it becomes a tensor.

$$M_{ij}(\vec{d}) = B_i(-\vec{x}) \circ B_j(\vec{x}) = \frac{1}{V} \int_{-\infty}^{\infty} B_i(\vec{x}) B_j(\vec{x} - \vec{d}) d\vec{x} \tag{48}$$

In the isotropic case this tensor can be reduced to the magnetic autocorrelation function.

$$w(\vec{r}) = M_{ii}(\vec{r}) = M_{ii}(r) \tag{49}$$

In this paper we define the n-dimensional Fourier transformation of a function $F(\vec{x})$ by

$$\tilde{F}(\vec{k}) = \int F(\vec{x}) e^{-i\vec{k}\vec{x}} \, d^n x \tag{50}$$

$$F(\vec{x}) = \frac{1}{(2\pi)^n} \int \tilde{F}(\vec{k}) e^{ikx} \, d^n k. \tag{51}$$

The magnetic power spectrum as the Fourier transformed magnetic autocorrelation function writes

$$\Phi_{ii}(\vec{k}) = w(\vec{k}) = \int_{-\infty}^{\infty} w(\vec{r}) e^{-i\vec{k}\vec{r}} d\vec{r}. \tag{52}$$

If we use isotropy again this equation can be simplified to

$$\begin{aligned}
w(k) &= \int_{-\infty}^{\infty} w(\vec{r}) e^{-i\vec{k}\vec{r}} d\vec{r} = \\
&= \int_0^{\infty} \int_0^{\pi} \int_0^{2\pi} w(r) e^{-ikrcos(\theta)} r^2 sin(\theta)\ dr d\theta d\phi = \\
&= 2\pi \int_0^{\infty} w(r) r^2 \int_0^{\pi} e^{-ikrcos(\theta)} sin(\theta)\ d\theta\ dr = \\
&\overset{z=cos(\theta)}{=} 2\pi \int_0^{\infty} w(r) r^2 \int_1^{-1} e^{-ikrz}(-1)\ dz\ dr = \\
&= 2\pi \int_0^{\infty} w(r) r^2 \frac{1}{-ikr} \left(e^{-ikr} - e^{ikr}\right) = \\
&= 4\pi \int_0^{\infty} w(r) r^2 \frac{sin(kr)}{kr}
\end{aligned}$$

Using the magnetic power spectrum we can get the one dimensional magnetic energy spectrum $\epsilon_B(k)$ by integrating over all angles in k-space.

$$\begin{aligned}
\epsilon_B(k) &= \frac{1}{8\pi} \int_0^{\pi} \int_0^{2\pi} w(k) k^2\ d\theta\ d\phi = \\
&= \frac{1}{2} w(k) k^2
\end{aligned}$$

By integration over k and multiplying with the volume of our box, we can get the magnetic energy contained in the box.

$$E = V \int_0^{\infty} \epsilon_B(k)\ dk \tag{53}$$

As it is very expensive to compute the autocorrelation function $\mathcal{O}(N^2)$ it is hard to achieve a reasonable resolution. Fortunately there is another way to calculate the power spectrum without calculating the autocorrelation function first.

$$\Phi_{ij}(\vec{k}) = \left(\int_{-\infty}^{\infty} B_i(\vec{x}) e^{-i\vec{k}\vec{x}} d\vec{x}\right) \left(\int_{-\infty}^{\infty} B_j(\vec{x}) e^{-i\vec{k}\vec{x}} d\vec{x}\right) = \tilde{B}_i(\vec{k}) \tilde{B}_j^*(\vec{k}) \tag{54}$$

The equality of both results for the power spectral density is shown by the Wiener-Khinchin theorem.

$$\int_{-\infty}^{\infty} M_{ij}(\vec{x}) e^{i\vec{k}\vec{x}} d\vec{x} = \frac{1}{V} \tilde{B}_i(\vec{k}) \tilde{B}_j^*(\vec{k}) \tag{55}$$

It can be proofed by a small calculation.

$$\begin{aligned}
\tilde{M}_{ij}(\vec{k}) &= \int_{-\infty}^{\infty} M_{ij}(\vec{r}) e^{-i\vec{k}\vec{r}} d\vec{r} = \\
&= \int_{-\infty}^{\infty} \frac{\int_{-\infty}^{\infty} B_i(\vec{x}) B_j(\vec{x}-\vec{r}) d\vec{x}}{V} e^{-i\vec{k}\vec{r}} d\vec{x} = \\
&= \frac{1}{V} \int_{-\infty}^{\infty} \int_{-\infty}^{\infty} B_i(\vec{x}) B_j(\vec{x}-\vec{r}) e^{-i\vec{k}\vec{r}} d\vec{x} d\vec{r} = \\
\overset{\vec{r}\to\vec{r}'+\vec{x}}{=} & \frac{1}{V} \int_{-\infty}^{\infty} \int_{-\infty}^{\infty} B_i(\vec{x}) B_j(\vec{r}') e^{-i\vec{k}\vec{r}'} e^{-i\vec{k}\vec{x}} d\vec{r}' d\vec{x} = \\
&= \frac{1}{V} \int_{-\infty}^{\infty} B_j(\vec{r}') e^{-i\vec{k}\vec{r}'} d\vec{r}' \int_{-\infty}^{\infty} B_i(\vec{x}) e^{-i\vec{k}\vec{x}} d\vec{x} = \\
&= \frac{1}{V} \tilde{B}_i(\vec{k}) \tilde{B}_j^*(\vec{k})
\end{aligned}$$

With equation 53 this also provides a way to get the autocorrelation function from two Fourier transformations via the power spectrum, that is much faster than the direct calculation.

5.1 Tests of the power spectrum

To see how the power spectrum will change if any parameter like method of grid calculation, box size, resolution etc. changes, I did some tests. The first test covers the calculation of the power spectrum from grids that were computed with different methods. As for the grid tests, again cluster g72 of the Hutt simulation was used. The size of the box was 2000 kpc with a resolution of 256^3 grid points.

The result is shown in figure 19. For scales larger than the maximum smoothing length all methods converge. This is clear due to the fact that the area of influence that one single particle has is for all methods not larger then a cube with a side length its smoothing length, like it is for method 6 (mod. TSC). For all other methods it is smaller. Once scales become smaller then the maximum smoothing length, methods 4 (Sort) and 5 (TSC) which neglect the smoothing length of the particles start to differ from the other methods. The other 4 methods show basically the same shape, while they vary a little. On scales lower than the average smoothing length the reliability of the power spectrum has to be questioned, as the SPH formalism is able to resolve these scales only on a small part of the box.

To conclude the method tests, methods 1, 2 and 3 give the best results and agree well with each other. As method 1 has much lower computational

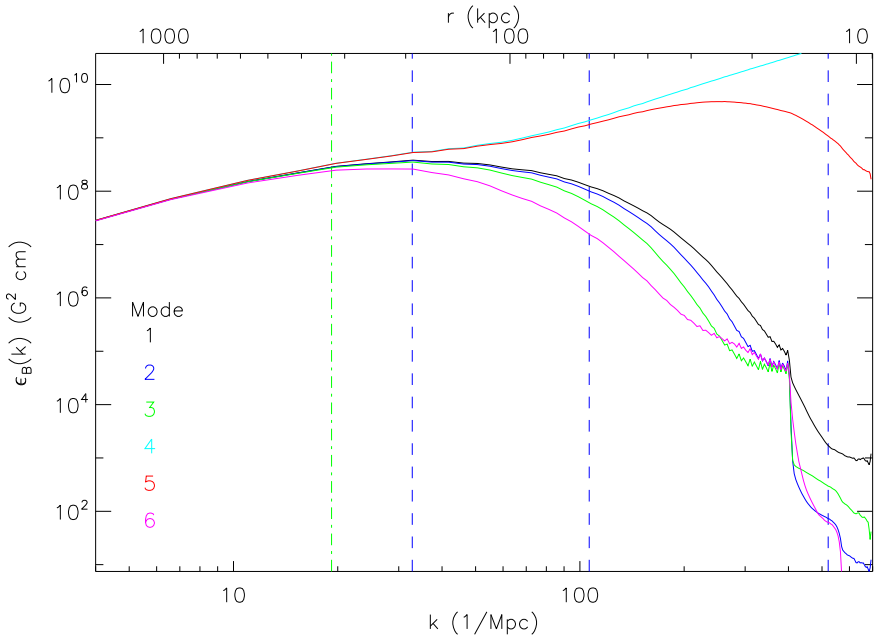

Figure 19: Magnetic power spectrum for different grid calculation methods. Full lines are power spectra of different methods. Vertical dashed lines show the maximum, average and minimum (from left to right) smoothing length of the particles within the box. It is arguable if scales smaller then the average smoothing length are resolved at all. The vertical dashed dotted line represents 10% of the virial radius of the cluster.

costs than method 2, and method 3 has the disadvantage that it additionally smoothes the quantities, **method 1 seems to be the best choice**. In the following calculations always method 1 (SPH) is used to calculate the grid.

Figure 20 shows power spectra calculated from a method 1 (SPH) grid for resolutions from 16^3 to 512^3 grid cells. Apparently for each resolution the power spectrum agrees with the better resolved power spectra on scales larger then approximately twice the size of the grid cells for this resolution. For a resolution of 256^3 grid cells the power spectrum is converged down to the scales much smaller then the average smoothing length. This is more than enough for this work, as it is converged in the whole area that is interesting, which starts at scales around the average smoothing length. The increasing curvature on small scales is due to SPH smoothing in less resolved parts of

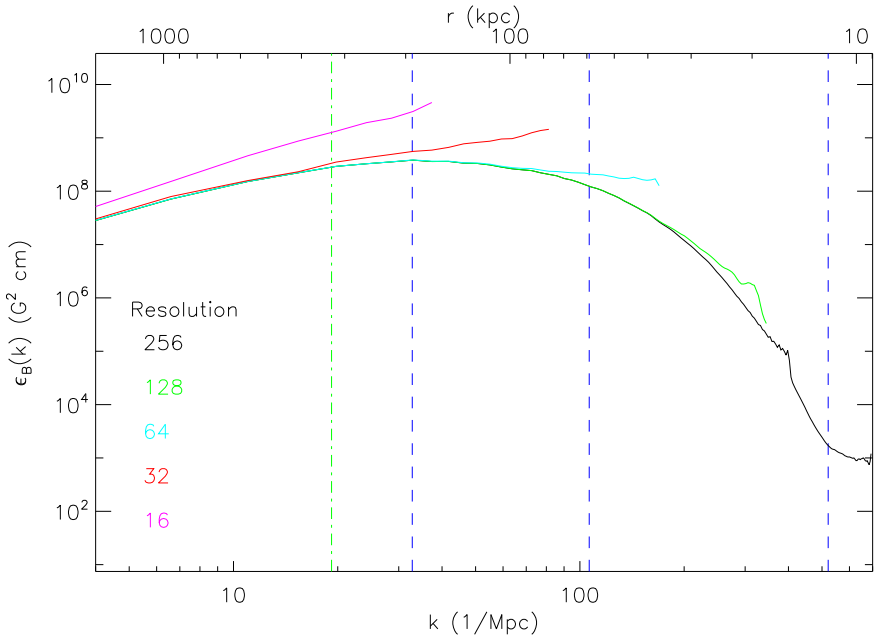

Figure 20: Magnetic energy spectrum for different resolutions. Box size is 2000 kpc. Full lines are power spectra of different resolutions. Vertical dashed lines show the maximum, average and minimum (from left to right) smoothing length of the particles within the box. It is arguable if scales smaller then the average smoothing length are resolved at all. The vertical dashed dotted line represents 10% of the virial radius of the cluster.

the box.

As one can see in figure 21, in this case the magnetic energy is mainly located not further away from the center of the cluster than a few hundred kpc. Therefore the total magnetic energy of boxes centered on the center of the cluster will not change significantly with the size of the box as long as the box is larger than about 1 Mpc. Thus to compare power spectra of different box sizes it is more reasonable to compare energy $E_B(k) = \epsilon_B(k) \cdot V$ than energy density. The radial distribution of the magnetic energy may however be different in other cases.

In figure 22 one can see power spectra with the same grid cell size for boxsizes and resolutions from 2000 kpc respectively 512^3 grid points to 62.5 kpc respectively 16^3 grid points. They have approximately the same shape

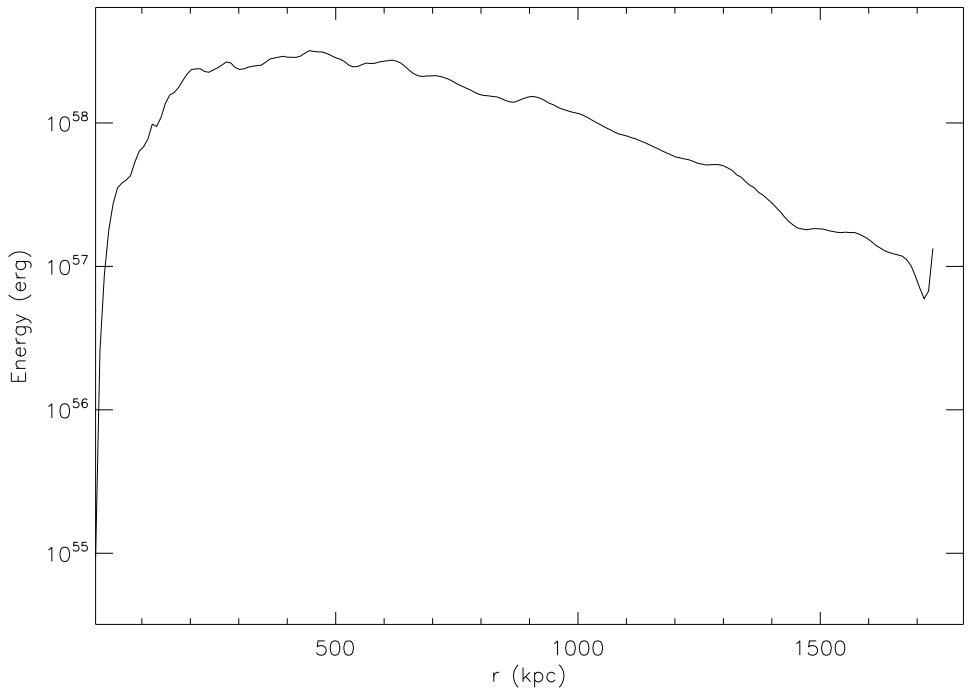

Figure 21: Magnetic energy of spherical shells around the cluster center with a size of 9kpc.

on the left hand side, but differ in the scale where the spectrum starts to decrease. This scale is smaller for smaller box sizes. It can be explained by the smaller maximum smoothing length of the smaller boxes. Therefore the grid is well resolved down to smaller scales. The absolute values of the power spectra is also smaller with smaller box sizes, as it is directly connected to the magnetic energy that depends on the volume of the box.

Figure 23 shows a modified version of figure 22. Here the lines are cutted at the average smoothing length of their box and 80% of the average smoothing length of the next larger box. To compensate for the smaller volume and therefore overall reduced energy, they are normalised to have the same mean value within overlapping ranges. This way the combined power spectrum is more reliable on lower scales, as the parts used there have a smaller box. Therefore they are less contaminated by numerical noise induced by low resolved areas in the outer part of the cluster than in the larger boxes. However

they suffer from the lower volume they are calculated on. One can see, that this combined power spectrum drops slowlier on small scales than the power spectra computed from the larger box. So it demonstrates that the steep drop of the power spectrum on small scales is due to the SPH smoothing. However it still does not show a clear power law. Note that the power spectra infered from the obersations by [MGF+04] reduced by a cluster-wide modelling of the magnetic field, and therefore constrain the magnetic field in a region of order of Mpc. So to compare them with our simulations a similar volume has to be investigated.

There are two aspects of the power spectrum that also have to be considered. Often zeropadding is used to compute the Fourier transformation. That means that one uses a grid twice as large as the data grid, that contains the original grid in the middle and is filled with zeros around. This should compensate for the function being non-periodic. To test the effects of zeropadding I additionally computed the power spectrum of my grid using this zeropadding method. It did not show any significant difference to the power spectrum computed without zeropadding. This may be explained by the fact that the magnetic field is already very small at the borders of the box, compared to the magnetic field in the center of the box. So the magnetic field has already its own zeropadding. Since it did not have any noticeable effect and needed eight times more memory, I did not use it further.

The other aspect is, that as the Fourier transformation is computed on a finite grid, this grid acts as a rectangular window function on the original quantity. To test the influence of this effect, I computed the power spectrum on larger grids with additional artificial window functions. Again, the window function did not have any significant effect, for the same reason as for the zeropadding method. Therefore the cut of the magnetic field at the border does not change anything.

5.2 Computing the autocorrelation function from a power spectrum

As we saw in equation 53, there is a way to get the autocorrelation function without computing it directly. Figure 24 shows the directly computed magnetic autocorrelation function and its counterpart, that was calculated from the magnetic power spectrum. While the directly computed autocorrelation function has only a resolution of 64^3 grid cells because of limited

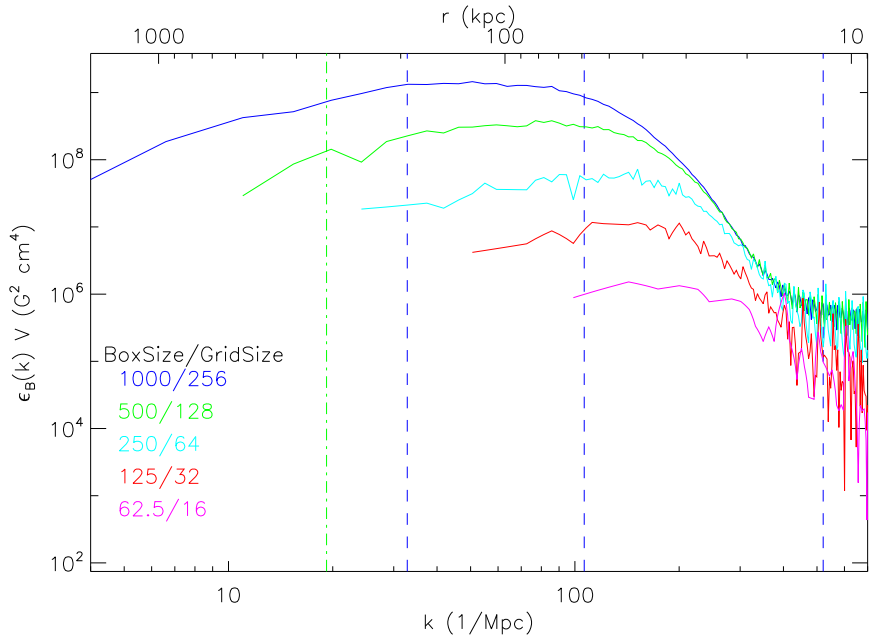

Figure 22: Magnetic energy for different box sizes and resolutions with the same grid cell size (box size / resolution = const). Full lines are power spectra for different box sizes and resolutions. Vertical dashed lines show the maximum, average and minimum (from left to right) smoothing length of the particles within the 2000 kpc box. It is arguable if scales smaller then the average smoothing length are resolved at all. The vertical dashed dotted line represents 10% of the virial radius of the cluster.

computational power, the power spectrum has a resolution of 256^3 grid cells and was done with much less effort. One can see, that the curve itself and especially height and position of the extrema of the autocorrelation function, that was computed from the power spectrum, agree well with the extrema of the directly computed function.

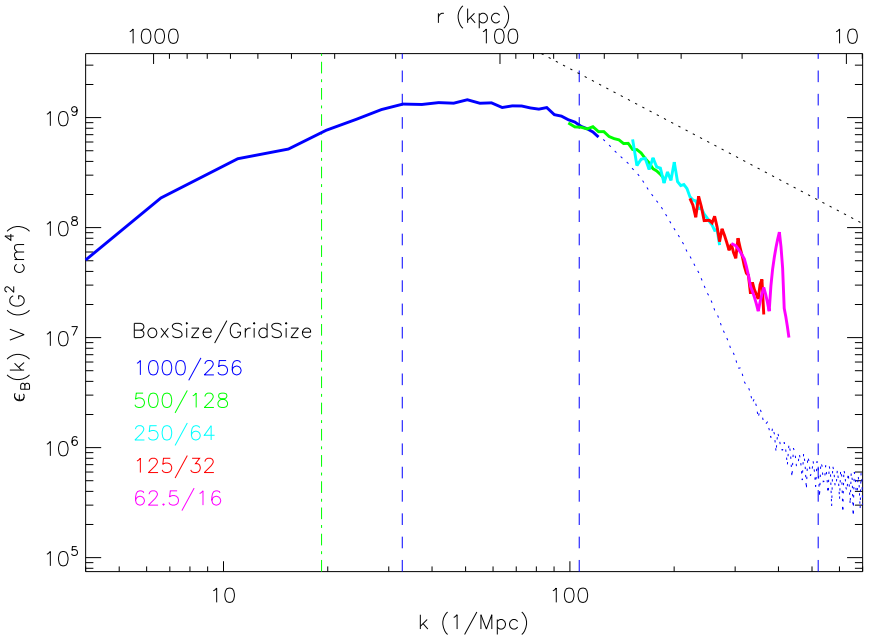

Figure 23: This figure is similar to figure 22. However all lines are cutted on large k at the average smoothing length of their box and at 80% of the average smoothing length of the next larger box at small k. They are normalised to have the same mean value over overlapping ranges. The dashed blue line is the continued powerspectrum of the largest box. The dashed black line shows the -5/3 power law of a Kolmogorov spectrum for comparison.

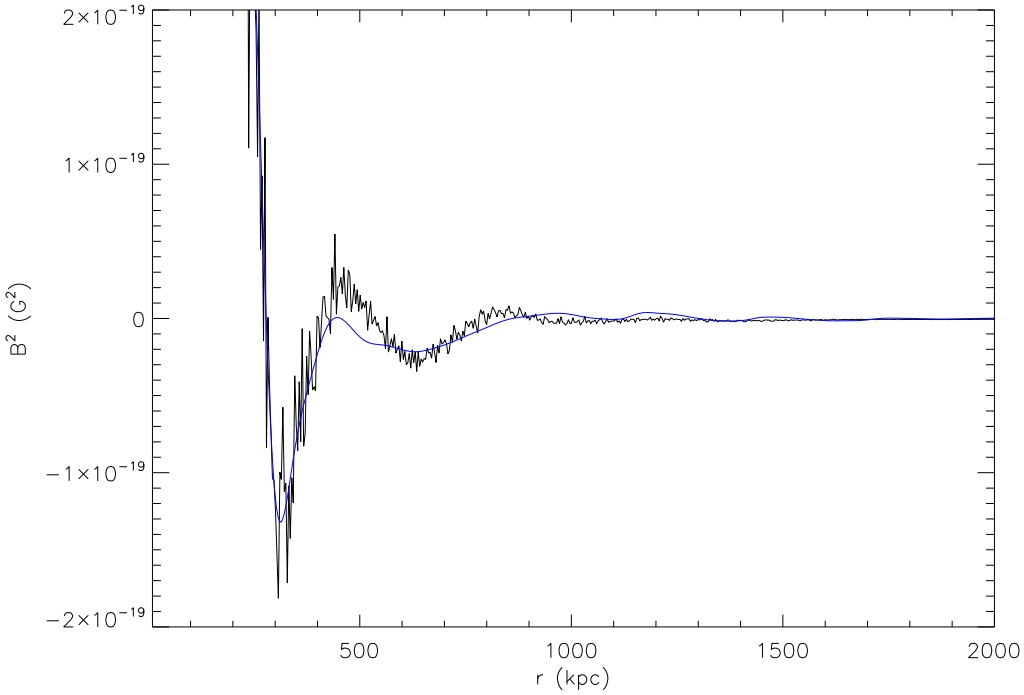

Figure 24: Autocorrelation function for a resolution of 64^3 grid cells (black) and autocorrelation function computed from power spectrum with a resolution of 256^3 grid cells (blue). Box size 2000 kpc.

6 The Hutt simulation

The Hutt simulation is a high resolution re-simulation of galaxy clusters taken from a large volume cosmological simulation. These simulations contain both dark matter and baryonic matter. Along with the baryonic matter also magnetic fields are included. Both follow the equations of ideal magnetohydrodynamics. (see section 3). The particles also carry information about shocks that diagnostic reasons, that were evaluated using a shock detection scheme developed by [PSEJ06].

It has already been shown that rotation measure maps generated from these simulations are able to reproduce observed RM maps of galaxy clusters well. (see [DBL99], [DBL02], [DGST05]).

From that simulation I chose 3 clusters for a detailed analysis. Their basic properties are shown in table 5. The g72 and the g51 cluster have approximately the same mass and radius. The g72 cluster has a two major mergers with a time difference of 3Gyears in between. After the second major merger, it continuously accretes further small halos. This avoids that the cluster is able to relax. The g51 cluster has only one major merger that is followed by 4.5Gyears of quiet growth and some smaller mergers afterwards. The g676 cluster is one order of magnitude less massive than the other two clusters and has only half of their radius. Like the g51 cluster it has one major merger, but its quiescent period after the merger is shorter than for the g51 cluster. So it undergoes many minor merging events before it has time to relax.

The detection of halos in cosmological simulations is not trivial. Here they are defined as spherical over densities around local maxima in the density field. The radius of an halo is then defined as the sphere around the center that has about 200 times the mean density of the simulation, and the mass within this sphere is the mass of the halo. The position of the center of the cluster is given by the gravitationally most bound particle, i.e. the particle that feels the deepest gravitational potential. It is then possible to reconstruct the evolution of this cluster from a small halo to a larger and larger object, by starting with a cluster at the end of the simulation and tracking this cluster backwards in time. The most massive progenitor of the cluster is then always associated with the galaxy cluster under investigation.

Table 5: Galaxy clusters of the Hutt simulation

Cluster	Mass in $M_\odot$	Dark matter mass in $M_\odot$	Baryonic mass in $M_\odot$
g72	$1.361 \cdot 10^{15}$	$1.208 \cdot 10^{15}$	$1.534 \cdot 10^{14}$
g51	$1.289 \cdot 10^{15}$	$1.144 \cdot 10^{15}$	$1.459 \cdot 10^{14}$
g676	$1.046 \cdot 10^{14}$	$9.202 \cdot 10^{13}$	$1.261 \cdot 10^{13}$

Cluster	Virial radius in kpc
g72	2291.25
g51	2248.36
g676	974.46

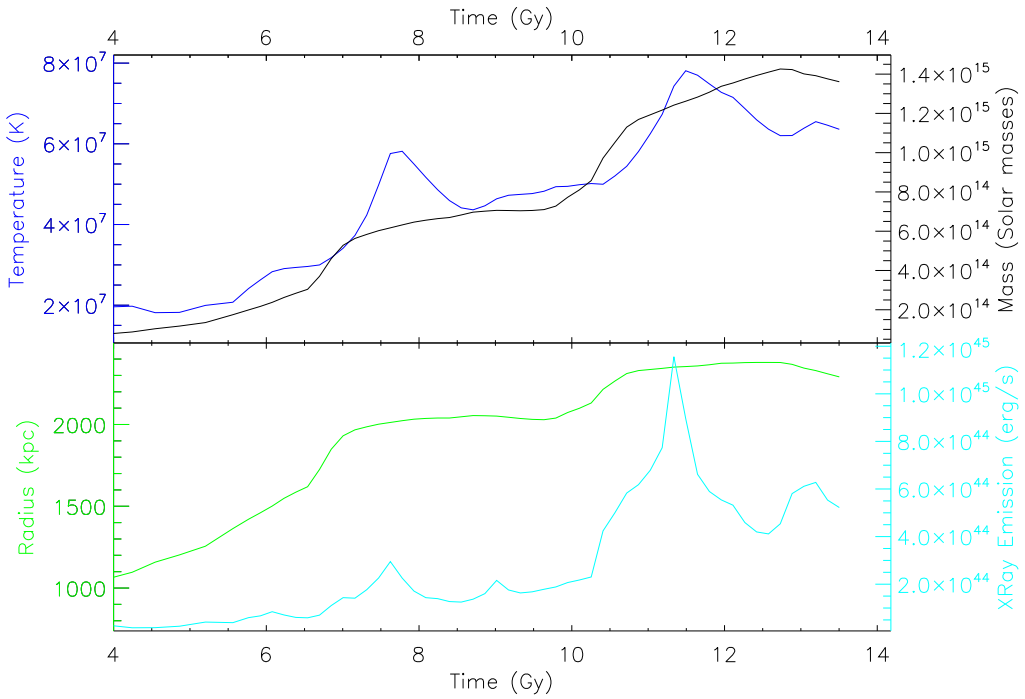

Figure 25: Time evolution of temperature, mass, radius and x-ray luminosity of cluster g72.

6.1 The g72 cluster

The g72 cluster is one of the two most massive clusters of the sample. Figure 25 shows 4 basic properties of the cluster, mass and temperature in the upper

plot, radius and total x-ray luminosity in the middle plot and the radius in the lower plot, all of them versus time in measured in the age of the universe. The cluster mass is given by the sum of the mass of all particles within the virial radius of the cluster.

The temperature of the cluster is given by the average temperature of all SPH particles within the cluster radius. The x-ray luminosity of the cluster is calculated by the formula given in equation 16, with an upper bound of the emitted energy of 2.4 keV and a lower bound of 0.1 keV.

From figure 25 we can already see the dynamical history of the cluster. First of all, the mass of the cluster is steadily increasing with time. Additionally there are 2 events at about 6.7 Gyears and 10.3 Gyears where a rapid increase of the mass occurs. This rapid increase is in both cases due to a merger with another big halo. Indeed this is the expectation within the hierarchical structure formation scenario. While they are accreting matter, once in a while some more massive structures are merging. Therefore mergers with similar massive structures are not uncommon at all.

The temperature of the cluster is also increasing with time, since its mass is increasing and therefore with the gravitational potential becoming deeper, the gas in the cluster is heated up. The temperature has two peaks respectively, that have their maximum about 1 Gyear after a merger. The temperature peaks can be understood considering that mergers induce shocks into the gas, which efficiently heat the gas (see [SM93]). About 2 Gyears after the shock, the gas has relaxed again and the temperature has returned to a value that is expected from the mass of the cluster.

The x-ray luminosity of the cluster stays nearly constant, except for some fluctuations and two peaks at both major mergers. It rises with the beginning of the merger, at the same time as the temperature, and has also its maximum at the same time (see also [SM93]). In contrast to the temperature it falls down faster and stays slightly enhanced even 2 Gyears after the merger. Also it increases slightly with time.

In general, a merging halo can have a second pass through the cluster center if it still exists after the first pass. In this case there will be a smaller peak around 2 Gyears after the first one in the temperature and x-ray luminosity, without any signature of previous mass increase. This can be seen for g72 at around 9 Gyears and 13 Gyears.

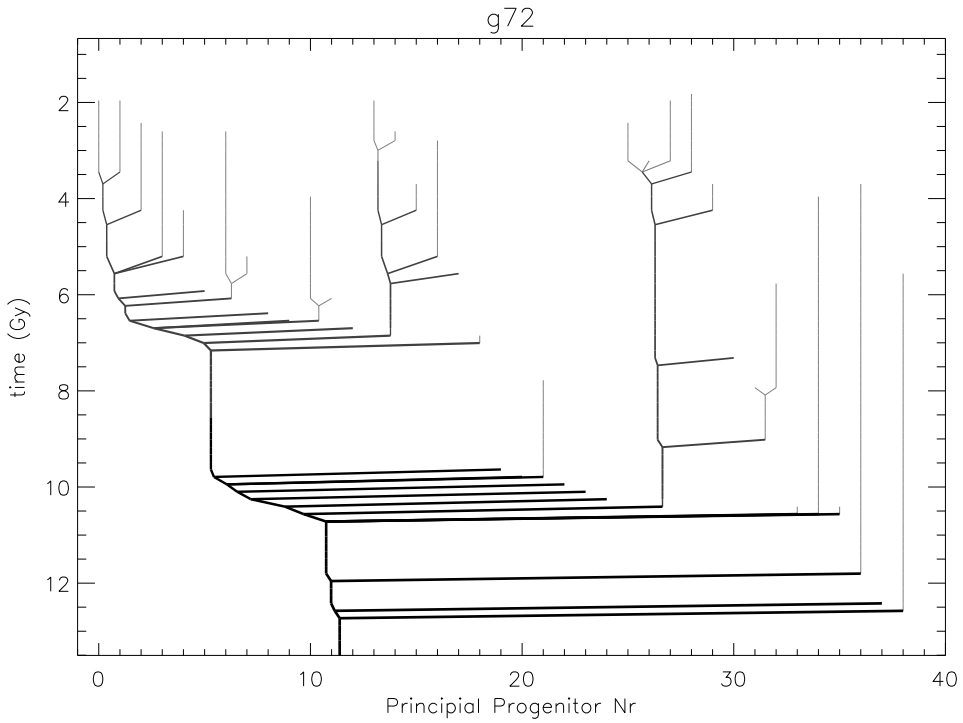

Figure 26: Merger tree of the g72 cluster. The darker and bigger the line is, the more massive is the cluster.

6.1.1 Merger history

Structure formation starts on small scales, that are able to collapse. This means that small halos form first. With time they grow by accreting matter of their neighbourhood and merging with other halos to create a larger halos. So the largest objects, that are galaxy clusters today, are the objects that formed latest. As a galaxy cluster is the result of many mergers of small halos while forming, it has a substructure that depends on this merger history. Therefore it is of interest to study the merger history of simulated clusters, as it is responsible for the morphology of the cluster.

To illustrate the merger history of a cluster, often merger trees are used. Figure 26 shows the merger tree for the g72 cluster. It shows the evolution of the cluster over time. Each vertical line represents a halo, out of them the most left branch represents the g72 cluster. For clarity reasons we show

only halos with more than 5000 particles. Horizontal lines that connect two vertical lines to a new line stand for a merger between the two halos into a new one. The position of the cluster on the x-axis is given by the weighted average of the masses of the halos that merged in the previous timestep. With increasing mass of the halos, their line becomes darker and thicker.

Figure 26 shows two larger mergers, that appear as consecutive row of a whole bunch of smaller mergers. One starting at 6.7 with a mass ratio of 7:5 between the two halos and another at 10.3 Gyears with a mass ratio of 2:1. Although they seem to be a row successive mergers with different halos, these two mergers are in fact only time elongated mergers with one other big halo. The spread occurs due to the way the virial radius of the larger of both merging halos is evaluated. While the two halos move into each other, more and more subclusters that were originally part of the less massive cluster are counted as parts of the more massive cluster, until the merger halo has been completely absorbed. Additionally, massive halos live in overdense regions and therefore are often surrounded by smaller halos which then also merge into the cluster.

6.1.2 Energies

In galaxy clusters there is energy in different forms, namely the gravitational potential of the dark matter halo, the kinetic energy of the gas, the inner energy of the gas and the magnetic energy in the magnetic fields of the cluster. The gravitational potential is mainly the potential of the dark matter, as it collapses faster since it does not have any pressure that is able to stabilise against the collapse. When gas falls into the gravitational potential of the dark matter halo, its kinetic energy increases. The pressure of the gas then leads to accretion shocks around the cluster heating the gas. Also smaller substructures that move with supersonic speed inside the cluster drive shocks through the gas. Therefore the gas additionally is heated. If one assumes equilibrium, the temperature of the gas refers to the depth of the gravitational potential. The magnetic energy is not directly connected to kinetic and inner energy, however the amplification of the magnetic field is caused by adiabatic compression when the magnetised plasma falls into the potential and shear flows within the gas, created by motions on small scales.

The energies are calculated from the simulation on a grid. Of them the inner energy of the gas is the easiest to compute, as it is a direct property

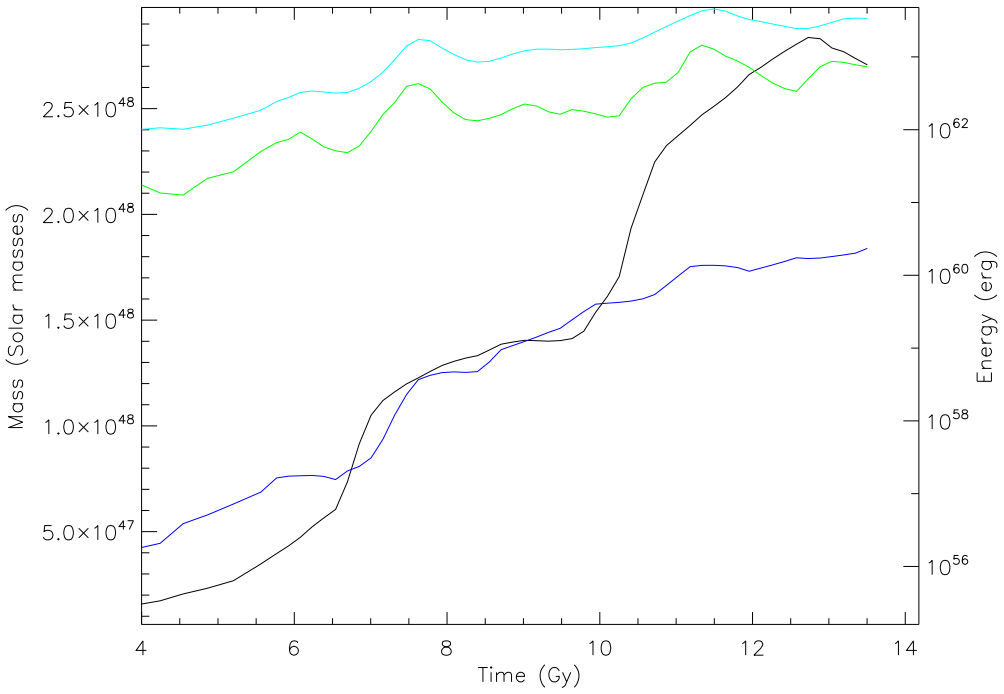

Figure 27: Time evolution of total kinetic energy (green), inner energy (cyan) and magnetic energy (blue) in a 2Mpc box centered at the center of the g72 cluster with a resolution of 256^3 grid points. The magnetic energy was smoothed using 2 steps in the future and to steps in the past. For comparison also the mass (black) of the cluster is plotted.

of the gas particles. So one has only to compute the grid and sum over all cells. The kinetic energy is a bit harder to calculate. It depends on mass and velocity of the cells.

$$E_{Kin} = \sum_{Cells} \frac{1}{2} m_{Cell} \vec{v}_{Cell}^2 \tag{56}$$

But as the cluster as a whole is moving, it is necessary to substract the velocity of the cluster itself from the local velocities of the particles in the cluster to get the "real" kinetic energy of the cluster particles.

$$v_{Cell,local} = v_{Cell} - v_{Cluster} \tag{57}$$

This way it is possible to calculate the kinetic energy on scales larger than the minimum resolution of grid. As the grid is fine enough to reach the maximum resolution of the simulations, due to the simulations being adaptive, in less

resolved regions of the simulation an oversampling is created. This could in presence of numerical noise in principle contribute to the kinetic energy also on relatively large scales. However, we never saw any indications of such contributions.

The magnetic energy is given by

$$E_B = \sum_{Cells} \frac{1}{8\pi} \vec{B}^2_{Cell} \, V_{Cell}. \tag{58}$$

This equation also only holds if the magnetic field is constant inside a cell. In the same way as for the velocity, also for the magnetic field the resolution used is high enough that is reasonable to assume this.

Figure 27 shows kinetic energy, inner energy and magnetic energy of the g72 cluster. For comparison also the mass is shown. All energies are calculated on a 2Mpc grid with a resolution of 256^3 grid cells by summation over all cells. Inner energy is about one order of magnitude larger than the kinetic energy. Both increase with time. After the mergers both show a peak. The peaks in the kinetic energy have a width of about 1Gyear, the peaks in the inner energy are slightly broader. The increase in the inner energy is mainly due to shocks that were created by the merger that run through the gas, heating it and therefore increasing its temperature and inner energy. Also its inner energy stays on a higher level after the merger than it had before, reflecting the increased deepness of the potential well due to the merger.

As both merging clusters are not homogeneous and hence have an inhomogeneous gravitational potential, they create large tidal forces on the particles. This effect increases the peculiar velocities of the particles. Also the clusters create large forces by attracting the other cluster with their gravitational potential, leading to a general acceleration of both clusters towards each other. Both effects lead to an increase of the kinetic energy within the cluster. Indeed the kinetic energy decreases after about 1 Gyear back to the value it had before the merger. This can be explained stating that viscosity leads to a relaxation of the cluster, as there is no energy source to maintain their higher velocity.

The magnetic energy of the cluster is a few orders of magnitude smaller then inner and kinetic energy. However it grows by 3 orders of magnitude during the simulation. Additionally to a steady growth with time, it is abruptly increased by about a factor of 10 after the first merger, nearly simultaneously

with the peaks in inner and kinetic energy. After the first merger the total magnetic energy evolves rather mild. This has its reason in the fact, that is as more difficult to amplify a magnetic field, as larger it already is. This can be seen as a saturation effect, as already mentioned in previous studies. These studies also showed that the structure of the magnetic field within the cluster does not depend on the form of the magnetic seed field. We will see, that this is a result of the first major merger of a cluster, that reshapes its entire magnetic field.

6.1.3 Kinetic Energy

It is also interesting to have a more detailed look at the energy distribution. One point is the distribution of the energy on different scales. As the kinetic energy depends on mass density and velocity, it is coupled to the form of the velocity field. In particular how large areas are, where the velocity points towards the same direction and on which scales the velocity fields is ordered. To obtain the kinetic energy on different scales I calculated the local mean velocity on these scales. This is done by segmenting the whole grid into cubes with given length. For these cubes I calculated the mass weighted average velocity of all cells of each cube.

$$\vec{v}_{Cube} = \frac{\sum\limits_{Cells} m_{Cell} \cdot \vec{v}_{Cell}}{\sum\limits_{Cells} m_{Cell}} \tag{59}$$

Reducing the velocity of the cells by the velocity of their cube, which is the mean velocity on the given scale, only the small scale velocity field is left. So the kinetic energy inside the grid on scales smaller then the size of the averaged cubes can be evaluated as

$$E_{Kin} = \sum_{Cells} \frac{1}{2} m_{Cell} (\vec{v}_{Cell} - \vec{v}_{Cube})^2. \tag{60}$$

If one chooses the size of the cluster as maximum scale, than this equation will be equal to equation 56, that describes the kinetic energy of the whole grid without the kinetic energy of the overall motion of the cluster. To get the kinetic energy around a given scale, I subtracted the energy of all scales smaller than the next lower scale (that is half of this scale) from this energy.

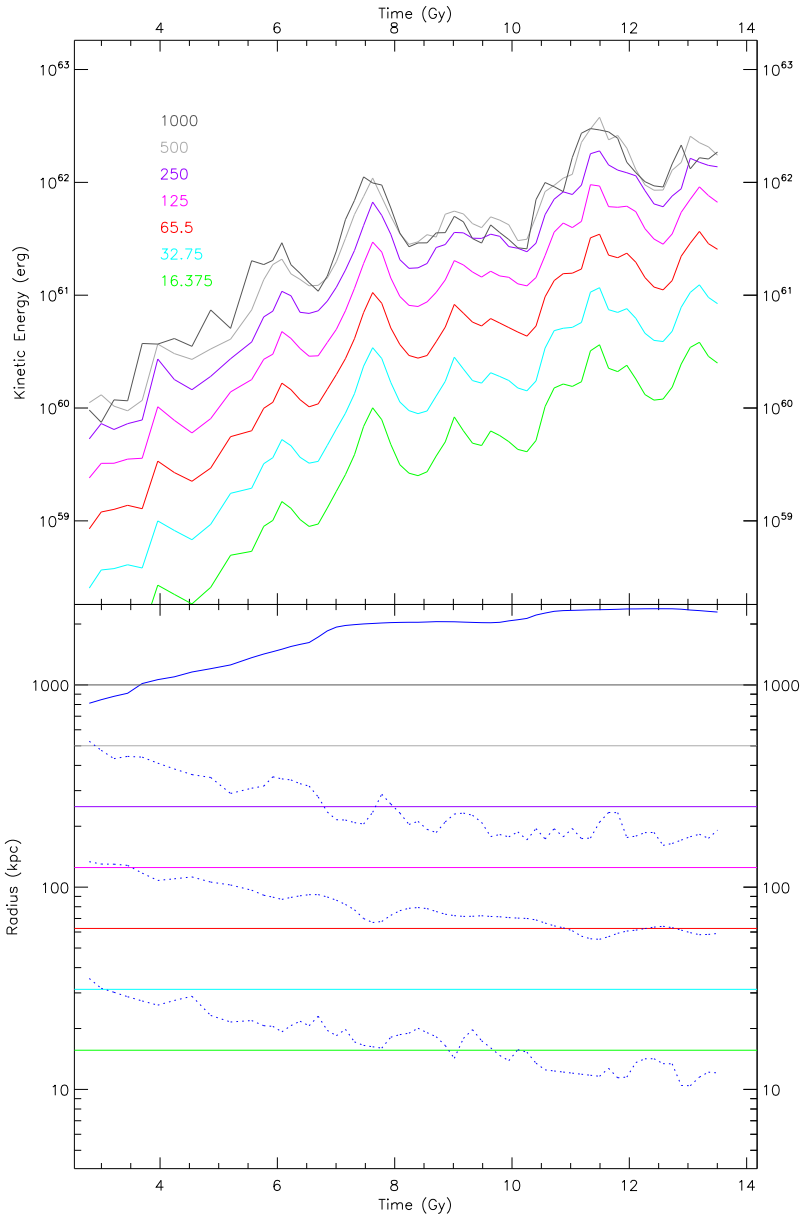

Figure 28: Time dependent kinetic energy on different scales in a 2Mpc box centered on the g72 cluster with a resolution of 256^3 grid points. Colored lines in the upper plot show the kinetic energy on scales between their scale and the next smaller scale. The scales are given by averaging over a number of grid cells, that is written in the lower left corner. So the green line shows the kinetic energy on the smallest scales, while the black line shows it on the largest scales. Colored lines in the lower plot (except the blue lines) show the distance that was averaged over for the kinetic energy line of the same color. The blue line shows the virial radius of the cluster. Dashed blue lines (from the highest to the lowest line) stand for the maximum, average and minimum smoothing length of the particles within the given box.

Figure 28 shows the kinetic energy of the g72 clusters on different scales. The upper plot shows the evolution of the kinetic energy with time. One can see, that most kinetic energy is on large scales (> 100 kpc) and that is in general as larger the scale is we look at, as higher is its kinetic energy. So the particle velocities are mainly due to large scale motions. Also the evolution of the kinetic energy on scales smaller than 100 kpc (all lines below purple), is nearly identical for all scales. Both peaks in the total kinetic energy that are caused by the mergers exist on all scales. There is no significant transfer of kinetic energy between different scales. This means that these simulations show no evidence of a significant turbulent cascade. As already shown in previous works, this can be understood mentioning that the velocity field of the cluster is dominated by the imprint of the cosmological velocity field that originates from the formation and growth of structures. Therefore local instabilities that would be associated with hydrodynamic turbulence do not have any visible influence. Another explanation is the rather high artificial viscosity of the SPH formalism, that is needed to capture shocks properly, but tends to suppress turbulence.

The lower plot shows the size of the different scales used in the upper plot in comparison with the virial radius of the cluster and the minimum, average and maximum smoothing length of particles within the grid box. The comparison with these smoothing lengths is interesting, as they tell something about the resolution of the simulation. Scales that are larger then the maximum smoothing length are completely resolved (that fits for the 700kpc, 350kpc and 175kpc averaging distances). Scales that are between the minimum and the maximum smoothing length are well resolved only in regions where particles have smaller smoothing lengths, i.e. towards high densities at the center of the cluster. Far away from the center of the cluster, these scales are not resolved any more, as the smoothing length of the particles are larger than these scales. The results for the kinetic energy on these scales that are smaller then the maximum smoothing length can only be trusted, as long as the kinetic energy there is dominated by regions whose resolution is better than this scale. This may possibly hold for the scales that are smaller than the maximum smoothing length, but larger than the average smoothing length. However the fact that the kinetic energy for the different scales smaller than the maximum smoothing length seems to behave similar indicates that these scales are not resolved enough and the results for the kinetic energy on these scales are significantly influenced by numerical effects.

6.1.4 Magnetic Energy

For the magnetic energy I did the same analysis. I split the grid into cubes and calculated the average magnetic field of a cube by

$$\vec{B}_{Cube} = \frac{\sum\limits_{Cells} \vec{B}_{Cell}}{\#\ Cells}. \tag{61}$$

This average magnetic field I subtracted from the magnetic field of each cell.

$$\vec{B}_{Cell,local} = \vec{B}_{Cell} - \vec{B}_{Cube} \tag{62}$$

Then I summed up the magnetic energies of all cells using their local magnetic field to get the magnetic energy for all scales smaller than a given averaging scale.

$$E_{B,small} = \sum_{Cells} \frac{1}{8\pi} \vec{B}^2_{Cell,local} \cdot V_{Cell} \tag{63}$$

This definition is equivalent to say that the magnetic energy on scales larger than a given scales is

$$E_{B,large} = \sum_{Cubes} \frac{1}{8\pi} \vec{B}^2_{Cube} \cdot V_{Cube}. \tag{64}$$

If this definition makes sense than the sum of the energy on scales smaller than a given length and the energy on scales larger than this length should be the same as the total magnetic energy. To test this, we assume that we split our grid into cubes of M^3 cells. It is sufficient to show that the energy sum is correct on one cube. In this case it also holds for the energies of the sum of the cubes, as the total energies are also just the sum of the energies of all cubes. On one cube the energies are the following.

$$\begin{aligned}
E_{B,small} &= \sum_{j=1}^{M^3} \frac{1}{8\pi} V_{Cell} \cdot (\vec{B}_{Cell,j} - \vec{B}_{Cube})^2 = \\
&= \sum_{j=1}^{M^3} \frac{1}{8\pi} V_{Cell} \cdot \left(\vec{B}_{Cell,j} - \sum_{i=1}^{M^3} \frac{\vec{B}_{Cell,i}}{M^3} \right)^2 \\
E_{B,large} &= \frac{1}{8\pi} \vec{B}^2_{Cube} \cdot V_{Cube} = \\
&= \frac{1}{8\pi} M^3 \cdot V_{Cell} \left(\sum_{i=1}^{M^3} \frac{\vec{B}_{Cell,i}}{M^3} \right)^2 \\
E_{B,total} &= \frac{1}{8\pi} V_{Cell} \sum_{i=1}^{M^3} \left(\vec{B}_{Cell,i} \right)^2
\end{aligned}$$

So the sum of the energy on small and on large scales is

$$
\begin{aligned}
E_{B,sum} &= E_{B,small} + E_{B,large} = \\
&= \sum_{j=1}^{M^3} \frac{1}{8\pi} V_{Cell} \cdot \left(\vec{B}_{Cell,j} - \sum_{i=1}^{M^3} \frac{\vec{B}_{Cell,i}}{M^3} \right)^2 + \frac{1}{8\pi} M^3 \cdot V_{Cell} \left(\sum_{i=1}^{M^3} \frac{\vec{B}_{Cell,i}}{M^3} \right)^2 = \\
&= \frac{1}{8\pi} V_{Cell} \left[\sum_{j=1}^{M^3} \left(\vec{B}_{Cell,j} - \sum_{i=1}^{M^3} \frac{\vec{B}_{Cell,i}}{M^3} \right)^2 + M^3 \left(\sum_{i=1}^{M^3} \frac{\vec{B}_{Cell,i}}{M^3} \right)^2 \right] = \\
&= \frac{1}{8\pi} V_{Cell} \left[\sum_{j=1}^{M^3} \left(\vec{B}_{Cell,j}^2 - 2\vec{B}_{Cell,j} \sum_{i=1}^{M^3} \frac{\vec{B}_{Cell,i}}{M^3} + \left(\sum_{i=1}^{M^3} \frac{\vec{B}_{Cell,i}}{M^3} \right)^2 \right) + \right. \\
&\quad \left. + M^3 \left(\sum_{i=1}^{M^3} \frac{\vec{B}_{Cell,i}}{M^3} \right)^2 \right] = \\
&= \frac{1}{8\pi} V_{Cell} \left[\sum_{j=1}^{M^3} \vec{B}_{Cell,j}^2 - 2M^3 \sum_{j=1}^{M^3} \frac{\vec{B}_{Cell,j}}{M^3} \sum_{i=1}^{M^3} \frac{\vec{B}_{Cell,i}}{M^3} + \right. \\
&\quad \left. + M^3 \left(\sum_{i=1}^{M^3} \frac{\vec{B}_{Cell,i}}{M^3} \right)^2 + M^3 \left(\sum_{i=1}^{M^3} \frac{\vec{B}_{Cell,i}}{M^3} \right)^2 \right] = \\
&= \frac{1}{8\pi} V_{Cell} \sum_{j=1}^{M^3} \vec{B}_{Cell,j}^2 = \\
&= E_{B,total}
\end{aligned}
$$

Therefore this splitting of the magnetic energy into energies on larger and smaller scales than a given scales is reasonable. A similar calculation can be done for the kinetic energy, but it is more complex as the for the kinetic energy not only the velocity but also the mass of the grid cells has to be taken into account.

The magnetic energy rises by amplification of the magnetic field. There are basically two different ways how the magnetic field is amplified. On the one hand, a magnetic field that is frozen into a plasma is amplified when the plasma is compressed spherical and adiabatically. In this case the magnetic field strength scales with the density of the plasma $B \propto \rho^{2/3}$. On the other hand the magnetic field can be amplified be shearing flows in the plasma. However this way of amplification is only efficient for low magnetic fields and therefore looses its influence on the magnetic field with the growth of the magnetic field.

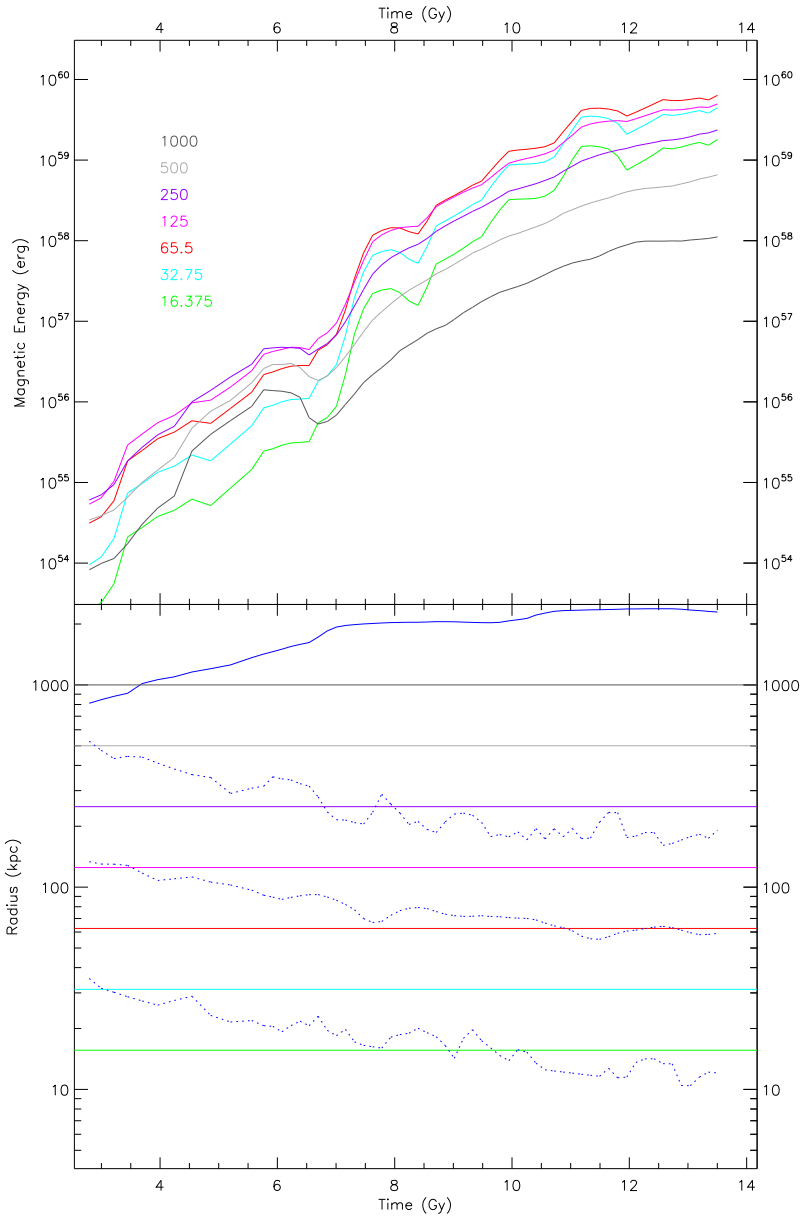

Figure 29: Time dependent magnetic energy on different scales in a 2Mpc box centered on the g72 cluster with a resolution of 256^3 grid points. The magnetic energy was smoothed using 2 steps in the future and to steps in the past. Colored lines show the magnetic energy on scales between their scale and the next smaller scale. The scales are given by averaging over a number of grid cells, that is written in the lower left corner. So the green line shows the magnetic energy on the smallest scales, while the black line shows the largest scales. Colored lines in the lower plot (except the blue lines) show the distance that was averaged over for the magnetic energy line of the same color. The blue line shows the virial radius of the cluster. Dashed blue lines (from the highest to the lowest line) stand for the maximum, average and minimum smoothing length of the particles within the given box.

The magnetic energy for different length scales is plotted in figure 29. The first difference to the kinetic energy one sees is that the main part of the magnetic energy is not on the largest scales, but on small scales. Also the order of the different scales sorted by their energy changes. So with time smaller scales grow more then larger scales (i.e. pink and red line are at the same level than the purple line at the beginning, but at a higher level in the end).

The first major merger of the cluster has a much larger effect on small than on large scales, however it increases the magnetic energy on all scales. The second major merger of the g72 cluster is not visible in the evolution of of any scales of the magnetic energy. After about 12 Gyears, the magnetic energy on large scales seem to be saturated and does not continue to grow.

The second plot of figure 29 is in fact the same as the second plot of figure 28. It shows the scales I had a look at in comparison to the maximum, average and minimum smoothing length of the particles within my cube. Again, the results on a scale are only useful, if they are at least dominated by regions that have a smaller smoothing length than this scale, i.e. they are well resolved.

Comparing the distribution of kinetic and magnetic energy in the cluster, the velocity seems to be driven by large scales, whereas the magnetic field is driven by small velocity gradients. This is consistent with the picture that shear flows drive the local amplification of the magnetic field. It also shows that the adaptive nature of the SPH formalism seems not to be so much restrictive for the magnetic field.

Another way to characterise the magnetic energy is to have a look at its local distribution. Most properties of the cluster like mass density, temperature, etc. are assumed to depend only on their distance to the cluster center in a first order approximation. So it is interesting to have look also on the radial distribution of the magnetic energy. Therefore I calculated the magnetic energy in spherical shells around the cluster center having a width of 9kpc. This is given by

$$E_{B,r} = \int_r^{r+\Delta r} \int_0^{\pi} \int_0^{2\pi} \frac{1}{8\pi} \vec{B}^2(r,\theta,\phi) r^2 sin(\theta)\ \mathrm{d}r\ \mathrm{d}\theta\ \mathrm{d}\phi. \qquad (65)$$

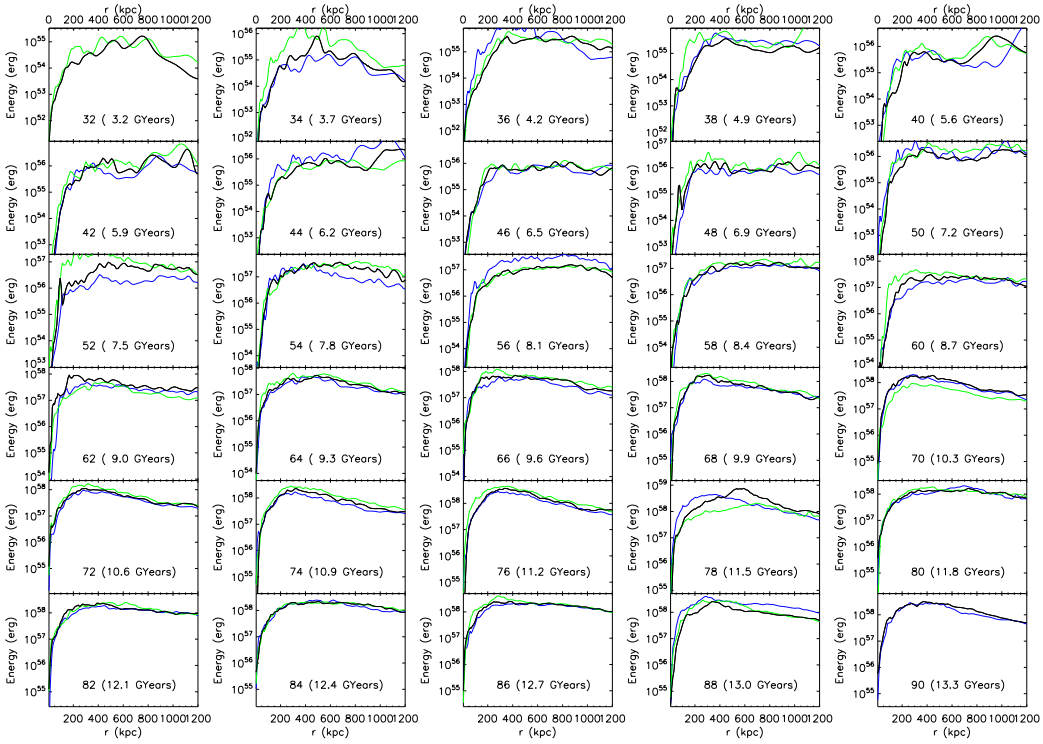

Figure 30: Radial magnetic energy of cluster g72 for every second snapshot for the current snapshot (black), the last snapshot (blue) and the next snapshot (green). So the blue curve is always equal to the green curve of the last plot.

As the magnetic energy is given by the product of the square of the magnetic field and the volume, it is constant for the shells if the square of the magnetic field decreases with r^{-3}, as the volume of the spherical shells increase with r^3. The total magnetic energy inside a sphere is then given by the sum of the energies of all shells within this sphere.

$$E_{B,total}(R) = \sum_{r<R} E_{B,r} \tag{66}$$

The radial magnetic energy for every second snapshot from 3.3Gyears to 13.3Gyears is plotted in figure 30. In the earliest snapshots, the magnetic energy rises with the radius for radii smaller than 500kpc, has a maximum between 500kpc and 800kpc and decreases for larger radii. One Gyear later the magnetic energy is nearly flat for radii larger than 250kpc. This distribution persists for a long time (about 5Gyears) until the magnetic energy

at large distances from the cluster center starts to decrease relatively to the energy at small radii. For a short time around 12 Gyears in the late times of the second merger it is nearly flat again, but the decrease of magnetic energy on large radii starts anew soon.

Both major mergers effect the radial distribution of the magnetic energy. However this happens not exactly during the merger, but when the temperature of the cluster reaches its maximum in consequence of the merger. The first merger mainly affects the magnetic energy at the center of the cluster after 7.5Gyears (plot snapshot 52). It first rises the energy for radii between 100 and 600 kpc, at lower radii by up to one magnitude. Only a short time later the energy also at large radii rises and the distribution is flat again. The second merger also effects the radial distribution of the magnetic energy at the maximum of the temperature around 11.3 Gyears (plot snapshot 78). It first redistributes magnetic energy from smaller radii (maximum of the energy is at 300kpc for snap 77, blue curve) to larger radii (maximum at 550kpc for snap 78, black curve). Then to the next snapshot the energy on radii smaller than about 700kpc decreases, leaving an again flat distribution.

That both mergers change the magnetic energy in the center of the cluster first with the peak in the cluster temperature is easily explained, as the temperature peak corresponds to the time when the merging halo arrives in the center of the cluster.

Figure 31 shows the line of sight integrated x-ray luminosity of the g72 cluster. One can see how hot halos fall into the cluster center during mergers. When the halo of the first merger has reached the center of the cluster (snapshot 52 for the first and snapshot 78 for the second merger) the temperature reaches its maximum.

6.1.5 Magnetic autocorrelation function

The magnetic autocorrelation function contains information about the structure of the magnetic field itself. A minimum in the autocorrelation function at a certain distance means that for this distance the magnetic field is preferably oriented in opposite directions. Therefore it characterises a typical lengthscale on which the magnetic field is basically ordered. The deeper the minimum is, the more important is this distance for the structure of the magnetic field.

Figure 32 shows in the upper plot the minima of the autocorrelation function for different times. At a distance of about 1400 kpc there is a persistent minimum that exists nearly all the time. It is most likely a part of the initial magnetic field of the simulation, that has been destroyed inside

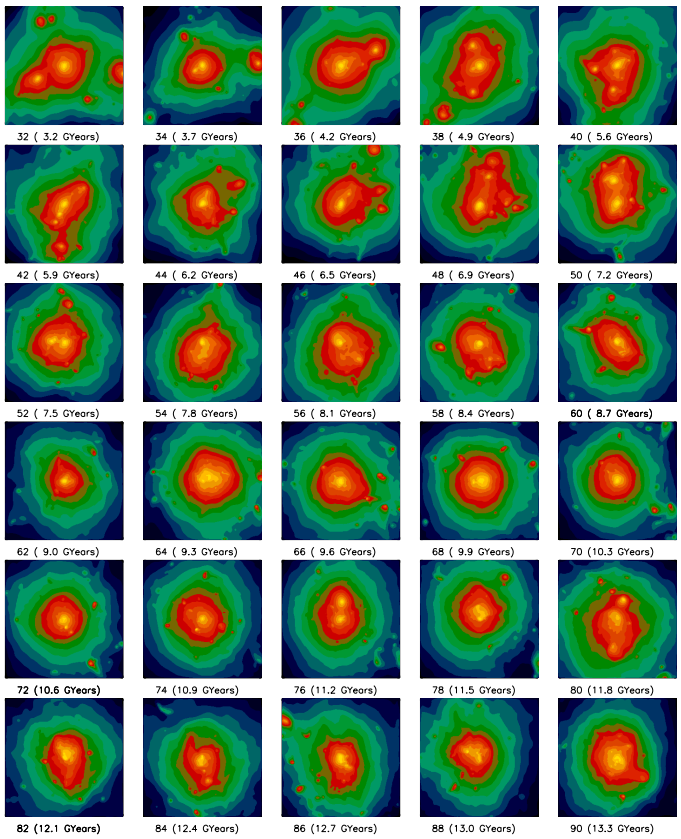

Figure 31: X-ray luminosity map of every second snapshot between 32 and 90 of the g72 cluster. The luminosity increases from blue via green and red to yellow where it is maximal.

the cluster but is still present in outer regions. To try if it is a residuum of the box size, I calculated the autocorrelation functions and their minima also for a larger 8000kpc box and found the same minimum about 1400 kpc.

Additionally there are a large number of minima that occur for some time and vanish afterwards. This may be any types of effects of structure formation like smaller mergers or smaller clumps moving with a large speed through the cluster, etc. They cause features on specific scales in the magnetic field,

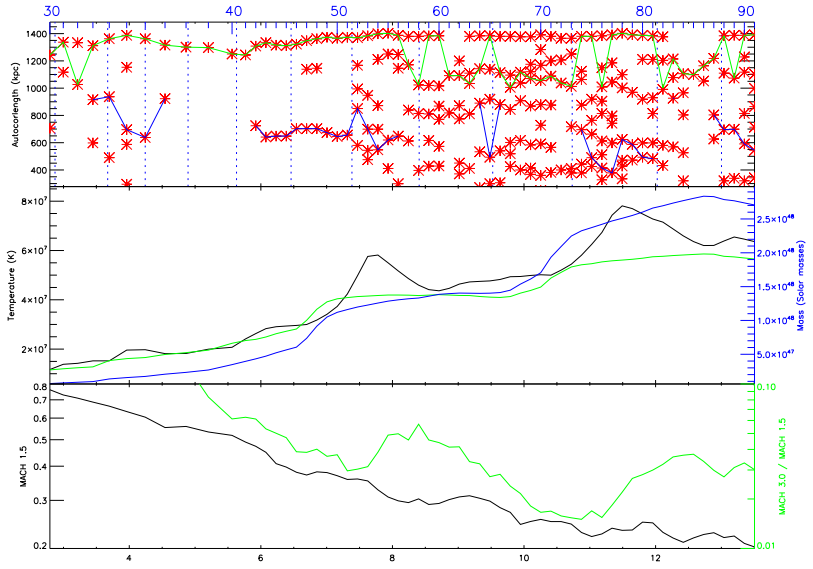

Figure 32: Magnetic autocorrelation length of the g72 cluster for a 2000 kpc box with a resolution of 256^3 grid cells. The red stars in the first plot stand for a local minimum of the autocorrelation function at that time. The green line shows the global minimum for $r > 1000$ kpc. If the global minimum of the autocorrelation function is located at a radius beneath 1000 kpc for at least 2 successive snapshots, the blue line is drawn. Dashed blue lines mark the points where a smoothing of the magnetic field happened.
The second plot shows the virial mass (blue), the temperature (black) and the virial temperature (green) of the cluster.
The black line in the third plot shows the fraction of particles within the box that have a Mach number larger than 1.5. The green line shows the quotient between the number of particles with a Mach number larger than 3 and the number of particles with a Mach number larger than 1.5.

that disappear after some time. Usually the global minimum of the autocorrelation function is at the 1400 kpc minimum, but there are some periods where the global minimum is at much smaller distances between 400kpc and 800kpc (blue lines in the upper plot). The amount and strength of minima on smaller distances seem to be connected with the temperature of the cluster, caused by the merger events. They are created by compressions that are caused by the interaction and forces between the core of the merging halo and the core of the cluster. If the core of the halo is not destroyed during its first passage through the core of the cluster, it will be pass a second time, as discussed before. With this second pass about 1.5 Gyears later, again the global minimum of the autocorrelation function moves down to smaller scales.

Therefore the second plot of figure 32 shows mass, temperature and virial temperature of the g72 cluster. Here the virial temperature is defined by assuming a power law for the relation between mass and temperature as

$$T_{Vir} = C \cdot (m \cdot h)^{\alpha} \tag{67}$$

where h is the time dependent Hubble function and C and α are two constants that are used to fit the temperature to the mass. These parameters are the result of the fitting of many more simulated clusters. Here it is used as the reference temperature of a cluster with the present mass to see when the cluster is not in equilibrium. While the temperature is larger than the from the power law expected virial temperature, the number (more stars in the first plot) and strength of the minima on smaller distances is increased (blue curve in the upper plot appears). This suggests, that when the cluster is not in equilibrium, the residual small scale motions significantly stretch and bend the magnetic field. Hence the in this case very inhomogeneous velocity field leads to a magnetic field tangled on various different scales.

The heating of the intercluster gas in SPH simulations is mainly caused by shocks that have their origin in minor and major mergers. The strength of a shock that runs through the gas can be estimated by its Mach number, that can be derived for a non-radiative polytropic gas from the Rankine-Hugoniot conditions.

$$\frac{\rho_2}{\rho_1} = \frac{(\gamma+1)\mathcal{M}_1^2}{(\gamma-1)\mathcal{M}_1^2+2} \tag{68}$$

Where ρ_1 and ρ_2 are the densities before and behind the shock, γ is the adiabatic index of the gas and $\mathcal{M}_1$ is the Mach number (for more details see [PSEJ06]). This way a Mach number for each SPH particles can be calculated.

This number we use as another indicator for the effects of mergers and the equilibrium situation of the cluster. Therefore the third plot of figure 32 provides information about the Mach numbers of the individual particles inside the cluster. It shows the fraction of particles that have a higher Mach number than 1.5. Over the hole time this fraction decreases, as the cluster is not in equilibrium in the beginning but relaxes with time. The overall number of shocked particles is not significantly affected by mergers, however it has a large effect on the fraction of HIGH Mach shocks (also shown in figure 32 as ratio between the fraction of shocks with Mach number larger than 3 and the fraction of shocks with Mach number larger than 1.5), that is increased by the merger. This high Mach shocks reflect very well the late state of

the merger, where the well known strong outgoing shock is formed. These effects take place after the meeting of the two cores, when the temperature is already decreasing again.

It is also interesting to mention, that the high Mach shocks exist much longer than the temperature peak. This shows that there are thermal activities within the cluster also a long time after the merger and explains why the cluster does not relax between the two merger events. Therefore the structure of the magnetic field stays complex all the time since it became complex in the first major merger.

An overview on the evolution of the magnetic autocorrelation function is given in figure 33. It shows the autocorrelation function for every second snapshot from 32 to 90. The first thing one can see is that the curves do not look very similar. So they may have only one dominant or more minima and the minima also change their shape and position. The function is rather smooth in the beginning, after the first merger starting around snapshot 51 there is much more structure visible. One can also see how minima evolve. They first occur as local minimum somewhere in the curve, than grow deeper and deeper until they are the global minimum for one or two snapshots. Afterwards they become weaker again and vanish finally. This represents individual structures in the magnetic field that are caused by dynamic processes within the cluster, that are mostly triggered by mergers.

6.1.6 Magnetic power spectrum

The magnetic power spectrum gives direct information how much power there is in the magnetic field on different scales. Figure 34 shows the power spectra of the g72 cluster for every second snapshot from 32 to 90. The power spectrum consists of two parts. For small values of k the increases until it reaches a maximum. The position of this maximum is around 10 $\frac{1}{\text{Mpc}}$ at the beginning and moves to higher k with time. After its maximum it decreases rapidly. The increase from very large scales to smaller scales is expected, as the magnetic field should not be dominated by very large scales. This can also be seen radial distribution of the magnetic energy (figure 30). The green line at 10% of the virial radius of the cluster corresponds to its core radius.

The increasing part of the power spectrum can basically be fitted by a power law. The decreasing part of the spectrum does not show a definite power law behavior. Its curvature depends strongly on the lengthscale chosen for the fit. The blue lines in figure 34 show the minimum, average and

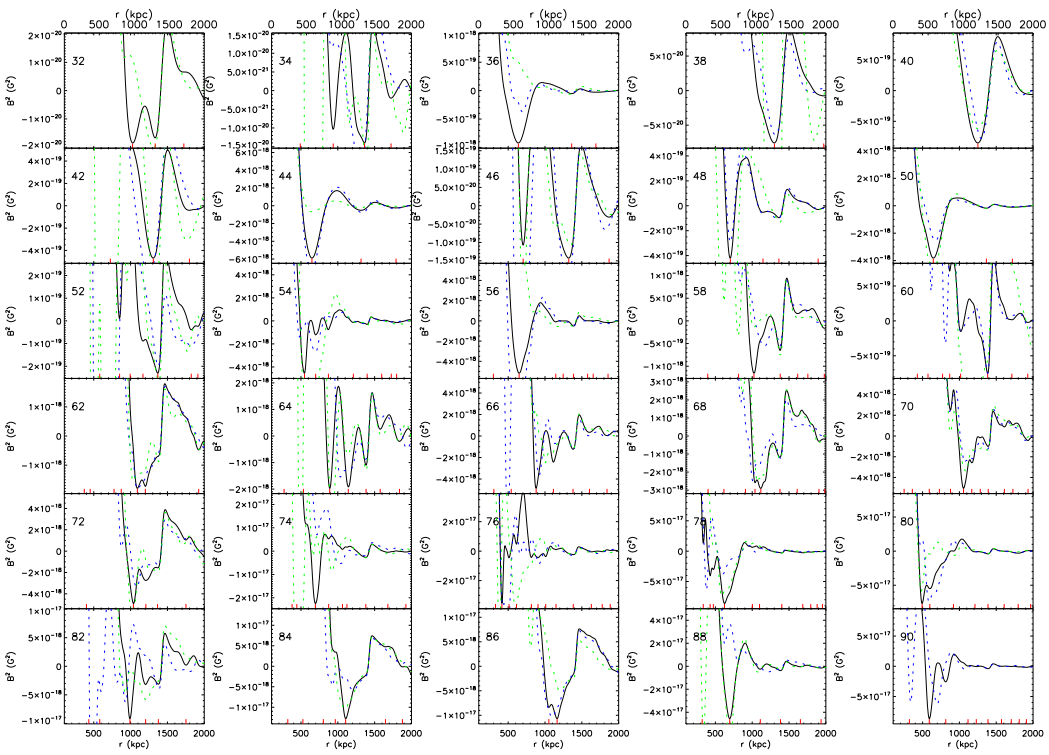

Figure 33: Autocorrelation function for every second snapshots between 32 and 90. X-axis is in kpc, y-axis in G^2. All plots (except the first and the last one) have 3 lines, the autocorrelation function of this snapshot (black), of the last snapshot (blue, dashed) and the next snapshot (green, dashed). Red vertical lines at the bottom show that there is a local minimum of the autocorrelation function at this radius, even though it may not be visible as it is only a local minimum that is too high.

maximum smoothing length of all particles whose center is inside the box. They show, that for the best resolution we know the power spectrum over two orders of magnitude. But as this resolution is only reached in small areas of high density, the power spectrum is influenced by resolution effects on one of these two orders of magnitude.

One thing to note is that both broad peak in the temperature at about 7.5Gyears and 11.5Gyears correspond to larger changes in the power spectrum in snapshots 52 and 78. As the power spectrum is directly connected to the magnetic energy, this represents an increase of magnetic energy on small scales (large k).

To track the evolution of the power spectrum I fitted a power law to 3

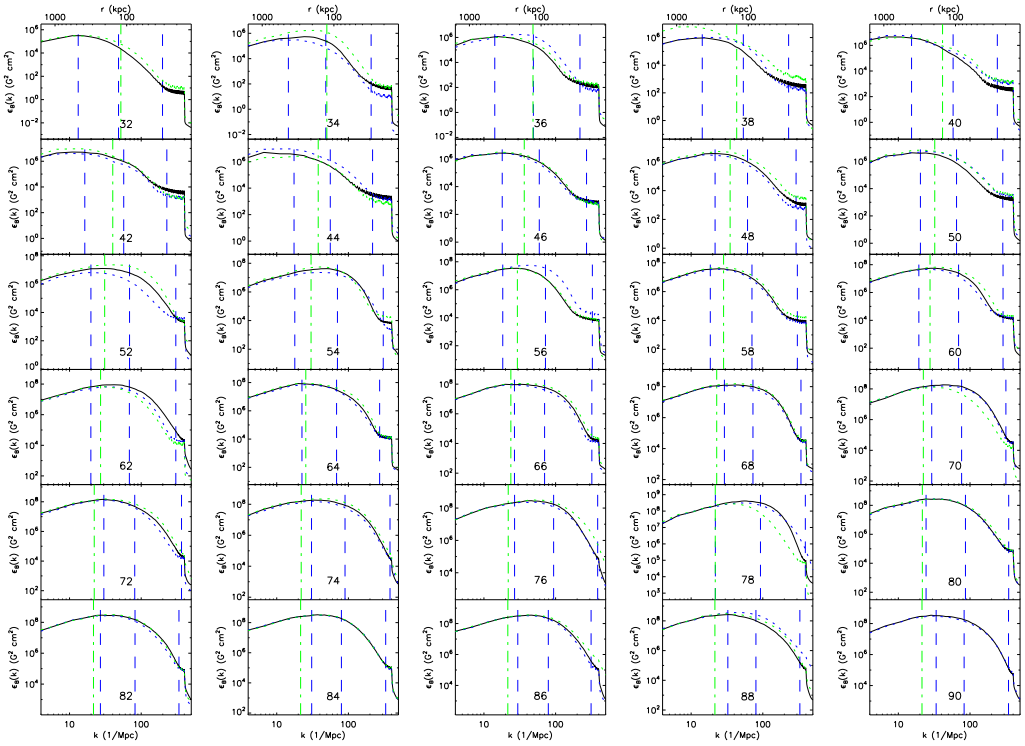

Figure 34: Magnetic power spectrum for snapshots 31 - 90. All plots (except the first and the last one) have 3 lines, the power spectrum of this snapshot (black), of the last snapshot (blue, dashed) and the next snapshot (green, dashed). Vertical blue dashed lines show, from left to right, the maximum, average and minimum smoothing length of the particles within the grid used for the calculation of the power spectrum. The vertical green dashed line represents 10% of the virial radius of the cluster.

different k around 20 $\frac{1}{\text{Mpc}}$, 100 $\frac{1}{\text{Mpc}}$ and 200 $\frac{1}{\text{Mpc}}$. The first one is, except for the very first snapshots, in the increasing part of the power spectrum and is near 10% of the virial radius of the latest snapshot. The other two are in the decreasing part of the power spectrum. Both are scales that not completely resolved any more, so their values have to be considered carefully, especially the last one that is already lower than the average smoothing length. The fits on these 3 scales is exemplarily shown for the last snapshot of the simulation in figure 35.

Figure 36 show the evolution of the spectral indexes obtained by fitting these power laws. As the spectral index is the exponent in the power law, the lower its value is the steeper decreases the power spectrum where it was fitted. The spectral index for 20 $\frac{1}{\text{Mpc}}$ reaches a constant value at about 0.5 after the first merger. The spectral index for 100 $\frac{1}{\text{Mpc}}$ grows with time, reaching -2.5

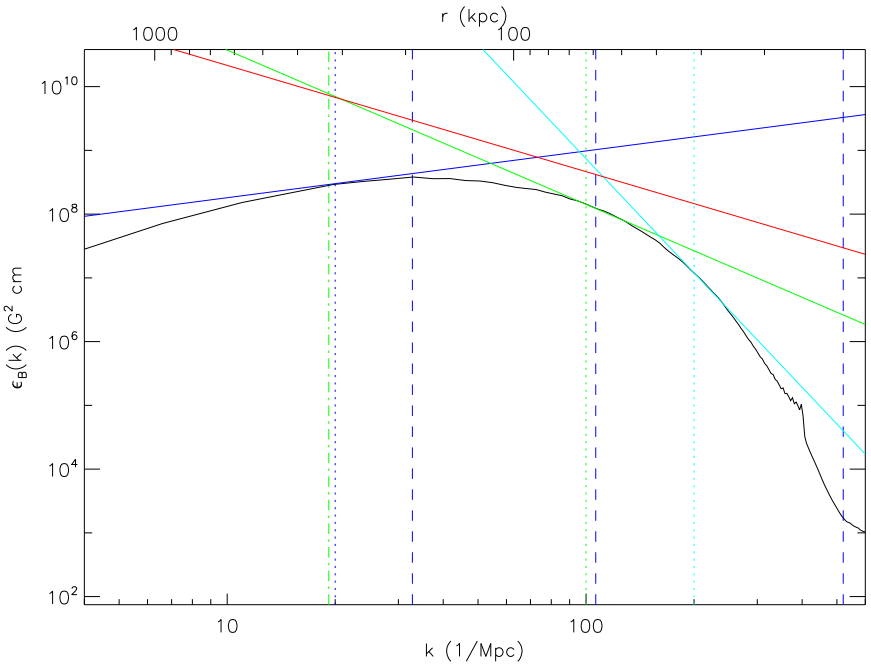

Figure 35: Magnetic power spectrum of snapshot 92 of the g72 cluster. Blue, green and cyan lines show the power law fits to the spectrum. Dotted vertical lines mark the points the power laws were fitted around. The red line shows the -5/3 power law of a Kolmogorov spectrum. Vertical blue dashed lines show, from left to right, the maximum, average and minimum smoothing length of the particles within the grid used for the calculation of the power spectrum. The vertical green dashed line represents 10% of the virial radius of the cluster.

in the end, but shows large deviations. The third spectral index for 200 $\frac{1}{\text{Mpc}}$ starts with a much higher value than the second but decreases with time and reaches -6 in the end. It is important to mention that this last index is fitted on a scale where the power spectrum has to be doubted.

For magnetic turbulence the power spectrum would follow a power law with a spectral index of -5/3. This is, in contradiction to observations, not yet visible in simulations. It is even not clear, that the power spectrum follows a power law over an appreciable range for more than single snapshots. However at this point one has to consider that the observed power spectra capture only much smaller scales ($k > \frac{1000}{\text{Mpc}}$) than present simulations. The maximum resolution of the simulation is due to its adaptive nature basically able to reach these scales. However, the effective resolution of the power spectrum of the magnetic field is one order of magnitude worse, as in the region where

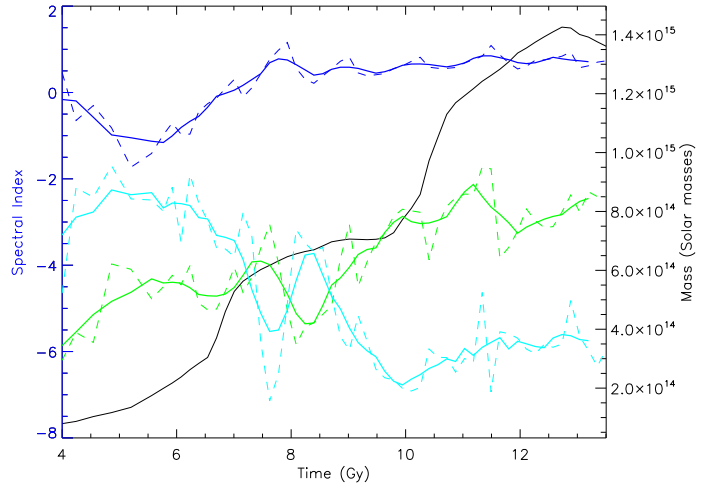

Figure 36: Spectral index of the power law fits on the magnetic power spectrum of the g72 cluster for fitting points at 20 $\frac{1}{\mathrm{Mpc}}$ (blue), 100 $\frac{1}{\mathrm{Mpc}}$ (green) and 200 $\frac{1}{\mathrm{Mpc}}$ (cyan). Dashed lines show the exact spectral indexes, the straight line is smoothed over 5 points. For comparison also the mass of the cluster is shown.

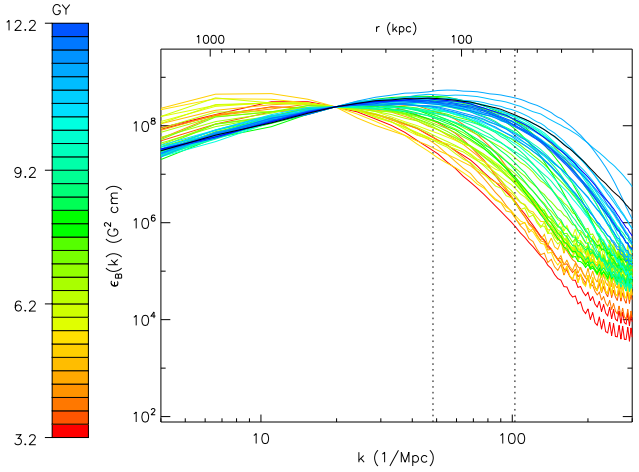

Figure 37: Magnetic power spectra of the g72 cluster from 3.2 to 12.2 Gyears on top of each other. The power spectra are normalised by multiplying with a constant to have the same value for k = 20 $\frac{1}{\mathrm{Mpc}}$. The black dashed lines show the average smoothing length of all particles inside the box for the earliest (left) and latest (right) snapshot whose power spectrum is plotted. Scales below this average smoothing length are not reliably resolved.

the power spectrum is calculated the maximum of the simulation resolution is not reached everywhere. So for a direct comparison of the observed and simulated magnetic power spectra, at least one additional order of magnitude of the spatial resolution is needed. Nevertheless it is possible to compare the relative evolution of the power spectra with other properties of the simulated clusters.

The relative evolution of the magnetic power spectrum can be seen in figure 37. It shows the normalised power spectra on top of each other. The power spectra seem do do some kind of turning around the point where they are fixed. So the increasing part of the power spectrum becomes larger, while the decreasing part starts later and decreases steeper. Also the position of the maximum of the power spectrum that is similar to the scale that carries the highest part of the magnetic energy moves from some 100 kpc to 100 kpc. This agrees with the magnetic energy distribution we got from the direct calculation of the magnetic energy on different scales before. In general the evolution of the magnetic power spectra seems not to be dominated by the mergers themselves, but by the non equilibrium situation of the cluster afterwards.

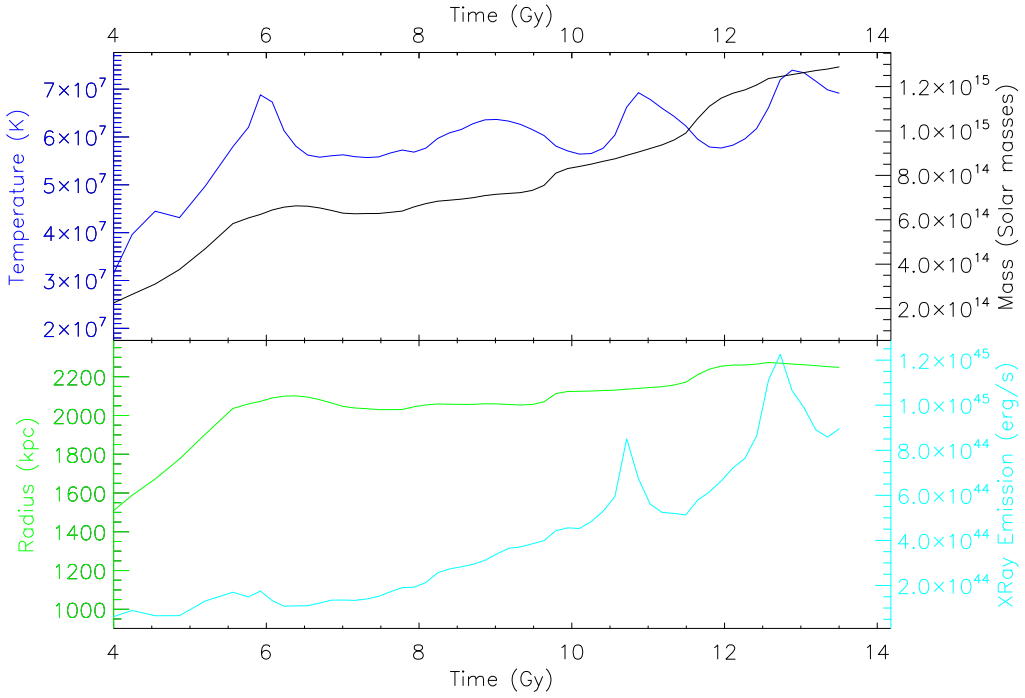

Figure 38: Time evolution of temperature, x-ray luminosity and radius of the g51 cluster.

6.2 The g51 cluster

The evolution of the g51 cluster is more quiet than the g72 cluster. It has one early major merger at 5.5Gyears and then stays quiet for 4Gyears. Afterwards it has two smaller mergers, one merger with a mass ratio of 8:1 at 9.7 Gyears and another merger with a mass ratio of 5:1 at 11.5 Gyears. For the early major merger is is not possible to get an usable mass ratio, as the other halos that merge with the cluster are not yet completely bound. The basic propepropertieshe g51 cluster are shown in figure 38. One can see, that the mergers are again followed an increase of the temperature and x-ray luminosity about one Gyear later, as for the g72 cluster. This time delay between the beginning of the merger and the rising of these quantities is the same for both clusters, although the merger itself is much shorter and the increase of the mass of the cluster already finished more than half a Gyear earlier. Instead it can be explained as the time that is needed for the halo to travel through the cluster into its center.

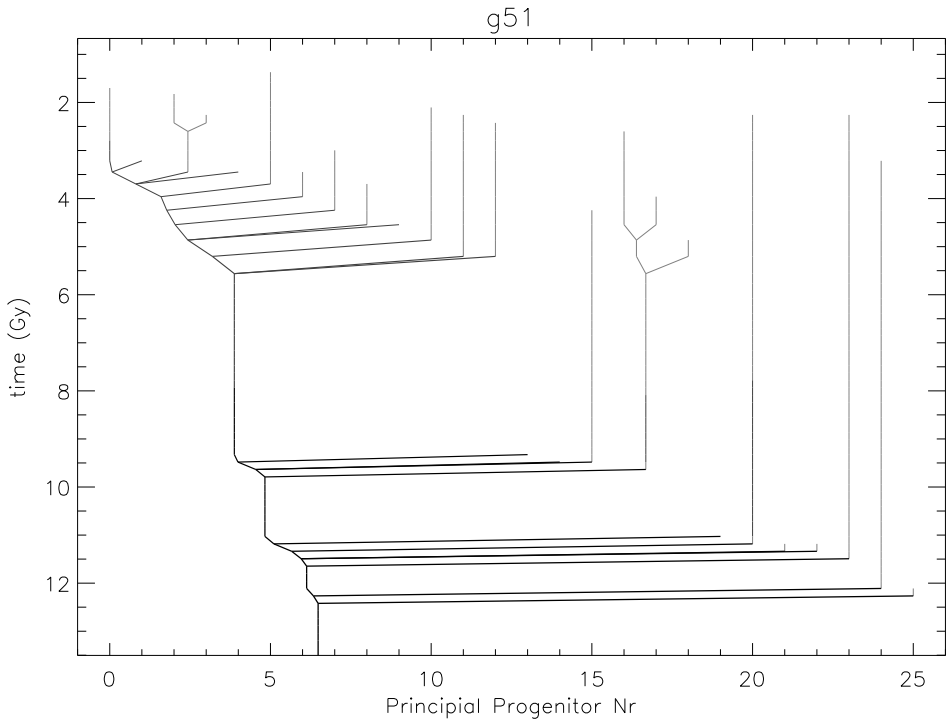

Figure 39: Merger tree of the g51 cluster. The darker and bigger the line is, the more massive is the cluster.

6.2.1 Merger history

Figure 39 displays the merger tree of the g51 cluster. It has one early broad merger and is then quiet. At 9Gyears it has two mergers. Both mergers last only about half an Gyear. This may be due to the fact that both eaten clusters are rather small and light. Therefore they need less time from the beginning of the merger when the two clusters touch to the point where the smaller cluster is completely part of the larger cluster.

6.2.2 Energies

Figure 40 shows the evolution of inner, kinetic and magnetic energy of the g51 cluster. The inner energy increases slowly with time (about one order of magnitude over the whole time) and is also only slightly influenced by the mergers. The kinetic energy of the cluster is nearly constant and peaks only temporarily in the 3 mergers. The magnetic energy grows up nearly 3 orders

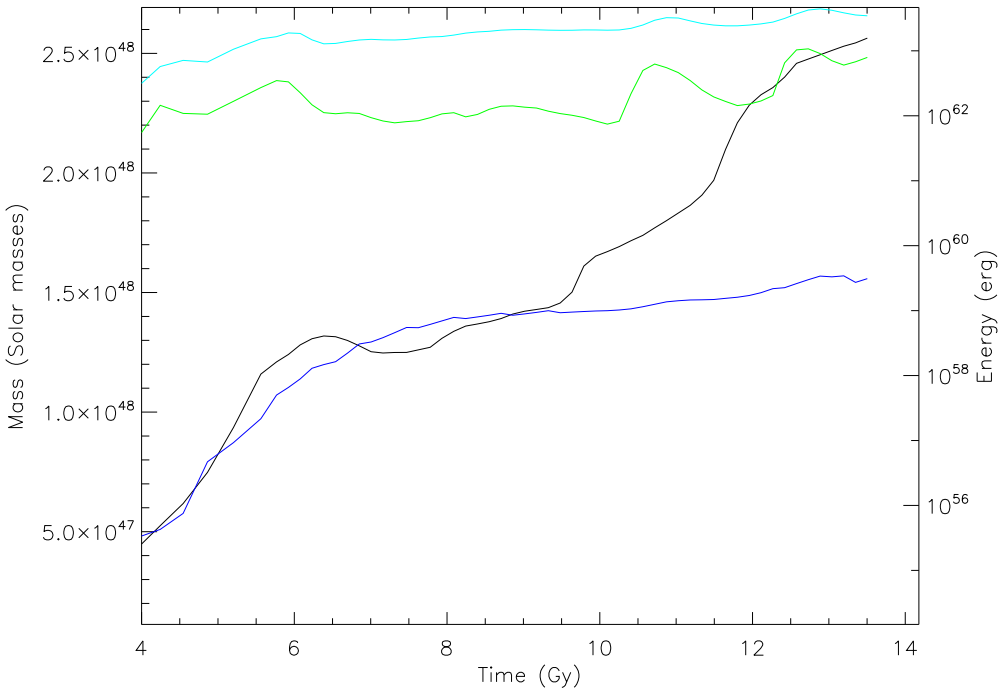

Figure 40: Time evolution of total kinetic energy (green), inner energy (cyan) and magnetic energy (blue) in a 2Mpc box centered at the center of the g51 cluster with a resolution of 256^3 grid points. The magnetic energy was smoothed using 2 steps in the future and to steps in the past. For comparison also the mass (black) of the cluster is plotted.

of magnitude in the early major merger until it is saturated. After that it stays constant and is even not changed by the late mergers.

6.2.3 Kinetic & magnetic energy

The distribution of the kinetic energy of the g51 cluster on different scales, that is shown in figure 41, is similar to the g72 cluster. The kinetic energy is mainly on large scales, therefore lies in large scale motions of the particles. The mergers affect all scales similarly. Scales smaller equal to and than 125kpc change almost parallel, so they seem not to be resolved good enough any more.

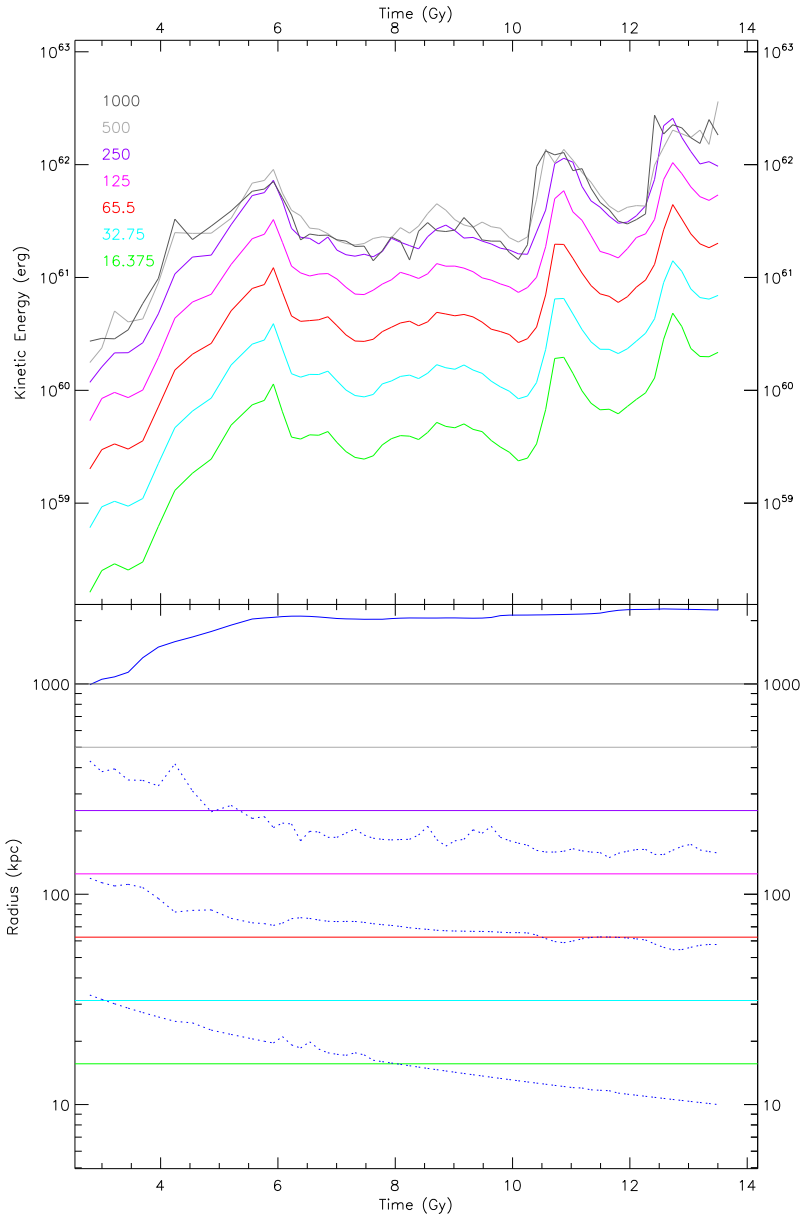

Figure 41: Time dependent kinetic energy on different scales in a 2Mpc box centered on the g51 cluster with a resolution of 256^3 grid points. Colored lines in the upper plot (except the blue line) show the magnetic energy on scales between their scale and the next smaller scale. The scales are given by averaging over a number of grid cells, that is written in the lower left corner. So the green line shows the kinetic energy on the smallest scales, while the black line shows it on the largest scales. Colored lines in the lower plot (again except the blue lines) show the distance that was averaged over for the kinetic energy line of the same color. The blue line shows the virial radius of the cluster. Dashed blue lines (from the highest to the lowest line) stand for the maximum, average and minimum smoothing length of the particles within the given box.

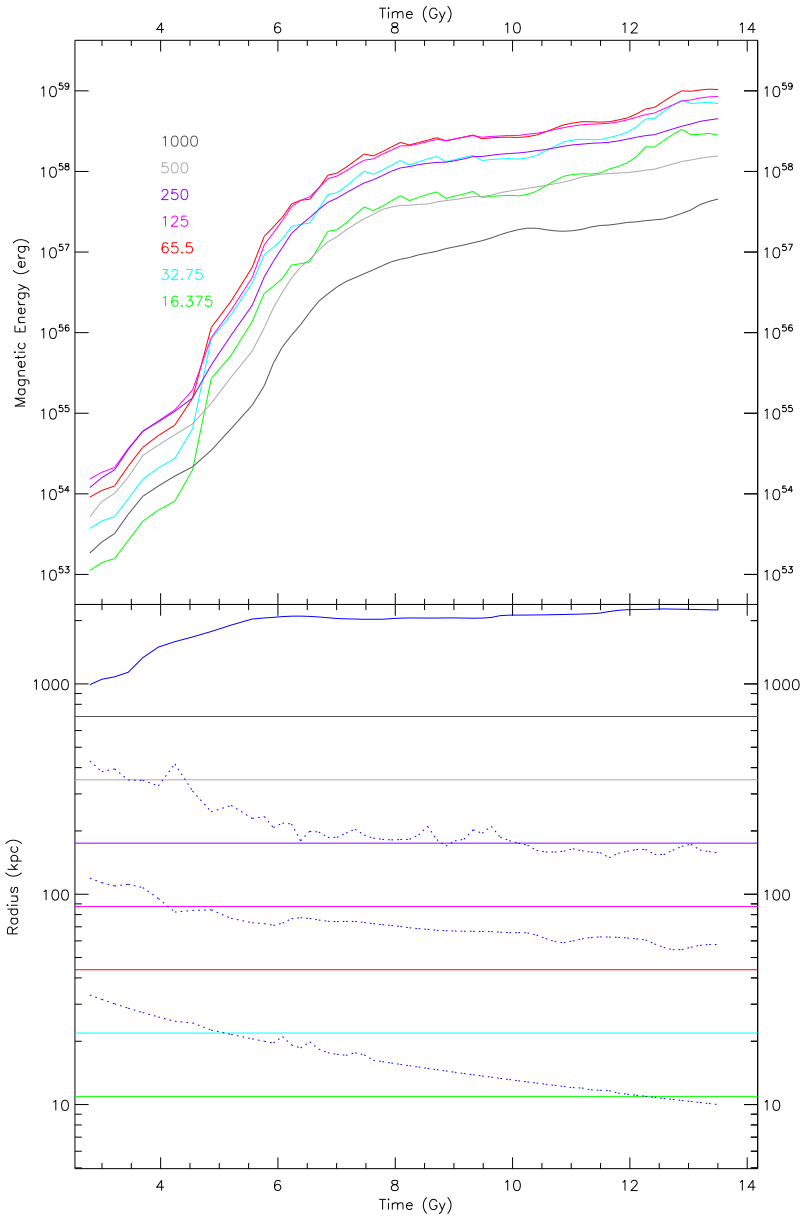

Figure 42: Time dependent magnetic energy on different scales in a 2Mpc box centered on the g51 cluster with a resolution of 256^3 grid points. The magnetic energy was smoothed using 2 steps in the future and to steps in the past. Colored lines (except the blue line) show the magnetic energy on scales between their scale and the next smaller scale. The scales are given by averaging over a number of grid cells, that is written in the lower left corner. So the green line shows the magnetic energy on the smallest scales, while the black line shows the largest scales. Colored lines (again except the blue lines) show the distance that was averaged over for the magnetic energy line of the same color. The blue line shows the virial radius of the cluster. Dashed blue lines (from the highest to the lowest line) stand for the maximum, average and minimum smoothing length of the particles within the given box.

The magnetic energy is dominated by energies on small scales, as shown in figure 42. With time, the fraction of energy that sits on large scales becomes even smaller. The magnetic energy is not affected by the late mergers on any scales, but amplified in the early merger on all scales.

Figure 43 shows the evolution of the x-ray emissions of the g51 cluster. Even more clearly as for the g71 cluster one can see here how halos merge with the cluster.

6.2.4 Magnetic autocorrelation function

The magnetic autocorrelation function of the g51 cluster is shown in figure 44. It shows the same global minimum as the g72 cluster. Also, like the g72 cluster, the magnetic field is swirled in the first major merger and therefore many additional minima in the autocorrelation function are created. However 4 Gyears after the merger, the magnetic field is relaxed again and nearly all additional minima at smaller scales vanished. This effect does not happen in the g72 cluster, as the first major merger there is followed by the second only less than 3 Gyears later. Also the strong shocks in the g51 cluster vanish more than 1 Gyear before the second merger starts. After they vanished the magnetic field is not influenced by dynamics effects until the second merger, so it is able to relax. With the second and third mergers of the g51 cluster, there are again new minima of the autocorrelation function created. Indeed this time there are only a few minima, as the two halos merge with the cluster are significantly less massive than the cluster. This can also be seen in the third plot of figure 44. There the first major merger causes a large number of high energetic shocks, while the late mergers only create very few.

6.2.5 Magnetic power spectrum

Fits of a power law to the magnetic power spectra of the g51 cluster at 20 $\frac{1}{\text{Mpc}}$, 100 $\frac{1}{\text{Mpc}}$ and 200 $\frac{1}{\text{Mpc}}$ are shown in figure 45. All 3 spectral indexes obtained this way do not change very much with time. They stay around 0, between -3 and -4 and around -6. This evolution is different to the g72 cluster, where the spectral indexes of the power spectra evolve with time. This may be due to the fact that the g51 cluster is quiet after the first major merger, while the g72 cluster is affected by its 2 major mergers all the time.

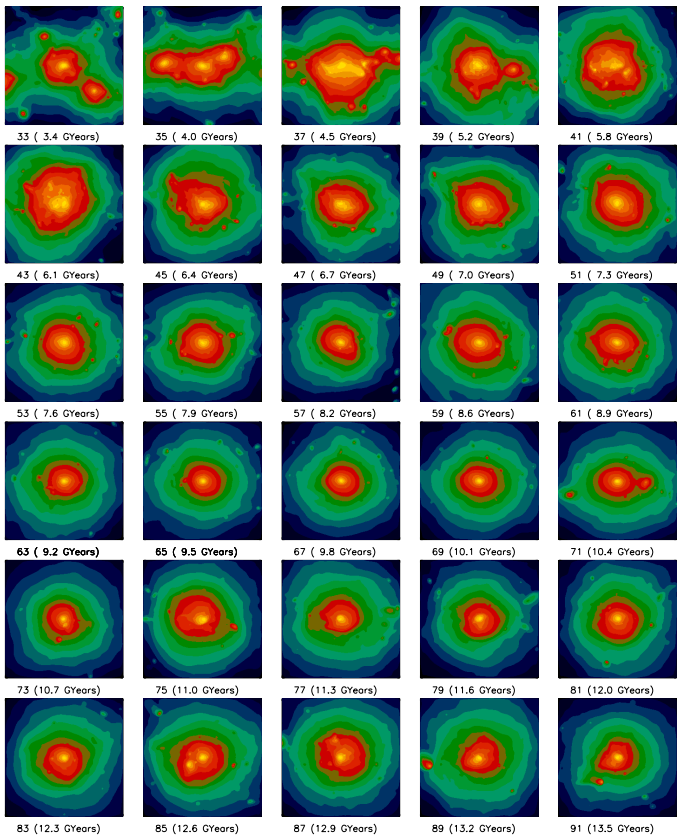

Figure 43: X-ray luminosity map of every second snapshot between 33 and 91 of the g51 cluster. The luminosity increases from blue via green and red to yellow where it is maximal.

A similar result can be obtained from the comparison of the evolution of the power spectrum as a whole of both clusters. The power spectrum of the g51 cluster is strongly affected only by the early first major merger of the cluster. This merger increases the relative amount of magnetic energy on small scales (large k) and moves the maximum of the power spectrum down to scales around 100kpc. After the merger the cluster relaxes and magnetic energy on small scales decreases again while the maximum moves to larger

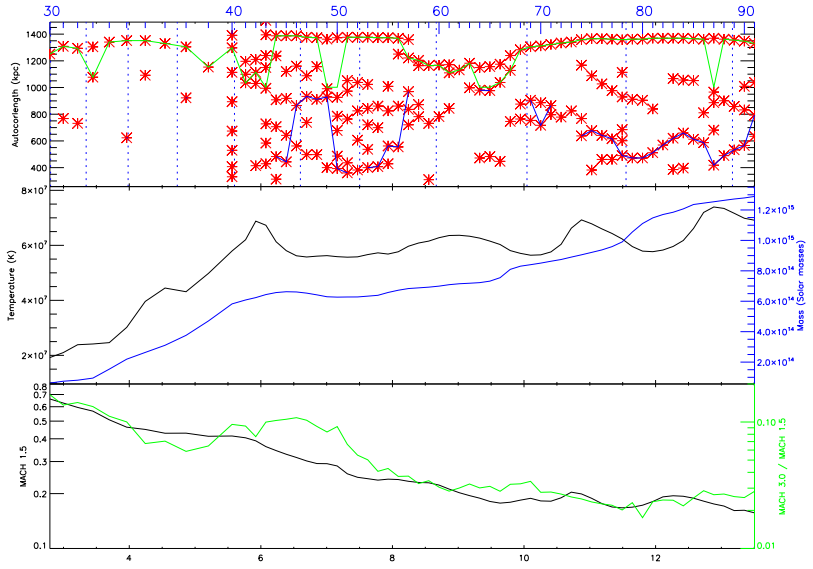

Figure 44: Magnetic autocorrelation length of the g51 cluster for a 2000 kpc box with a resolution of 256^3 grid cells. The red stars in the first plot stand for a local minimum of the autocorrelation function at that time. The green line shows the global minimum for $r > 1000$ kpc. If the global minimum of the autocorrelation function is located at a radius beneath 1000 kpc for at least 2 successive snapshots, the blue line is drawn. Dashed blue lines mark the points where a smoothing of the magnetic field happened.
The second plot shows the virial mass (blue), the temperature (black) and the virial temperature (green) of the cluster.
The black line in the third plot shows the fraction of particles within the box that have a Mach number larger than 1.5. The green line shows the quotient between the number of particles with a Mach number larger than 3 and the number of particles with a Mach number larger than 1.5.

scales. After the cluster has relaxed, the power spectrum does not change significantly any more. The different evolutions of the g72 and g51 clusters is also visible in the spread that is covered by the power spectra in figures 37 and 46. The fact that the spread is about twice as large for the g72 cluster as for the g51 cluster again shows that the g72 cluster is more out of equilibrium as a result of its merging history.

The evolution of magnetic power spectrum of the g72 cluster shows the same evolution for the first major merger. But before the cluster had enough time to relax, the second major merger pushes this evolution forward, leading to a continuous growth of the magnetic energy on small scales and movement of the maximum of the power spectrum to smaller scales.

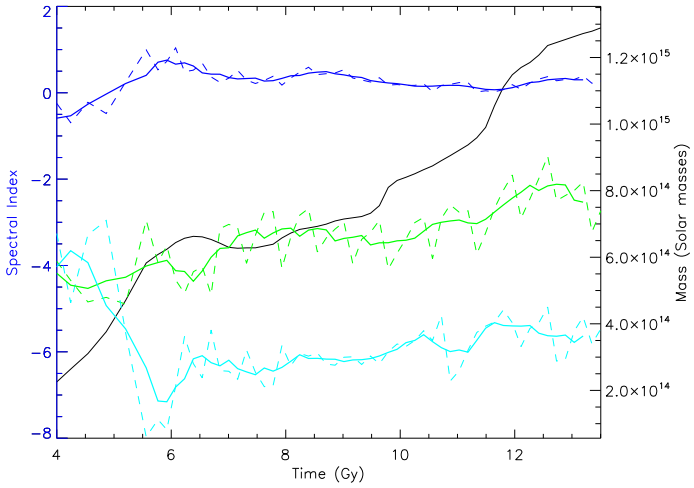

Figure 45: Spectral index of the power law fits on the magnetic power spectrum of the g51 cluster for fitting points at 20 $\frac{1}{\text{Mpc}}$ (blue), 100 $\frac{1}{\text{Mpc}}$ (green) and 200 $\frac{1}{\text{Mpc}}$ (cyan). Dashed lines show the exact spectral indexes, the straight line is smoothed over 5 points. For comparison also the mass of the cluster is shown.

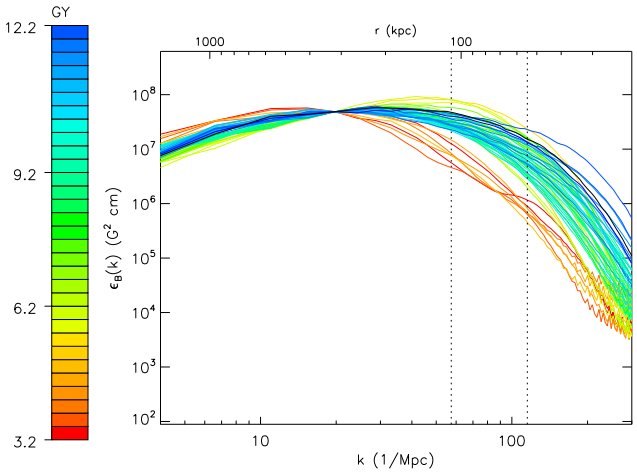

Figure 46: Magnetic power spectra of the g51 cluster from 3.2 to 12.2 Gyears on top of each other. The power spectra are normalised by multiplying with a constant to have the same value for k = 20 $\frac{1}{\text{Mpc}}$. The black dashed lines show the average smoothing length of all particles inside the box for the earliest (left) and latest (right) snapshot whose power spectrum is plotted. Scales below this average smoothing length are not reliably resolved.

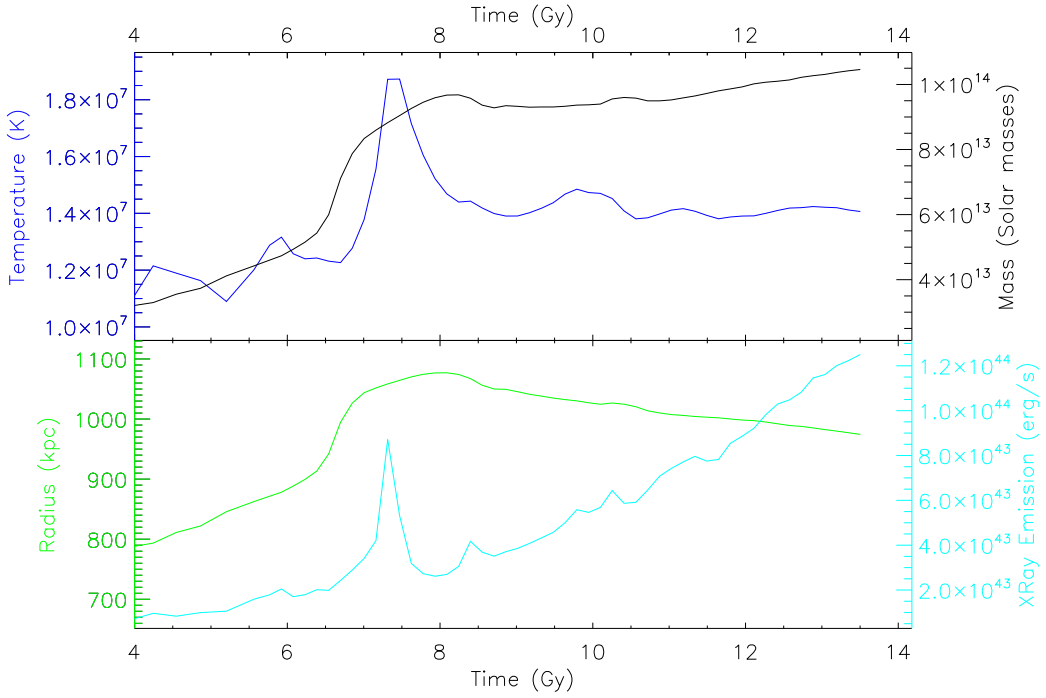

Figure 47: Time evolution of temperature, x-ray luminosity and radius of the g676 cluster.

6.3 The g676 cluster

The g676 cluster is one order of magnitude less massive than the other two clusters. It has only one major merger with a mass ratio of 1:1 that starts at 6.5 Gyears. Figure 47 shows the evolution of mass, radius, temperature and x-ray luminosity of the cluster. The temperature of the cluster increases before the merger and peaks about 0.7 Gyears after the merger. The peak follows the merger faster than for the g72 and g51 cluster, as the g676 cluster is much smaller and halo needs less time to reach the cluster center. After the merger peak the temperature stays constant. The radius of the cluster also grows until the first merger happens. Afterwards the cluster collapses slowly. The x-ray luminosity has a small peak when the temperature peaks after the merger. Later it increases with time, since the cluster contracts and its electron density increases.

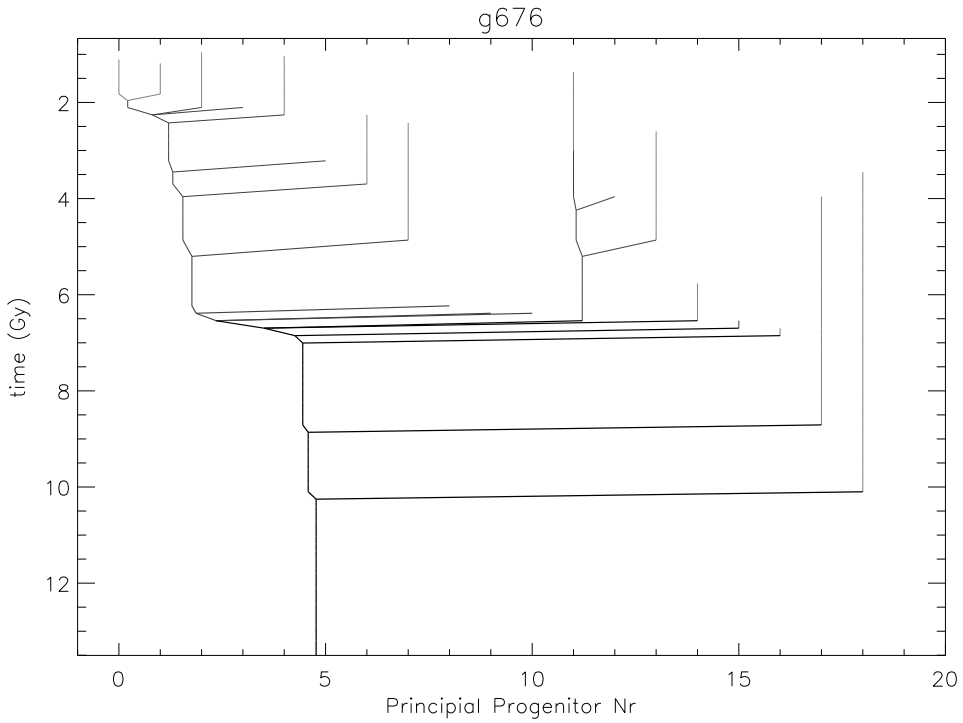

Figure 48: Merger tree of the g676 cluster. The darker and bigger the line is, the more massive is the cluster.

6.3.1 Merger history

The merger history of the g676 cluster, shown in figure 48 is rather quiet. In this figure, all halos more than 500 particles are shown, in contrast to the 5000 particle limit of the merger trees of the other 2 clusters. The major merger lasts for half a Gyear. Afterwards the cluster has two minor mergers preventing it from relaxing.

Figure 43 shows the evolution of the X-ray luminosity for the g676 cluster. The first major merger is visible clearly around 6 Gyears. Also one can see many small halos falling into the cluster in its later evolution.

6.3.2 Energies

Figure 49 shows the evolution of kinetic, inner and magnetic energy of the g676 cluster. Kinetic and inner energy are approximately constant for most

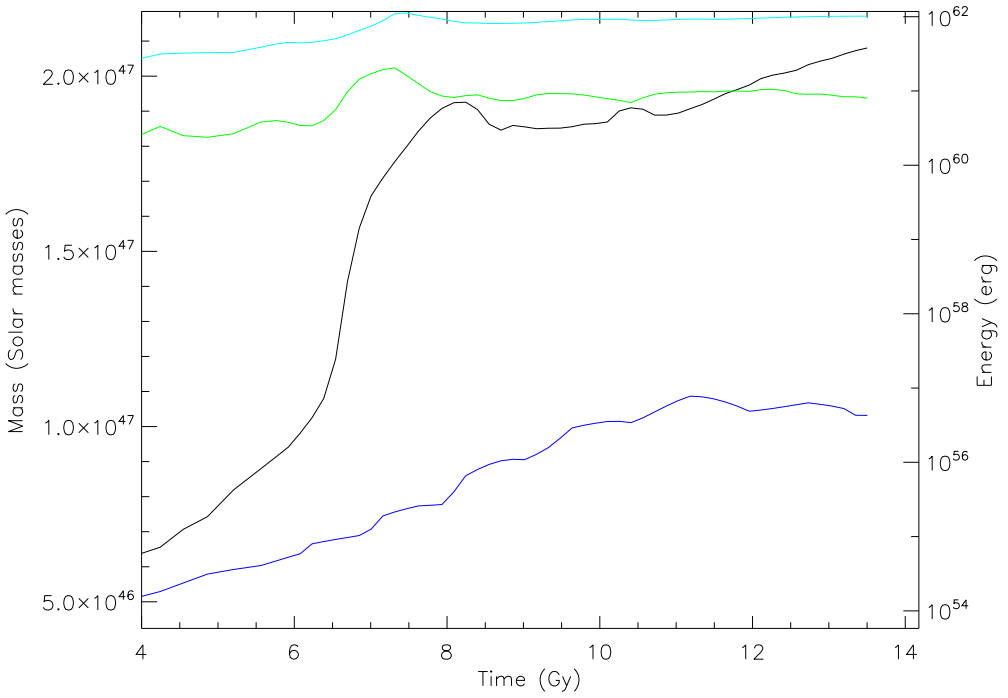

Figure 49: Time evolution of total kinetic energy (green), inner energy (cyan) and magnetic energy (blue) in a 2Mpc box centered at the center of the g676 cluster with a resolution of 256^3 grid points. The magnetic energy was smoothed using 2 steps in the future and to steps in the past. For comparison also the mass (black) of the cluster is plotted.

of the time, with a short peak at the major merger. Here the kinetic energy increases nearly with the mass of the cluster, while the inner energy increases about half a Gyear later. Both decrease to a slightly larger value than before the merger after their maximum. The magnetic energy seems to be not affected by the merger at all. It grows continuous until 10 Gyears and stays constant thereafter.

6.3.3 Kinetic & magnetic energy

Figure 50 and 51 show the evolution of kinetic and magnetic energy of the g676 cluster on different scales. One can see, that the kinetic energy is again dominated by large scale motions. The major merger affects all scales similarly. The smaller merger around 10 Gyears affects only large scales of

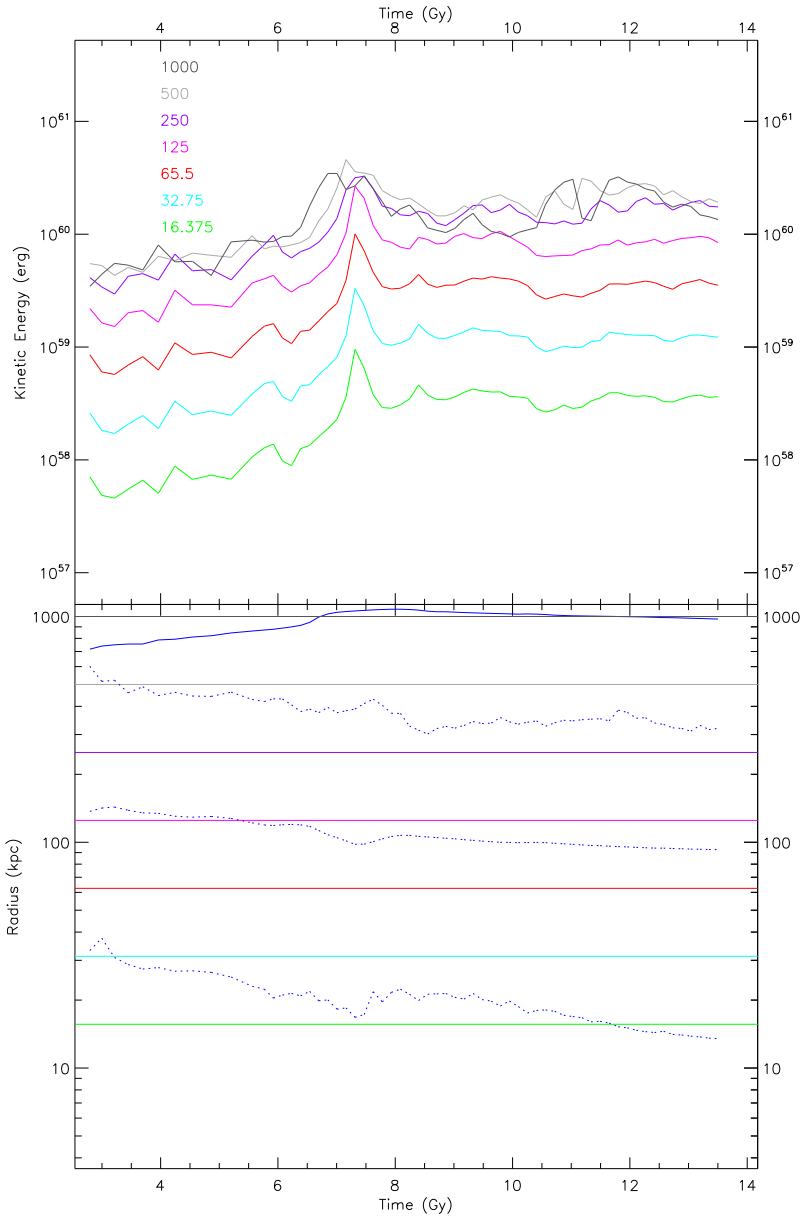

Figure 50: Time dependent kinetic energy on different scales in a 2Mpc box centered on the g676 cluster with a resolution of 256^3 grid points. Colored lines in the upper plot (except the blue line) show the magnetic energy on scales between their scale and the next smaller scale. The scales are given by averaging over a number of grid cells, that is written in the lower left corner. So the green line shows the kinetic energy on the smallest scales, while the black line shows it on the largest scales. Colored lines in the lower plot (again except the blue lines) show the distance that was averaged over for the kinetic energy line of the same color. The blue line shows the virial radius of the cluster. Dashed blue lines (from the highest to the lowest line) stand for the maximum, average and minimum smoothing length of the particles within the given box.

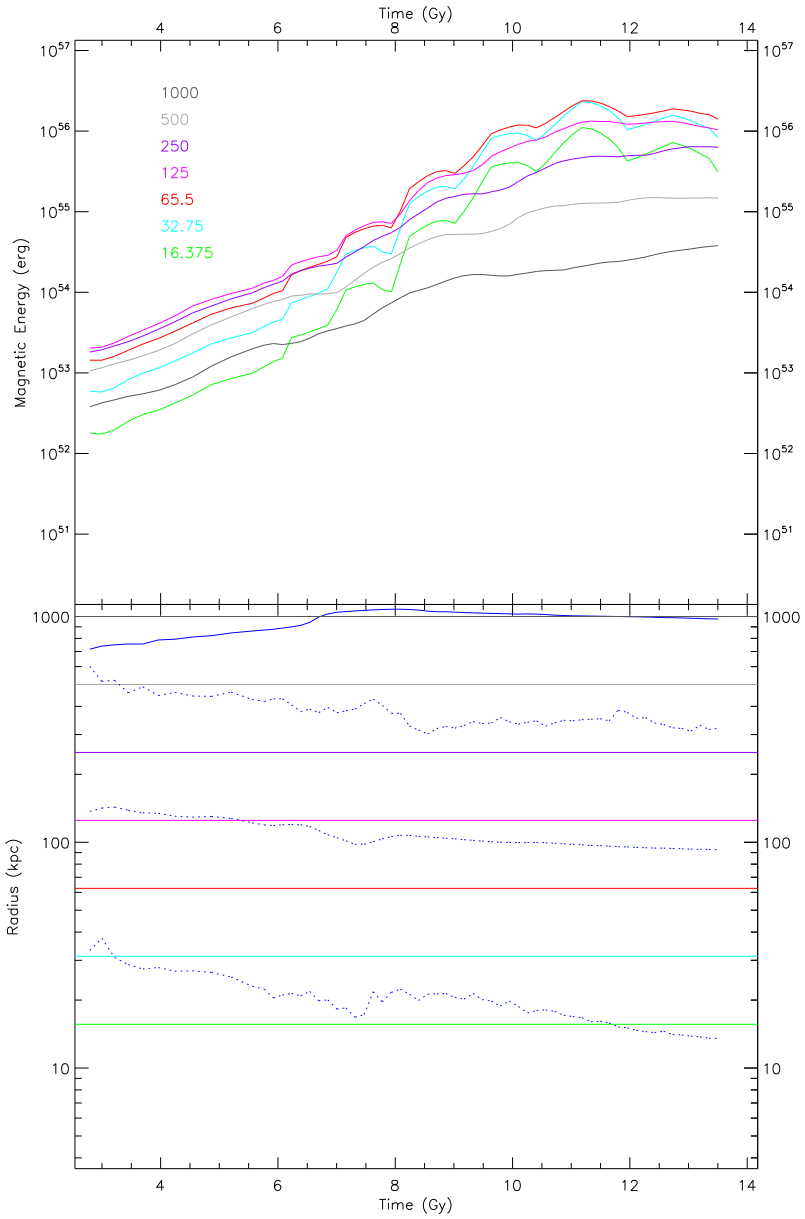

Figure 51: Time dependent magnetic energy on different scales in a 2Mpc box centered on the g676 cluster with a resolution of 256^3 grid points. The magnetic energy was smoothed using 2 steps in the future and to steps in the past. Colored lines (except the blue line) show the magnetic energy on scales between their scale and the next smaller scale. The scales are given by averaging over a number of grid cells, that is written in the lower left corner. So the green line shows the magnetic energy on the smallest scales, while the black line shows the largest scales. Colored lines (again except the blue lines) show the distance that was averaged over for the magnetic energy line of the same color. The blue line shows the virial radius of the cluster. Dashed blue lines (from the highest to the lowest line) stand for the maximum, average and minimum smoothing length of the particles within the given box.

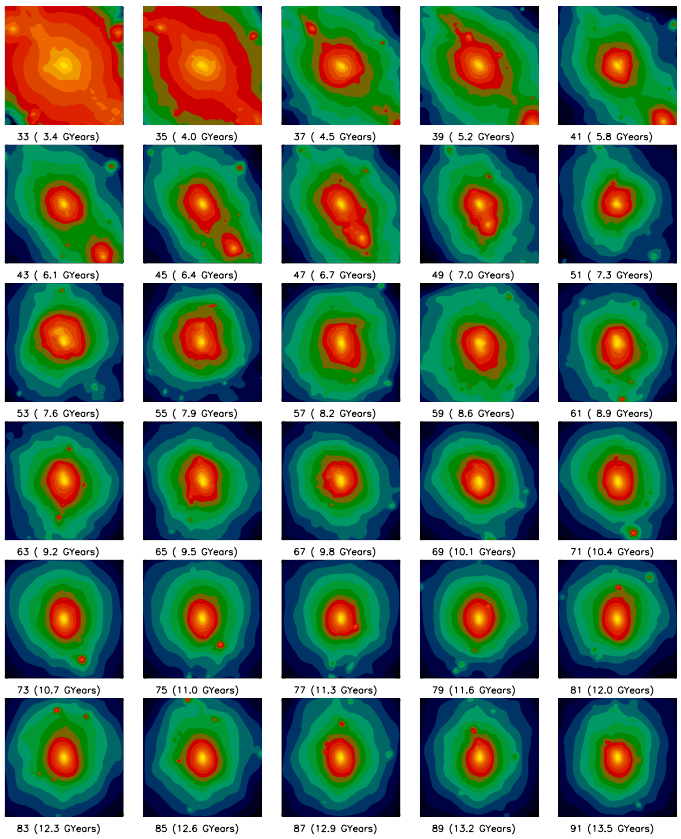

Figure 52: X-ray luminosity map of every second snapshot between 33 and 91 of the g676 cluster. The luminosity increases from blue via green and red to yellow where it is maximal.

the kinetic energy. The magnetic energy is dominated by small scales, as in the other two clusters. Also the energy grows faster on small scales than on large scales. But that the energy on scales from 100 kpc downwards changes parallel on all these scales again, is a hint that they are not well resolved.

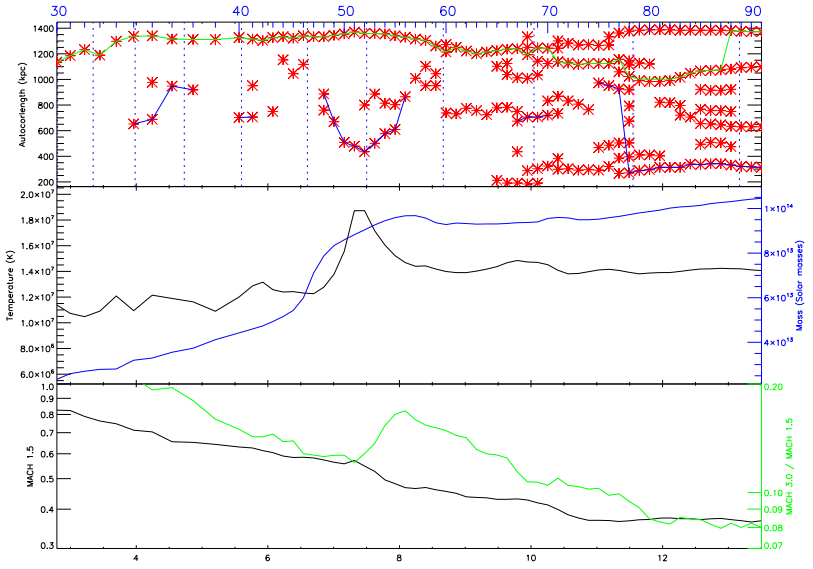

Figure 53: Magnetic autocorrelation length of the g676 cluster for a 2000 kpc box with a resolution of 256^3 grid cells. The red stars in the first plot stand for a local minimum of the autocorrelation function at that time. If the global minimum of the autocorrelation function is located at a radius beneath 1000 kpc for at least 2 successive snapshots, the blue line is drawn. Dashed blue lines mark the points where a smoothing of the magnetic field happened.
The second plot shows the virial mass (blue), the temperature (black) and the virial temperature (green) of the cluster.
The black line in the third plot shows the fraction of particles within the box that have a Mach number larger than 1.5. The green line shows the quotient between the number of particles with a Mach number larger than 3 and the number of particles with a Mach number larger than 1.5.

6.3.4 Magnetic autocorrelation function

The minima of the magnetic autocorrelation function are shown in figure 53. The minima at around 1400 kpc is visible again, and therefore does obviously not depend on the virial radius of the cluster, that is only half of the size of the g72 or g51 cluster. One can see clearly, that the at the merger the rise of the temperature comes along with a new minimum in the autocorrelation function that is created at 900 kpc. It goes down to 450 kpc at the time of the maximum temperature, increases back to 900 kpc and disappears.

The third plot of figure 53 shows that the merger creates a large number of shocks that endure in the cluster for a long time (4 Gyears). They may

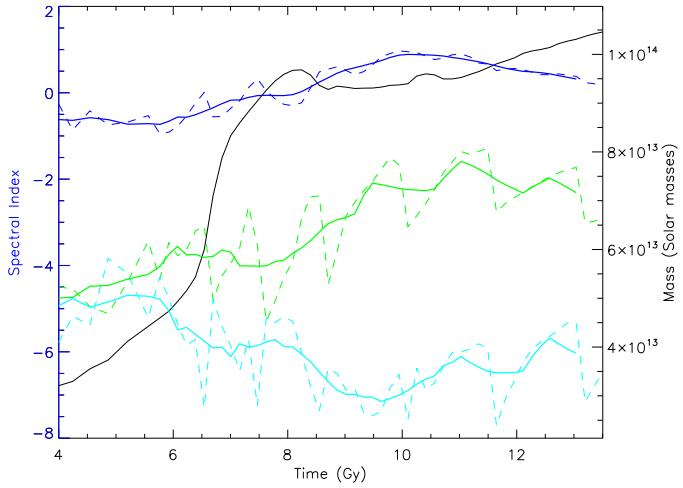

Figure 54: Spectral index of the power law fits on the magnetic power spectrum of the g676 cluster for fitting points at 20 $\frac{1}{\mathrm{Mpc}}$ (blue), 100 $\frac{1}{\mathrm{Mpc}}$ (green) and 200 $\frac{1}{\mathrm{Mpc}}$ (cyan). Dashed lines show the exact spectral indexes, the straight line is smoothed over 7 points. For comparison also the mass of the cluster is shown.

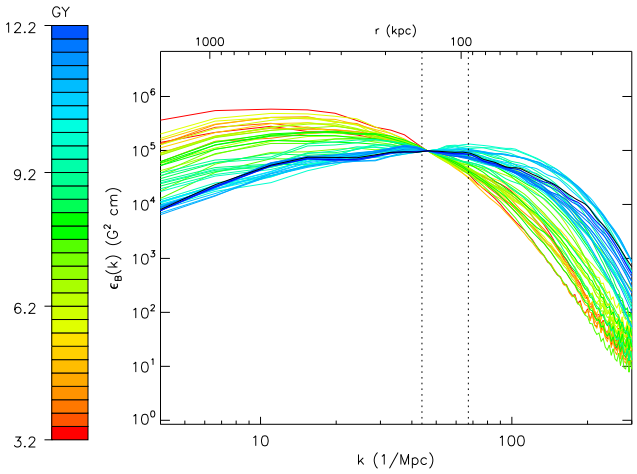

Figure 55: Magnetic power spectra of the g676 cluster from 3.2 to 12.2 Gyears on top of each other. The power spectra are normalised by multiplying with a constant to have the same value for k = 45 $\frac{1}{\mathrm{Mpc}}$. The black dashed lines show the average smoothing length of all particles inside the box for the earliest (left) and latest (right) snapshot whose power spectrum is plotted. Scales below this average smoothing length are not reliably resolved.

be the reason for the later increase of minima in the autocorrelation function that indicates that the magnetic field is broken down to smaller fields once more.

6.3.5 Magnetic power spectrum

Figure 54 shows the spectral indexes for a power law fit on the power spectra of the magnetic field of the g676 cluster at 20 $\frac{1}{\text{Mpc}}$, 100 $\frac{1}{\text{Mpc}}$ and 200 $\frac{1}{\text{Mpc}}$. The first index at 20 $\frac{1}{\text{Mpc}}$ does not change much. The index at 100 $\frac{1}{\text{Mpc}}$ increases with time, i.e. the spectrum becomes less steep at this point. The last index decreases up to the merger and stays at the same value afterwards.

The power spectra themselves are shown in figure 55. The evolution is basically the same as for the other clusters. The maximum of the power spectrum moves to higher k (smaller scales), reaching its highest value of k $\approx 70\frac{1}{\text{Mpc}}$ around 10 Gyears. From there it moves to slightly larger values again.

7 Conclusions

The best method to calculate a grid from a SPH simulation is direct sampling at the center of the grid cells using the values that are given by the SPH formalism. Only for poorly resolved grids other methods may be better. Although it is often used, the TSC method is not a good choice, as long as the grid cells are smaller than the particle that has the lowest resolution, e.g. the largest smoothing length. The modified TSC method is much better, but has a remaining error that is about one order of magnitude larger than the error of direct SPH sampling.

As already known, the simulations show, that massive mergers are followed about 1 Gyear later by an increase of the temperature and x-ray emissivity of the cluster. The time difference corresponds to the time that the infalling halo needs to reach the cluster center. If the halo is not dissolved during the first passage through the cluster center, there may be a second passage of the remaining substructures of the halo, that can also lead to additional smaller peaks in the temperature and x-ray emissivity. The increase of temperature and x-ray emissivity is due to compression and shock heating of the gas, that pushes the cluster into a non equilibrium state. This non equilibrium state is also visible in the excess of high Mach number shocks that are detected in the intra cluster medium. This effect can also be seen if the infalling halo is disrupted very fast, as it will lead to increasing gas motions in the center of the cluster where denser infalling gas is drawn in. In this way, the internal non equilibrium state of the cluster can be maintained significantly longer than its visible properties, like temperature and X-ray luminosity show, depending of the details of the merger event. The residual motions that maintain the non equilibrium state of the cluster can strongly amplify the magnetic field and change its structure. Therefore also the disorder of the magnetic field on small scales can be maintained a long time beyond the typical timescale of the merger event itself.

Kinetic and inner energies rise at the same time. The kinetic energy is dominated by large scales, therefore it represents large scale motions, that were enhanced by the merger. There is no visible evidence in the kinetic energy that a turbulent cascade build up in these simulations. This can be interpreted in a way that the kinetic energy in the gas is always dominated by the velocity field on cosmological scales, and the small scale contributions from local fluid instabilities that may cause turbulence are only minor. Another explanation is that the instabilities are suppressed by the artificial numerical viscosity of the underlying hydro scheme.

The evolution of the magnetic field is dominated by the first major merger

of the cluster. It on the one hand heavily amplifies the magnetic field by dynamical effects like shear flows. On the other hand it completely reshapes the magnetic field, destroying any memory or dependence on the seed magnetic field. After the first major merger, the evolution of the magnetic field slows down. Nevertheless the magnetic field is still amplified by compressions and shear flows of the plasma that carries the field.

The magnetic energy is dominated by small scales and the core of the cluster. It undergoes an evolution where energy is moved from large scales, where the energy is early deposited in the beginning when the magnetic field is homogeneous, to small scales. This evolution is mostly finished after the first major merger.

The magnetic autocorrelation turns out to be a good indicator of the structure of the magnetic field. This structure is the result of the dynamics inside the cluster. Mergers and their residual motions have a strong influence on the dynamics of the cluster. Therefore they produce many features in the magnetic field structure, which are visible in the magnetic autocorrelation function. The major merger events and their secondary passages lead to pronounced minima at small scales at the same time as the temperature and X-ray luminosity reach their maxima. When the peaks in the temperature and X-ray luminosity disappear, the minima also get much less prominent. So their lifetime as dominating structures of the magnetic field lasts for about 1 Gyear, therefore it is similar or slightly longer than the temperature or X-ray luminosity excess.

The major merger events trigger a large number of minima in the autocorrelation function across a range of smaller scales. These minima reflect the bending of the magnetic field by the velocity field. They can be maintained for a significant long timescale by even small residual motions or minor merger events, that support the complexity of the magnetic field against being damped on small scales. This damping is only observed for the g51 cluster. The g72 and g676 do not have a long enough quiet period without distortions. Here the g72 cluster has a second major merger, whereas the g676 cluster maintains some residual motions, which are visible in a small excess of strong shocks. Later it undergoes several minor merger events. This indicates that a time span of at nearly 4 Gyears of quiescent accretion is needed for the magnetic field of the cluster to relax in the simulations. A period of only 2.5 to 3 Gyears as in the two other clusters seems to be not sufficient.

The magnetic power spectrum does not show a power law over a significant range for the resolutions achieved in current simulations. The adaptive nature of the simulation is in principle able to reach the interesting scales. However, less resolved parts within the volume of interest, that induce a smoothing on relatively large scales, seem to influence the power spectrum significantly. So the power spectrum on small scales is strongly affected by numerical noise induced from less resolved areas. The limiting scale is the maximum smoothing length or a bit more optimistically the average smoothing length of all particles within the box the power spectrum is calculated on. This resolution limit is at least one order of magnitude away from the known ranges of observed power spectra. This is equivalent to an increase of the number of particles of the simulations by a factor of 1000.

Attempts to fit a power law on the power spectrum lead to results that depend strongly on the lengthscale where the fit is done. Nevertheless the shape of the power spectrum undergoes significant changes with time. But it is not clear from our analysis whether these changes on small scales have physical or numerical reasons.

Outlook

Finally figure 56 shows the time evolution of the spectral indexes of the magnetic power spectra of the 3 clusters together with some spectral indexes from observations. Although this plot has to be taken with large caution (from theoretical and observational side), the evolutionary tracks of the individual clusters demonstrate how the evolution of the simulated clusters shapes the magnetic field. Therefore it is encouraging to further push the simulation effort towards higher resolution to be able to better measure the structure of the magnetic field within the cluster. Better understanding of the interplay between the dynamical state of the cluster and the magnetic field will finally allow us a better interpretation of the observations.

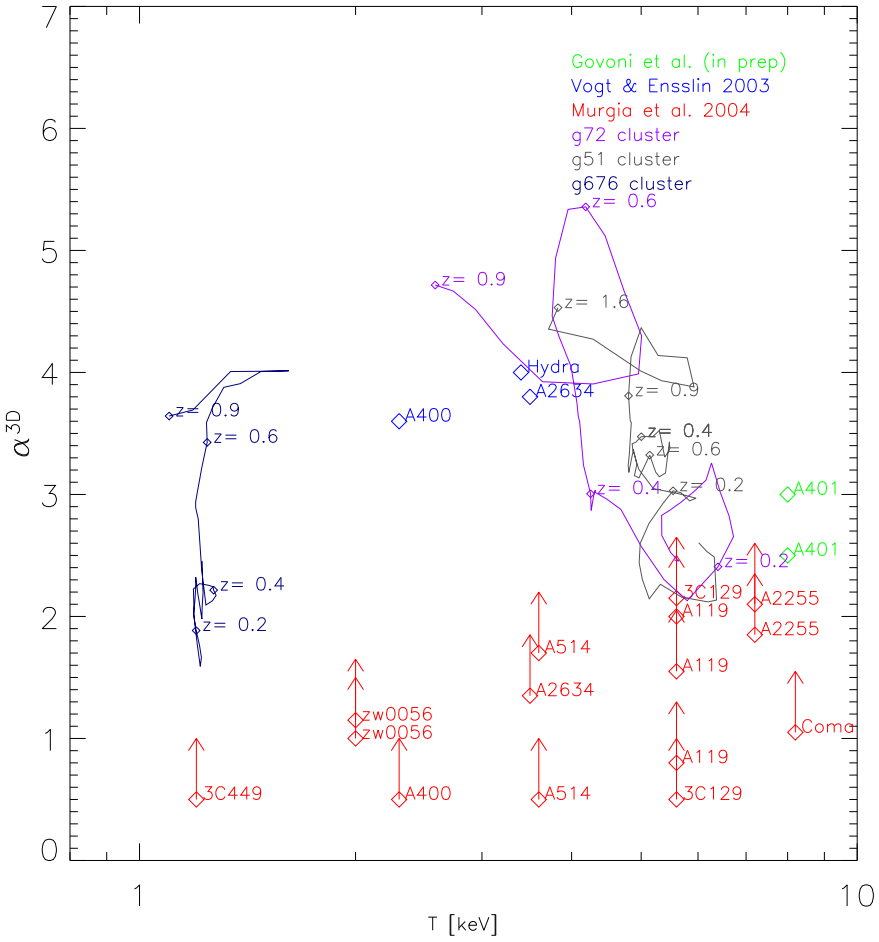

Figure 56: Comparison of observed spectral indexes of magnetic power spectra with the spectral indexes of the power spectra of the 3 simulated clusters g72, g51 and g676. Blue points are from [VE03]. One has to mention that they were measured on much smaller scales than the simulated spectral indexes. Red points show very weak lower limits from [MGF+04]. Green points are taken from Govoni et al. (in preparation). The purple, gray and dark blue lines show the evolution of the spectral index of the magnetic power spectra of the g72, g51 and g676 cluster, fitted around $100\frac{1}{\mathrm{Mpc}}$. As on this scale the power spectrum does not follow a power law over a significant range and the reliability of the power spectrum at these scales can be questioned, these indexes have to be taken with caution. For some points of the lines also their age is displayed in terms of redshift. It is important to note, that the values of these spectral indexes depend crucially on the point, where the power law is fitted. The tracks start after the first major merger.

References

[BOT01] S. Børve, M. Omang, and J. Trulsen. Regularized Smoothed Particle Hydrodynamics: A New Approach to Simulating Magnetohydrodynamic Shocks. *ApJ*, 561:82–93, November 2001.

[DBL99] K. Dolag, M. Bartelmann, and H. Lesch. SPH simulations of magnetic fields in galaxy clusters. *A&A*, 348:351–363, August 1999.

[DBL02] K. Dolag, M. Bartelmann, and H. Lesch. Evolution and structure of magnetic fields in simulated galaxy clusters. *A&A*, 387:383–395, May 2002.

[DCP87] J. W. Dreher, C. L. Carilli, and R. A. Perley. The Faraday rotation of Cygnus A - Magnetic fields in cluster gas. *ApJ*, 316:611–625, May 1987.

[DGST05] K. Dolag, D. Grasso, V. Springel, and I. Tkachev. Constrained simulations of the magnetic field in the local Universe and the propagation of ultrahigh energy cosmic rays. *Journal of Cosmology and Astro-Particle Physics*, 1:9–+, January 2005.

[FG79] S. M. Faber and J. S. Gallagher. Masses and mass-to-light ratios of galaxies. *Annual Review of Astronomy and Astrophysics*, 17:135–187, 1979.

[GM77] R. A. Gingold and J. J. Monaghan. Smoothed particle hydrodynamics - Theory and application to non-spherical stars. *MNRAS*, 181:375–389, November 1977.

[GM83] R. A. Gingold and J. J. Monaghan. On the fragmentation of differentially rotating clouds. *MNRAS*, 204:715–733, August 1983.

[GMF+06] F. Govoni, M. Murgia, L. Feretti, G. Giovannini, K. Dolag, and G. B. Taylor. The intracluster magnetic field power spectrum in Abell 2255. *ArXiv Astrophysics e-prints*, August 2006.

[Gov03] F. Govoni. Magnetic Fields in Galaxy Clusters. *The Cosmic Cauldron, 25th meeting of the IAU, Joint Discussion 10, 18 July 2003, Sydney, Australia*, 10, 2003.

[HE88] R. W. Hockney and J. W. Eastwood. *Computer simulation using particles*. Bristol: Hilger, 1988, 1988.

[Luc77] L. B. Lucy. A numerical approach to the testing of the fission hypothesis. *AJ*, 82:1013–1024, December 1977.

[MGF+04] M. Murgia, F. Govoni, L. Feretti, G. Giovannini, D. Dallacasa, R. Fanti, G. B. Taylor, and K. Dolag. Magnetic fields and Faraday rotation in clusters of galaxies. *A&A*, 424:429–446, September 2004.

[PSEJ06] C. Pfrommer, V. Springel, T. A. Enßlin, and M. Jubelgas. Detecting shock waves in cosmological smoothed particle hydrodynamics simulations. *MNRAS*, 367:113–131, March 2006.

[SBD+06] D. N. Spergel, R. Bean, O. Dore', M. R. Nolta, C. L. Bennett, G. Hinshaw, N. Jarosik, E. Komatsu, L. Page, H. V. Peiris, L. Verde, C. Barnes, M. Halpern, R. S. Hill, A. Kogut, M. Limon, S. S. Meyer, N. Odegard, G. S. Tucker, J. L. Weiland, E. Wollack, and E. L. Wright. Wilkinson Microwave Anisotropy Probe (WMAP) Three Year Results: Implications for Cosmology. *ArXiv Astrophysics e-prints*, March 2006.

[SH02] V. Springel and L. Hernquist. Cosmological smoothed particle hydrodynamics simulations: the entropy equation. *MNRAS*, 333:649–664, July 2002.

[SM93] S. Schindler and E. Mueller. Simulations of the evolution of galaxy clusters. 11. Dynamics of the intra-cluster gas. *A&A*, 272:137–+, May 1993.

[Spr05] Volker Springel. The cosmological simulation code gadget-2. *MNRAS*, 364:1105, 2005.

[VE03] C. Vogt and T. A. Enßlin. Measuring the cluster magnetic field power spectra from Faraday rotation maps of Abell 400, Abell 2634 and Hydra A. *A&A*, 412:373–385, December 2003.

[VE05] C. Vogt and T. A. Enßlin. A Bayesian view on Faraday rotation maps Seeing the magnetic power spectra in galaxy clusters. *A&A*, 434:67–76, April 2005.

[XW02] S.-J. Xue and X.-P. Wu. Chandra X-Ray Observatory Observation of A1689: New Determination of Mass Distribution and Comparison to Lensing Measurements. *ApJ*, 576:152–158, September 2002.

Acknowledgment

First I want to thank Dr. Klaus Dolag for the idea of this work and his guidance through it. Also he never got tired answering my questions and providing help where I needed it.

I also want to thank Prof. Dr. Wolfgang Hildebrandt for supervising this work.

I am grateful for the possibility to write this thesis at the MPA. It was a great environment for scientific work.

Furthermore I want to thank Dr. Christoph Pfrommer for providing his MACH-number detection scheme.

Additonally my special thanks go to all people at MPA i worked and talked with, exspecially Andreas Marek for many interesting and funny discussions.